Effect of Manufacturing on Microstructure and Magnetic Properties of Non-Oriented Electrical Steel

Aroba Saleem

Department of Mining and Materials Engineering

McGill University, Montreal

November 2017

A thesis submitted to McGill University in partial fulfillment of the requirements for the degree of Doctor of Philosophy

Table of Contents

List of Figures

List of Tables

Abbreviations

SEM	Scanning Electron Microscopy
EBSD	Electron Backscattered Diffraction
BSE	Back Scattered Diffraction
FSD	Fore Scattered Diffraction
SST	Single Sheet Tester
NOES	Non-oriented Electrical Steel
EDS	Energy Dispersive Spectrometer
XRD	X-ray Diffraction
FEA	Finite Element Analysis
RD	Rolling Direction
TD	Transverse Direction
ND	Normal Direction
WEDM	Wire Electric Discharge Machining

Abstract

The development of highly efficient electrical machines may lead to the conservation of electrical energy. Besides an improved design, the better selection of material and broader knowledge of the influence of manufacturing on the resulting magnetic properties may help to reach this target. Electrical steel grades are the normal construction material for electrical motors and transformers because of their enhanced soft magnetic properties. The magnetic characteristics of electrical steels are closely related to losses. Non-oriented electrical steels (NOES) are the most economical choice of material used in electrical machines to transform electricity in movement, as in electric car motors. In electromagnetic devices, the non-oriented electrical steel is often subjected to different mechanical stresses induced due to manufacturing such as cutting, interlocking and welding. Thus, it is important to evaluate magnetic properties under conditions present in actual electrical machines and understand the relationships between the magnetic properties and mechanical stresses induced. In addition, the mechanical cutting processes induce plastic deformation near the edges, which also affects the magnetic properties. Hence, the current research is to study magnetic properties of NOES and residual stress and deformation induced due to manufacturing and present the relation between microstructure, mechanical and magnetic properties affected by cutting.

Punching is a common process for manufacturing of cores of electric motors and causes shearing near the edge, resulting in degradation of magnetic properties. The deterioration of magnetic properties due to punching is commonly investigated using rectangular or toroidal samples in magnetic measurements units without focussing much on the microstructural changes near the edge. The present work has pursued this objective of analysing the microstructural changes due to punching and study the effect of punching load on microstructure near the edge. This work was accomplished by observing the cross section of the punched sample using scanning electron microscope (SEM) and analyzing the back scattered electron imaging (BSE) and electron back scattered diffraction (EBSD) micrographs. In addition, nanoindentation was performed to study the change in hardness near the edge due to punching. An attempt was made to separate the residual stress and deformation regions based on the microstructural and

mechanical property correlation. Other cutting methods such as shear cutting, and laser cutting were also studied in the present work.

These microstructural effects due to cutting were further related to magnetic properties. The investigation of magnetic property degradation due to shear cutting and laser cutting was done using a single sheet tester (SST). In addition, the core loss separation was employed to see the change in hysteresis and eddy current loss component separately, due to cutting. Finally, the effect of different cutting processes was compared, and a relation was established between the microstructure, mechanical properties and magnetic properties of non-oriented electrical steel.

Résumé

Le développement de machines électriques hautement efficaces devrait conduire à la conservation de l'énergie électrique. Une conception améliorée, un meilleur choix de matériel et une connaissance plus approfondie de l'influence de la fabrication sur les propriétés magnétiques résultantes peuvent aider à atteindre cet objectif. Les aciers électriques de haute qualité sont les matériaux de fabrication prépondérants pour les moteurs électriques et les transformateurs en raison de leurs très bonnes propriétés magnétiques. Les caractéristiques magnétiques des aciers électriques sont étroitement liées aux pertes. Les aciers électriques à grains non orientés (NOES) constituent le choix le plus économique de matériaux utilisés dans les machines électriques pour transformer l'électricité en mouvement, comme par exemple, dans les moteurs de voitures électriques. Dans les appareils électromagnétiques réels, l'acier électrique non orienté est souvent soumis à des contraintes mécaniques différentes, induites par la fabrication comme la coupe, le verrouillage et le soudage. Ainsi, il est important d'évaluer les propriétés magnétiques des machines électriques présentes dans les conditions d'opération réelles et de comprendre les relations entre les propriétés magnétiques et les contraintes mécaniques induites par le processus de fabrication. En outre, les processus de coupe mécanique induisent une déformation plastique à proximité des bords qui affectent également les propriétés magnétiques. Par conséquent, la recherche actuelle porte sur l'étude des propriétés magnétiques des NOES, le stress résiduel et la déformation induite par la fabrication. Un autre axe d'étude porte également sur les relations entre la microstructure, les propriétés mécaniques et magnétiques affectées par l'usinage.

Le poinçonnage est un processus commun pour la fabrication de noyaux de moteurs électriques et provoque un cisaillement près du bord, entraînant une dégradation des propriétés magnétiques. La détérioration des propriétés magnétiques due au poinçonnage est généralement étudiée en utilisant des échantillons rectangulaires ou toroïdaux dans des unités de mesures magnétiques sans se concentrer sur les changements microstructuraux proches du bord. Le présent travail a permis d'analyser des changements microstructuraux dus au poinçonnage et d'étudier l'effet de la charge de poinçonnage sur la microstructure près du bord. Ce travail a été accompli en observant la coupe transversale de l'échantillon perforé à l'aide d'un microscope électronique à balayage (MEB) et en analysant les micrographies par diffraction rétrodiffusée

d’électrons (EBSD). De plus, la nanoindentation a été effectuée pour étudier la variation de dureté près du bord en raison du poinçonnage. Nous avons essayé de séparer les régions stressées des déformation résiduelles en fonction de la corrélation des propriétés microstructurales et mécaniques. D'autres méthodes de coupe comme la coupe de cisaillement et la découpe au laser ont également été étudiées dans la présente thèse.

Les effets microstructuraux dus à la coupe ont également été liés aux propriétés magnétiques. L'étude de la dégradation des propriétés magnétiques, due à la coupe de cisaillement et à la découpe au laser, a été effectuée à l'aide d'un testeur de feuille unique. En outre, la séparation des pertes de noyau a été utilisée pour voir séparément la variation des courbes l’hystérésis et de perte de courant de Foucault, en raison de la coupe. Enfin, l'effet de différents processus de coupe a été comparé et une relation a été établie entre la microstructure, les propriétés mécaniques et les propriétés magnétiques de l'acier électrique à grains non orienté.

Acknowledgements

This work was completed with the support and guidance of many people and organisations, to whom I am deeply grateful. First, I would like to thank my research supervisor, Prof. Richard R. Chromik, for his help and support during my research and giving me the opportunity to study at McGill. Also, I would like to thank my co-supervisor Prof. David Lowther for facilitating the communication between the industrial partners and the university.

I would like to thank Nicolas Brodusch who helped me in using electron microscope during my research. I would also like to thank our department staff, especially Ms. Barbara Hanley, who helped me with any problems or questions during my work.

I wish to thank the Industrial partners, TM4, Infolytica, Linamar and Purolator for the financial support they offered for this research.

I would like to express my gratitude to the post doctoral fellow, Dr. Natheer Alatawneh, who helped me in my research. I am thankful to him for his interesting discussions during the research and his valuable feedback. I would also like to thank undergraduate student, Mengfan Zhang, for helping me in lab.

I would also like to thank my research group collogues and seniors, Dr. Tanvir Rahman, Dr. Dina Goldbaum, Dr. Pampa Ghosh, Dr. Yaoyao Ding and Dr. Matthew Gallaugher for their feedback and help. Also, I would like to thank Paul Fourmont, Debika Banerjee and Dina Goldbaum for helping me in writing the abstract in French. My friends also contributed to uplift me during hard times while writing my thesis and I am thankful to them. I am very thankful to Priyadarshi, Sima, Sara, Debika, Riya, Mansha and Sourav for their support.

I am infinitely grateful to my parents, Basharat Saleem and Masooda Yasmeen, for their relentless support, encouragement and patience during my PhD. I am also thankful to my family, Faizan, Farheen and Junaid, for being there throughout this journey. Last but not the least, I am thankful to Almighty Allah.

Preface

The present work is based on the collection of manuscripts that are submitted or yet to be submitted in the peer reviewed journals. The detailed contribution of each co-author to each individual journal paper is provided below:

Chapter 4: Study of change in microstructure and mechanical properties in a non-oriented electrical steel lamination due to interlocking

Mengfan Zhang, Dina Goldbaum and Aroba Saleem performed the punching of steel laminations and nanoindentation on the planar samples. Aroba Saleem also performed punching of the samples for cross section nanoindentation, post analysis and writing the manuscript. R.R. Chromik supervised this project and corrected the manuscript.

Chapter 5: Microstructure and mechanical property connections for a punched non-oriented electrical steel lamination

Aroba Saleem studied the microstructure of the cross section of punched sample using electron microscope, analysed and wrote the manuscript. Aroba Saleem also performed the nanaoindentation on the cross section of the punched sample and analysed the load-displacement curves obtained from nanoindentation. Nicolas Brodusch assisted in electron microscopy work on electron microscope. R. R. Chromik supervised the project, provided feedback and corrected the manuscript.

Chapter 6: Effect of Shear Cutting on Microstructure and Magnetic Properties of Non-Oriented Electrical Steel

Aroba Saleem performed the shear cutting of the steel laminations, microstructure and mechanical property analysis, magnetic testing, analysis of the data and writing the manuscript. Natheer Alatawneh guided in the execution of the project and provided feedback. R. R. Chromik and D. A. Lowther supervised the project, provided feedback and corrected the manuscript.

Chapter 7: Effect of Laser Cutting on Microstructure and Magnetic Properties of Non-Oriented Electrical Steel

Aroba Saleem performed the microstructural and magnetic characterization of the laser cut samples, analysed the data and wrote the manuscript. Natheer Alatawneh and Tanvir Rahman provided feedback and R. R. Chromik and D. A. Lowther supervised the project along with editing the manuscript.

1. Introduction

1.1 General description of electric machines and the importance of considering the manufacturing effects on machine performance

Personal and freight transportation is one of the key contributors in greenhouse gas (GHG) emissions. The transportation sector constitutes a major part in the greenhouse gas emission according to the European Union. The growth of greenhouse gas emissions from transportation is increasing every year and is expected to reach 50 to 100 % higher by 2050 [1]. The main policies to reduce the emissions from transportation are focussing on the optimization of the efficiency of the existing vehicles, the development of new sustainable fuels and propulsion systems, and the electrification of the vehicles. A more efficient, more reliable, safer and more environmentally friendly vehicle can be achieved by means of electrification.

A schematic chain of electrical energy transportation consists of a generator, which converts mechanical energy into electrical energy, and a motor, which converts electrical energy into mechanical energy. Whether electrical energy is converted into mechanical or vice versa, there is always some part of energy which is lost during the transformation. In electromagnetic energy conversion, an important part of the energy loss is because of the core of the electric device [2]. Here, the questions of efficiency and economical value of the electric device arises. How crucial is the energy loss due to the core? What are the ways to improve the efficiency? How to predict the losses in case of new designs or new materials?

The present work deals with the study of the core material used in electric motors. The material mostly used as a core in electric machines is electrical steel and electrical steels have important applications concerning energy needs such as electric cars [3]. A better understanding of electrical steel characteristics is important for improving the efficiency of electric machines and hence, reducing energy consumptions. Non-oriented electrical steel sheets are widely used as the core materials of motors. The magnetic properties of non-oriented electrical steel sheets have a large influence on motor efficiency.

Electrical steel laminations are designed in to motor core shape by cutting methods such as punching, guillotining, laser cutting and wire electric discharge machining (WEDM). The cutting techniques affects the properties of the steel lamination near the cut zone differently. Mechanical cutting induces deformation near the cut edge whereas laser cutting induces thermal shock wave which results in residual stresses. Thus, magnetic properties are affected by cutting. Magnetic property deterioration due to cutting has been investigated in the literature [4], [5] but less attention is given to the microstructural changes near the cut edge and how it affects the magnetic properties. The present research focusses on the effect of mechanical and laser cutting on the microstructure and magnetic properties of non-oriented electrical steel laminations. Scanning electron microscope was used to study the microstructural changes along with electron back scattered diffraction (EBSD) for orientation mapping, back scattered electron (BSE) imaging for electron channelling micrographs and fore scattered diffraction (FSD) for magnetic domain imaging. In addition, nanoindentation was performed on non-oriented electrical steel lamination to study the hardness profiles and pop-in phenomena near the cut edge. Further, the laminations were cut in long strips and magnetic properties such as core loss and permeability were determined using single sheet magnetic testers.

1.2 Problem Definition

The electrical steel laminations are designed into the core of electric machines by various manufacturing processes. The manufacturing processes, such as punching, shearing, laser cutting, interlocking, welding, bonding, riveting, and pressing lamination stack into a frame, are known to deteriorate the magnetic properties of electrical steel sheets [4], [6], [7].The influence of different cutting techniques on the microstructural parameters such as grain size and shape, inclusion content, dislocation density and magnetic properties such as magnetic loss and permeability of non-oriented electrical steel is presented in this study. Better understanding of manufacturing process will lead to a better selection and design of electric machine parts, consequently improving the efficiency.

1.3 Research Objectives

The overall objective of this research is to understand the effect of different cutting processes on the microstructure, mechanical and magnetic properties of non-oriented electrical steel. However, the specific objectives can be described as follows:

1. Investigate the change in microstructure and mechanical properties of non-oriented electrical steel at various stages of punching, which further improves the understanding of interlocking of core laminations.
2. Observe the microstructural modifications near the edge due to punching and relate that with the mechanical properties. This chapter attempts to separate the effect of work hardening, residual stress and grain refinement on hardness change due to cutting based on microstructure.
3. Study the effect of different cutting techniques on magnetic properties of non-oriented electrical steel
4. Relate microstructure with magnetic properties in mechanical and laser cut samples.

1.4 Thesis Organisation

The present thesis is divided into nine Chapters. Chapter 2 gives the overall literature review on the current topic. It also includes the fundamental concepts and past research work done on this subject. Chapter 3 consists of experimental methodology employed for all the research work carried out in this study. As per the requirement for manuscript based thesis, Chapter 4 to Chapter 7 are in the form of complete articles, which are to be submitted or accepted in peer reviewed academic journals.

In Chapter 4, hardness change at various stages of punching from lower to higher load is presented. Nanoindentation measurements along with the SEM micrographs were employed to measure the local hardness and microstructural details of the sample, respectively. The maximum hardness increase near the punched edge at different loads and the reason behind the increase in hardness was studied and discussed. This study was done to understand the effect of interlocking on the microstructure and mechanical properties of NOES.

In Chapter 5, a detailed microstructural analysis is presented for a punched sample with a huge burr and related to the mechanical properties. Back scattered images and band contrast maps were used to observe shear bands in the deformed zone and nanoindentation measurements was employed for characterization of mechanical properties.

In Chapter 6, the influence of shear cutting on the magnetic properties of NOES is studied. In this chapter, two grades were selected and magnetic property degradation was studied after shear cutting. The magnetic measurement was performed by single sheet tester and material characterization by SEM and nanoindentation.

In Chapter 7, the laser cut steel laminations were tested and their magnetic properties were investigated. The reasons for magnetic deterioration were studied by performing microstructural and micromagnetic analysis near the cut edge using electron microscope

Chapter 8 presents the global discussions followed by the summary of all results in Chapter 9.

2. Literature Review

Society's need to reduce energy consumption has been rising along with the need to address environmental problems. Electric machines such as motors and generators are increasingly used in several industrial sectors which consume a significant portion of energy, thus, a considerable attention is paid to decrease those machines' power consumption [8]. The design and optimization of efficient electric machines results in a lower power consumption, which require a broad knowledge of the magnetic materials used in the machines' structure. This leads to a strong demand for improvement of non-oriented electrical steel (NOES) used in manufacturing of the machines' cores [9].

Cores of electric motors and generators are fabricated by cutting the electrical steel laminations to the specified shape and then clamping or welding the cut laminations. Various cutting operations such as mechanical cutting (punching and shear cutting) and laser cutting can be used which induces stresses near the cut edge [10]. These stresses result in the deterioration of the magnetic properties including iron losses and permeability [11]. Mechanical cutting also induces plastic deformation near the edge, which affects the microstructure and consequently, the magnetic properties, whereas laser cutting affects the magnetic properties by inducing thermal strains [4]. The test conditions employed at the laminations manufacturing facility are distinctly different to those that the laminations are subjected to when used as a core in the electric motor. For example, the catalogue data is available for the electrical steel sample before mounting it as core in the motor. On the other hand, the magnetic properties of electrical steel core are different than those before mounting due to cutting, welding and clamping operations. This discrepancy may affect the performance of the electric motor. Hence, in order to be able to incorporate the material degradation into electrical machine design, it is necessary to characterize the local change of the magnetic properties in an accurate way [12]. In this chapter, a literature review is presented that discusses the NOES material, manufacturing processes and change in the microstructure and magnetic properties due to manufacturing.

2.1 Fundamental magnetic concepts

2.1.1 Hysteresis loop

The macroscopic magnetic properties of the materials are due to the magnetic moments which are associated with individual electrons [13]. Each electron in an atom has magnetic moments that originate from two sources: one from the motion of electron around the nucleus, which may be considered as a small current loop generating a very small magnetic field and other from the rotation of the electron around its own axis (electron spin). Thus, each electron in an atom may be considered as a small magnet with orbital and spin magnetic moments. The net magnetic moment of an atom is the sum of the magnetic moments of individual electrons and magnetic moments of some electron pairs cancel each other resulting in zero net moment. Thus, materials composed of atoms having completely filled electron shells (He, Ne, etc.) are considered as non- magnets. Materials are divided into various categories namely diamagnetic, paramagnetic and ferromagnetic based on the net magnetic field associated with the atoms, which depends on their atomic and molecular structure [14]. Diamagnetism is a weak form of magnetism that is not permanent and persists only under the influence of external magnetic field. It is induced due to the change in the orbital motion of electrons and the direction is opposite to that of external magnetic field. Another category is paramagnetic materials in which the atoms have magnetic moments aligned randomly in the absence of magnetic field and these magnetic moments are aligned in the direction of external field, if applied, with no mutual interaction between the dipoles. Certain metallic materials possess permanent magnetic moment in the absence of an external field and manifest very large and permanent magnetizations. These are called ferromagnetic materials. The magnetism in these materials mainly arises from the spin magnetic moment of electrons, in addition to the orbital magnetic moment. Furthermore, there is coupling interactions of the atoms which cause magnetic moments of the adjacent atoms to align with one another, even in the absence of external field. This mutual alignment of magnetic moments exists over a relatively large volume of the crystal called magnetic domains [14]. Adjacent domains are separated by domain boundaries or walls, across which the direction of moments gradually changes. In a polycrystalline material, each grain may consist of more than a single domain. When a small external magnetic field is applied, domains with moments oriented nearest to the direction of the applied field grow at the expense of their neighboring domains. At higher field, the growth of domains occurs by domain wall motion and domain rotation, both of which are irreversible at such amplitudes. When the field amplitude is further increased, saturation occurs and the sample converts into a single domain. This is the state of saturation magnetization [15]. Saturation magnetization mainly depends on the composition of the material because the maximum value of magnetization which can be achieved by the material is only affected by the initial state such as number of free electrons, valency of the substitutional or interstitial atoms, etc.

Ferromagnetic materials are mainly characterized by their hysteresis loops, which gives the relation between the flux density, B and the magnetic field strength, H. Thus, the hysteresis loop is also called B-H loop (or magnetization loop). When a ferromagnetic material is magnetized and taken through a magnetization cycle, the time lag between the applied magnetic field strength, H and the corresponding flux density, B, of the material results in a typical B-H loop (Fig. 2.1). When H is increased from zero in a ferromagnetic material that is completely demagnetized, B increases along a given direction and follows the dashed line to reach point 'a'. This dashed line represents the initial magnetization curve of the material. All the magnetic domains are almost aligned at point 'a' (to practically form one big domain occupying the whole specimen, as shown in full grey color) and an increase in H will produce very little increase in B and the material attains magnetic saturation, B_s. When H is completely reduced to zero, some magnetic flux remains aligned in directions different than those of their initial directions when H was zero, where the curve arrives point 'b', also known as the state of remanence, B_r, which means that the material remains magnetized in the absence of external field. This permanent magnetization may be explained by the motion of domain walls. The resistance to the movement of domain walls that occurs in response to the increase in magnetic field in opposite direction accounts for the lag of B with H [14]. A reversal of H from zero to negative values, the point 'c' is reached where the flux, B, reduces to zero, also known as the coercive point, H_c. At further increase of H in the opposite direction, point 'd' is reached where the material again becomes magnetically saturated but this time in the opposite direction. Reducing H back to zero brings the curve to point 'e', where a level of remanence ($-B_r$) equal to that achieved in the other direction is seen. Applying H again along the positive direction (domains marked in grey start to grow again at the expense of oppositely oriented domains in white) returns B to zero at point 'f' (both grey and white-colored domains co-exist). From point 'f', the curve takes a different path back to the saturation point, where the loop is completed. The ease with which magnetic flux is established in a material defines the permeability of the material. Permeability (μ) is used to define the relationship between B and H as shown in Eq. 2.1 [14]–[16]:

$$\mu = \frac{B}{H} \qquad \dots (2.1)$$

The permeability, μ, is not constant for ferromagnetic materials and is a function of H [17] (see section 2.1.2).

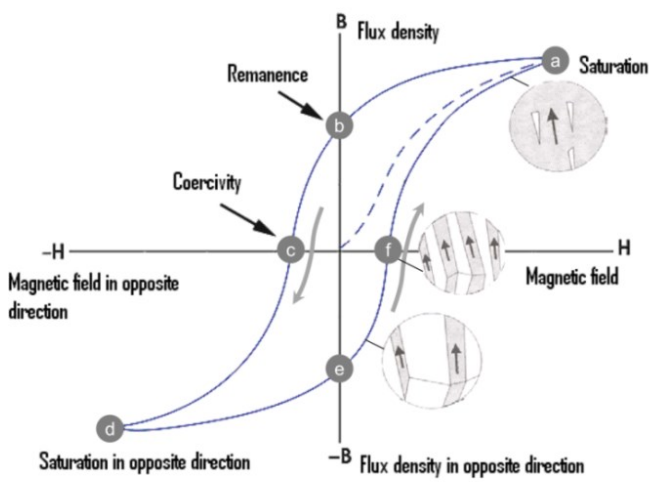

Fig. 2.1 Typical B-H loop of a ferromagnetic material [15].

Ferromagnetic materials are divided into two categories, namely, soft magnetic materials and hard magnetic materials, based on their hysteresis characteristics as shown in Fig. 2.2 [17].

Soft magnetic materials require lower applied field strength to reach saturation compared to hard magnetic materials. In other words, soft magnetic materials are easy to magnetize and demagnetize and their distinguishing character is high permeability which makes them fit to use for electric machines and devices [14]. An example of soft magnetic material is Si-steel, also called electrical steel, used as a core in electric machines. Hard magnetic materials, on the other hand, are used as permanent magnets where high coercivity is required.

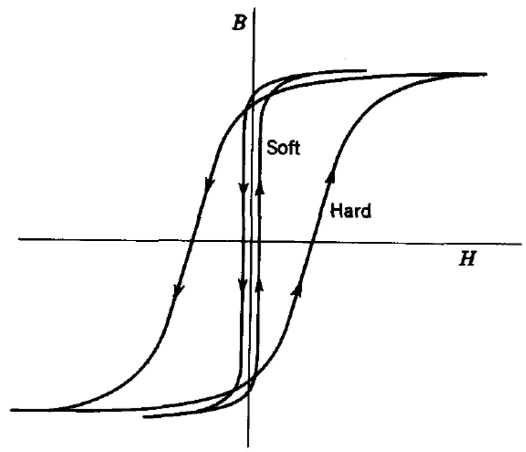

Fig. 2.2 Hysteresis loops for soft and hard magnetic materials [17].

The shape of the hysteresis curves and the magnetic properties of soft magnetic materials such as permeability, coercivity, and losses are related to the microstructure of the material such as grain size, inclusions, impurities, defects, and texture [18]. These microstructural parameters affect the motion of domain walls and consequently acts as pinning sites for the movement of domains. Crystallographic texture is important because magnetization behavior can be different along different crystallographic directions. In case of bcc iron, <100> is the easy direction of magnetization whereas <111> is difficult [19].

2.1.2 Magnetic permeability

The magnetic permeability is an important property of ferromagnetic materials calculated from the initial magnetization curve (*B-H* curve) and is a measure of the flux density produced by a given field (Eq. 2.1). It is to be noted that permeability is not the slope, *dB/dH*, of the *B-H* curve but rather the slope of a line from the origin to a particular point on the curve as shown in Fig. 2.3 [14]. The magnetization curve (Fig. 2.3a) starting at the origin has a finite slope which gives the magnitude of initial permeability, therefore, the μ-H curve (Fig. 2.3b) starts with a finite permeability for infinitesimal fields [17]. Another value of permeability which is often quoted is the maximum permeability (μ_m). This value divides the magnetization curve (Fig. 2.3a) into two parts: easy magnetization up to μ_m and hard magnetization beyond μ_m. This can be explained with the help of domain theory. The magnetic domains are aligned randomly in an unmagnetized state with each domain aligned in the direction of easy axis with an overall negligible magnetization. With the application of field, some domains become unstable and rotate quickly to an easy direction parallel or close to the direction of applied field which accounts for the easy magnetization before the maximum permeability (Fig. 2.3a) [17]. With further increase in *H*, beyond μ_m, the domains which are not already aligned in the direction of applied field are rotated gradually towards the direction of *H*. This requires higher field strength until saturation where all the domains are aligned in the direction of *H* and accounts for the hard magnetization section, beyond μ_m, in the *B-H* curve (Fig. 2.3a).

The permeability, μ, of the ferromagnetic material is also defined as the product of relative permeability (μ_r) and the permeability of vacuum which is 4×10^{-7} H m^{-1} [14], [17]. Since, the permeability of vacuum is constant for all the values of *H*, the relative permeability follows the same trend as the permeability in μ-H curve (Fig. 2.3b) and attains a peak value at μ_m. The relative permeability is a dimensionless quantity which is customary to use instead of permeability which has dimensions of H m^{-1}. The permeability of ferromagnetic materials is strongly structure sensitive and so depends on purity, inclusion fraction, grain size and crystallographic texture [14].

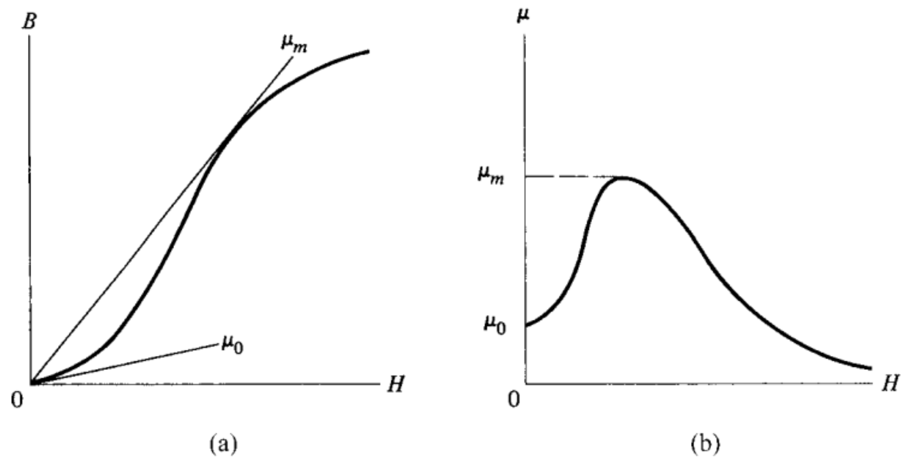

Fig. 2.3 Typical magnetization curve for ferromagnetic material (a), and corresponding variation of permeability with H (b) [14].

2.1.3 Core loss

The core loss is, conventionally, divided into two components, hysteresis loss (W_h) and eddy current loss (W_e), which is given in Eq. 2.2, where $W_h \propto f$ and $W_e \propto f^2$ [14]. It is, therefore, expected that loss per cycle (W/f) will vary linearly with frequency and is equal to W_h at zero frequency.

$$W = W_h + W_e \qquad \ldots(2.2)$$

The first component of core loss equation (Eq. 2.2) is hysteresis loss (W_h), which is determined from the area of the hysteresis loop and is caused due to the pinning of magnetic domains resulting in extra energy required for domain movement during magnetization. This area can be obtained by integration and is proportional to B^2 [20]. Suppose that a magnetic material is excited from zero to the maximum field and then back to zero field. At the end, the returned power is less than the supplied power and the lost power is considered to be used in the reorientation of the magnetic domains which causes hysteresis [20]. The hysteresis loss component is sensitive to structural variables such as grain size, inclusions and defects present in the material which affect the domain movement during magnetization [14]. The second component of core loss equation (Eq. 2.2) is eddy current loss (W_e) which is described as follows: "when the material experiences changes in magnetic field, a flux is generated which causes eddy currents to develop, which in turn creates a counter field leading to a shielding effect proportional to the rate of change of flux density, thereby reducing the net magnetic flux and causing decrease in the current flow". The eddy current losses are less in materials with high resistivity, however, high resistivity is usually coupled with low permeability [20]. Hence, a trade-off exists between them for material design. Further, the eddy current loss is proportional to B^2 and f^2 [14], [20].

There is a discrepancy between the measured eddy current loss and the calculated eddy current loss and the difference between the two is called the anomalous loss or excess loss. It appears because the calculation of eddy current loss ignores the presence of domains and domain wall motion, and is therefore too low [14]. Hence, the measured eddy current loss (W_e) for electrical steel laminations can be expressed as an algebraic summation of classical eddy current loss (W_c) and excess (or anomalous) loss (W_{excess}) [14]–[16], [21]–[23] as shown in Eq. 2.3, where σ is the electrical conductivity, d is the sample thickness, B_{max} is the saturation flux density, f is the frequency and A_{cs} the cross-sectional area of the sample. The parameter G = 0.1356 for electrical steel laminations and is a dimensionless parameter whereas V_0 is known to be a constant for flux density up to 1.3 T and increases at higher levels [23].

$$W_e = W_c + W_{excess} = \sigma \pi^2 d^2 B_{max}^2 \frac{f^2}{6} + 8\sqrt{\sigma G A_{cs} V_0(B_{max})}\,(B_{max} f)^{\frac{3}{2}} \qquad \ldots(2.3)$$

The separation of losses into its components is shown in Fig. 2.4 where loss per cycle is plotted against the frequency. The loss per cycle increases with frequency, but not linearly, giving a concave-downward curve. This is because the domain spacing is not constant but decreases with increase in frequency [14]. As a result, the domain wall motion is affected by frequency, which consequently affects the losses.

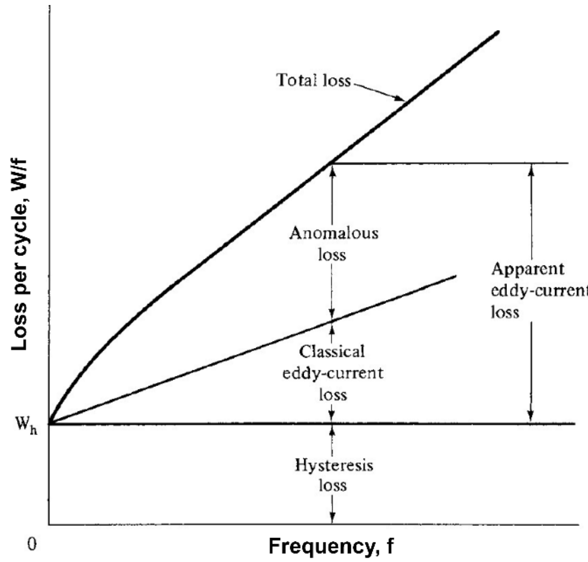

Fig. 2.4 Conventional separation of total core loss [14].

2.2 Material parameters that affect the magnetic properties

The material parameters such as composition, grain size and crystallographic texture that affect the magnetic properties of soft magnetic materials such as electrical steel are as follows.

2.2.1 Composition

The steels used as magnetic cores inside the transformers or motors, which require better magnetic properties, are low carbon steels with an addition of ~3 % Si (known as electrical steel). Addition of Si results in improving the magnetic performance of steel by increasing the resistivity and reducing the core loss [24]. The Si concentration can vary between 1 and 3.7 wt.% and some percentage of Al (0.2-0.8 wt.%) and Mn (0.1-0.3 wt.%) is usually added, by which the alloy resistivity is further increased without impairing the mechanical properties [25], [26]. Enormous efforts have been made to discover binary, tertiary or quaternary alloys which are able to perform better than silicon as resistivity raisers. Remarkably, the silicon used in 1903 remains the overall most successful alloying element [26].

Nowadays, other alloying elements instead of, or in addition to, Si are widely used. Among them, the most important is Al, which affects the magnetic properties of iron similarly as silicon does. Al also prevents magnetic ageing by N precipitation, by stabilizing it through the formation of A1N second phases [27]. Magnetic ageing is the increase in core loss of the material with time, which occurs due to the precipitation of carbon and nitrogen when their amount in solution exceeds the solid solubility limit at the temperature of use [27], [28]. For non-oriented electrical steels with aluminum addition, the sum of contents of both base elements (Si + 2Al) is up to 4 %. Manganese (Mn) is also an alloying element, either in the small amounts needed to assure that all sulphur content is combined as manganese sulphide to avoid hot shortness during rolling, or in some conditions to improve crystallographic texture [3]. The most common explanation of hot shortness in steel is that iron and iron sulphide form a low melting eutectic which produces a liquid phase at the grain boundaries at the usual hot working temperature of steel [29]. This eutectic phase melts at the working temperature and the material starts to separate at the grain boundaries. Mn combines with sulphur to form a more refractory sulphide which avoids the liquid phase. Al and Mn form the non-metallic inclusions AlN and MnS in the steel; however, impurity elements like Cu, Ti, Se, Cr, Zr etc. can also form inclusions and thus influence both the texture development and the magnetic properties [25]. Due to its effect in increasing electrical resistivity, phosphorus is used in contents around 0.1%, which are higher than those in steels for mechanical applications. Tin (Sn) and antimony (Sb), in contents below 0.1%, are frequently added to electrical steels. Addition of Sn and Sb decreases intergranular subsurface oxidation during annealing and may improve texture in some circumstances [3].

2.2.2 Microstructure

The magnetic properties of the soft magnetic materials such as magnetization curves, permeability, coercive field and core losses are related to the microstructure (grain size, inclusions, surface defects) and crystallographic texture. These microstructural parameters determine the pinning sites, which restricts the movement of domains during magnetization. The effect of grain size (*D*) on core loss can be understood by dividing the total loss into its components and studying the effect of grain size on each component. Hysteresis loss decreases with grain size whereas the eddy current loss increases as shown in the Fig. 2.5. The combination of these two components offers a typical trend for core loss vs. grain size with a minimum loss achieved at an optimum grain size which is reported to be 100 – 150 µm in non-oriented electrical steel (NOES) [24], [30]–[32]. NOES is a soft magnetic material which is used as a core in electric motors.

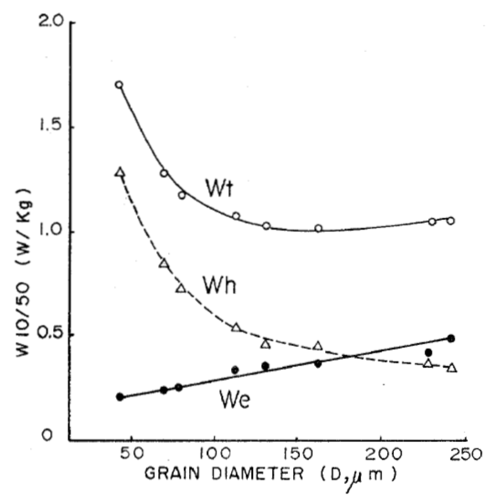

Fig. 2.5 Effect of grain diameter of electrical steel on the total loss and its components [24].

The grain size of the material gives an estimation of the grain boundary area which acts as a hindrance to the movement of domains during magnetization. This resistance to the movement of domains increases hysteresis losses and also coercivity. Therefore, smaller the grains more the grain boundary area and higher the hysteresis losses [18], [24], [33]. On the other hand, eddy current losses are lower for smaller grains and vice versa. This is because of the fact that grain boundaries increase the electrical resistivity of the material and eddy current loss is inversely proportional to resistivity [24]. Hence, when *D* is varied (with other factors being unchanged), hysteresis loss (W_h) varies in proportion to *l/D* and eddy current loss (W_e) more or less in proportion to *D* [24], [34]. Thus, the optimum grain diameter is a reasonable compromise between W_e and W_h to achieve minimal core loss. Further, W_h is influenced by the presence of inclusions, Si% and texture, which are also necessary to be optimized. Hence, during manufacturing, it is important to reduce the content of impurities, inclusions and fine precipitates (as they impede grain growth) and grow grains into optimum grain size by short-time continuous annealing [24], [31]. A typical microstructure of a non-oriented electrical steel is shown in Fig. 2.6. The grains are observed as dark and light polygonal structures which are visible due to electron channelling contrast and domain structure is also visible within the grains resulting from magnetic contrast. These contrast effects are discussed later in this chapter. The inclusions and/or precipitates are also visible in the microstructure as black dots. Non-oriented electrical steels (NOES) have been among the steel products that benefit most from crystallographic texture optimization for the improvement of magnetic properties; however, the focus of processing technology has largely been on the control of grain size [25].

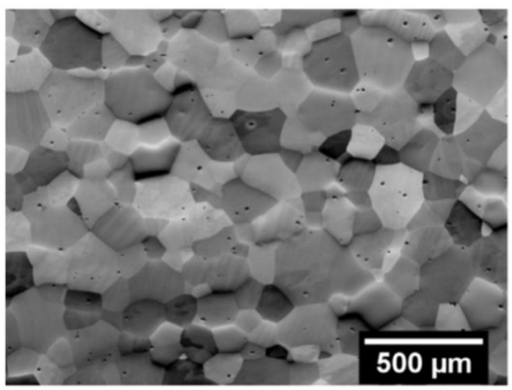

Fig. 2.6 SEM image of a non-oriented electrical steel showing the grain morphology [35].

2.2.3 Crystallographic Texture

Crystallographic texture determines the distribution of crystallographic orientations in a material and there is an unexplored possibility of improving the magnetic properties of electrical steels through texture control [36]. The material with random crystallographic orientations has no or weak texture whereas the material with some preferred orientation has medium or strong texture. In electrical steels, the role of crystallographic texture is based on the relation between the crystallographic direction and magnetocrystalline anisotropy energy. The magnetocrystalline anisotropy energy is the energy due to atomic interactions and is minimum for the domains located along certain crystallographic directions termed as easy directions of magnetization [19]. In electrical steels, the easy direction of magnetization is <100> whereas <111> direction is hard to magnetize. Therefore, the crystal with [100] orientation is easily magnetized with highest permeability whereas crystal with [111] orientation has low permeability. The [110] orientation comes in between [100] and [111] orientation in terms of magnetization. Hence, in the absence of applied field, the domains align themselves parallel to <100> direction to reduce the magnetocrystalline anisotropy energy. Therefore, the preferred orientation in electrical steels consists of orientations with easy direction parallel to the magnetization direction. However, in rotating applications, the direction of magnetization changes continuously and hence, there is no point of having an easy direction parallel to one specific direction. Therefore, the satisfactory texture for the steel sheet used in rotating applications (non-oriented electrical steel), where the field is in the plane of the sheet, must have <100> directions within the plane of the sheet whereas <111> out of the plane.

Crystallographic texture in NOES is generally represented as {hkl} <uvw>, which signifies that the {hkl} planes of the grains lie parallel to the plane of the sheet, whereas their <uvw> directions lie parallel to the rolling direction (RD) [37]. A schematic representation of two orientations is shown in Fig. 2.7, where (011) [100] and (001) [100] texture is presented. The (001) plane has two easy axes of magnetization which lies within the plane of the sheet, whereas in (011), only one easy axis lies within the plane of the sheet. On the other hand, (111) texture has no easy axis of magnetization parallel to the plane of the sheet. This means that orientation of the grains in NOES must have {100} or {110} planes parallel to the sheet whereas {111} should be avoided.

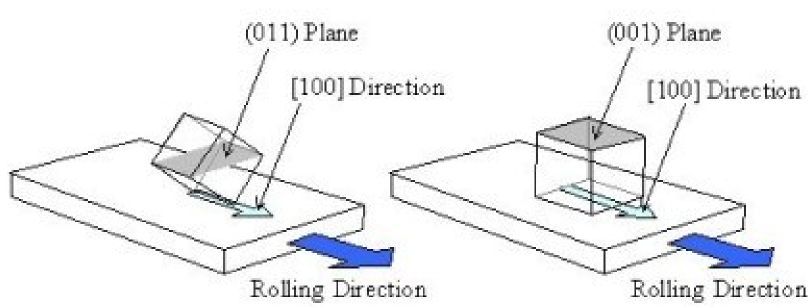

Fig. 2.7 Schematic of the plane of the sheet showing different crystallographic texture orientations [38].

The texture is conventionally represented by pole figures but more complete description is provided by the orientation distribution function (ODF) [37]. An ODF specifies the frequency of occurrence of particular orientations in three-dimensional (Euler) space. The characteristic texture components of steel are mainly the cube ({001}<001>), the rotated cube ({001}<110>), and the Goss ({110}<001>) components which are of importance for magnetic applications [39]. It was reported by Cunha et al. [40] that texture improvement is achieved mainly by reducing the volume fraction of the [111] ∥ND (Normal direction – direction perpendicular to rolling plane), that is the main recrystallization texture component of α-iron, and increasing the volume fraction of texture components belonging to [001] ∥RD and [001] ∥ND. Also, texture can be improved remarkably by the addition of Sb which was found by Honda et al. [31]. Finally, the evaluation of the texture effect on the magnetic properties remains a challenge because it is very difficult to separate its effect from the one exerted by the grain size or second phase inclusion.

2.3 Electrical Steels

Electrical steels are the commonly used material in cores of electromagnetic devices and especially, the electrical motors, generators and power transformers [41]. Electrical steel is categorized into two types: grain-oriented and non-oriented electrical steels (NOES). Grain-oriented electrical steel (GOES) is a class of steel with 3% silicon in which strong (110) [001] crystallographic texture is developed by abnormal grain growth [3]. The magnetic properties along the rolling direction are excellent in these steels and these are used as core material in transformers. In non-oriented electrical steel, on the other hand, the properties are measured as an average for the rolling and transverse directions with {100} <uvw> as a favourable texture [14]. The {100} <uvw> texture means that the easy direction which is <100> is randomly oriented along the plane of the sheet whereas the hard <111> direction is out of the plane. This texture is good for applications where the angle between the magnetic field and the rolling direction of the sheet is variable but the field is in the plane of the sheet. This helps in keeping the properties uniform in all the directions along the plane of the sheet and makes it isotropic. Hence, NOES is the soft magnetic material most commonly used in applications that demand isotropy of magnetic properties along the plane of the sheet, such as rotating electrical machines [3].

The study and the control of the magnetic parameters of NOES has become a very important economic issue because these materials are used extensively and hence, are responsible for great part of the energy losses in electrical systems [42]. These steels are made by hot rolling to near final thickness, acid pickling to remove oxide layers, and cold rolling to final thickness, which gives the best surface finish and flatness. NOES can be supplied in semi processed form which requires a subsequent annealing treatment or it can be fully processed where annealing is done as a final step at the steel mill. [14].

2.3.1 Manufacturing

Non-oriented electrical steel offers a challenge in terms of its alloy design, thermomechanical processing and structure-property correlation, for improving its magnetic performance. Typical magnetic properties of interest to the motor manufacturer are core loss and permeability and these properties depends on metallurgical factors such as composition, cleanliness of steel, grain size and crystallographic texture [43]. Manufacturing of these steel laminations into the final motor core design induces residual stresses and other microstructural changes in the lamination, consequently affecting the magnetic properties [10]. No simple or straightforward relationship exits between the microstructure changes due to manufacturing and mechanical and magnetic properties after manufacturing. The motor manufacturers get the NOES laminations from the steel producers considering all the factors such as composition, thickness of lamination, grain size and so on - the cost economics also being a primary criterion. In modern steelmaking, the cleanliness and composition can be controlled well and the other metallurgical parameters depends on the thermomechanical processing sequence [43]. Non-oriented electrical steels are produced by a process of casting, hot rolling, cold rolling and heat treatment. The end product must be very low in carbon and sulphur and free from non-metallic inclusions, that is, metallurgically very 'clean' [44]. The lower grade NOES laminations (up to 2 wt. % Si) are produced and delivered in the semi-processed state and follow the same thermomechanical history of low-carbon steels, with final thickness ranging between 0.65 mm and 0.50 mm. The higher grades are instead fully processed materials. The hot rolled sheets (thickness 2.3 mm - 1.8 mm) are cold rolled to intermediate gauge, annealed at 750°C - 900°C reduced to the final gauge of 0.65 mm - 0.35 mm, and subjected to a recrystallization and decarburization anneal at 830°C - 900°C and a final grain-growth anneal at 850°C - 1100°C [25].

These laminations are designed into the motor core shape by various cutting techniques such as mechanical (punching or shear cutting) or laser cutting, then pressed during stacking of laminations to cores and welded or riveted. All these processes can substantially affect the magnetic properties but cutting is considered most important because it causes higher degradation of magnetic properties than other processes [45], [46]. The deterioration of magnetic properties by manufacturing, called building factor, must be considered in the calculation of core losses [11]. The building factor is defined as the ratio of core loss of the electrical steel laminations after mounting as a core inside the motor to the core loss of the laminations before manufacturing. It is important to reduce the building factor in order to reduce the energy loss in motors. Also, the catalogue data available for the lamination consists of the values calculated before manufacturing, therefore, the building factor has to be taken into account for the accurate calculation of losses of electric motors. The mechanical cutting (punching) of steel laminations is widely used for the preparation of electrical machines because of its low production cost [4]. Punching induces mechanical strains, whereas laser cutting induces thermal strain near the cutting edge both of which affect the magnetic properties [10]. A large fraction of electrical steel cores is manufactured by guillotining (shear cutting) which causes shearing of the lamination near the cut edge [47]. Reported works on these cutting techniques show that the lamination's magnetic properties are indeed sensitive to the cutting method. The variations in losses and permeability due to the cutting method can reach up to 10% and up to 20%, respectively, at 60 Hz, and 1.5 T [5].

The microstructure of the lamination is modified near the edge due to cutting, which affects its magnetic performance [10], [48]. The changes in microstructure near the edge have been previously investigated by optical microscope [49] and electron microscope [4], [50]. In addition, magnetic domains were observed by some researchers near the cut edge by magneto-optical Kerr microscopy [10]. In most of these articles, the study of microstructure is only performed to compare the micrographs for different cutting methods without providing the details of microstructural modifications and their relation to mechanical or magnetic properties. The magnetic domain analysis near the edge performed by Naumoski et al. [10] explains the domain structure after punching and laser cutting of NOES but more research is required to study domain structure for different cutting processes. Thus, understanding the local degradation of the lamination due to cutting is crucial for improving the cutting process and also for the design and simulation of the electrical machines.

2.3.1.1 Punching

Punching is a process of cutting off sheets using a die and a punch, applying shear stress along the thickness of the sheet [51]. Load is applied on the punch so that it passes through the lamination to create a hole (or any other shape) whereas the die is located on the other side of the lamination to support it while punching. Shearing happens by severe plastic deformation locally near the punched edge followed by fracture which propagates deeper into the lamination resulting in fracture [51]. Punching involves plastic deformation [4] and therefore, the force required for shearing near the edge is theoretically equal to the shear strength of the lamination [51]. Due to friction between the lamination and the punch, the actual punching force is higher than the shear strength.

Punching is the most common process of manufacturing cores of electric motors because it is less expensive than other cutting techniques [52]. The deteriorating effect of punching on the magnetic properties of the material is revealed close to the punched edge in the previous work [52], [53]. This harmful effect leads to the virtual decrease of cross section of the core and increase of air gap of the electric motor [52]. When the steel lamination experiences plastic deformation during punching, the energy supplied to the material results in lattice misorientation which creates defects. These defects act as pinning sites for the domain wall motion during magnetization and results in the modification of both magnetic and mechanical properties [53].

The area affected by punching can be measured by various means such as microhardness measurements [52], [54], localized voltage measurements induced in coils near the edge [55], Kerr microscope observations [10] or finite element simulations [56], [57]. The effect of punching on magnetic properties of NOES lamination studied by Naumoski et al. [10] is shown in Fig. 2.8. In that study, rings of NOES lamination were produced by punching and laser cutting. Also, spark erosion (electric discharge wire cutting) was used as a reference cutting method. Punching deteriorates magnetic properties which is observed by shearing of the curve and permeability is significantly reduced as shown in Fig. 2.8. The most deteriorated properties are observed in laser cut samples because rapid heating and cooling affects a large zone and changes magnetic properties. The laser cutting effect will be studied in more detail in one of the following sections. Similar results for magnetic deterioration due to punching NOES were reported by Manescu et al. [58] where the magnetic property deterioration was observed due to plastic deformation and the stresses induced by cutting. Due to plastic deformation, the microstructure near the edge is altered which results in increase in dislocation density and hence, restricts the domain movement during magnetization [48], [50].

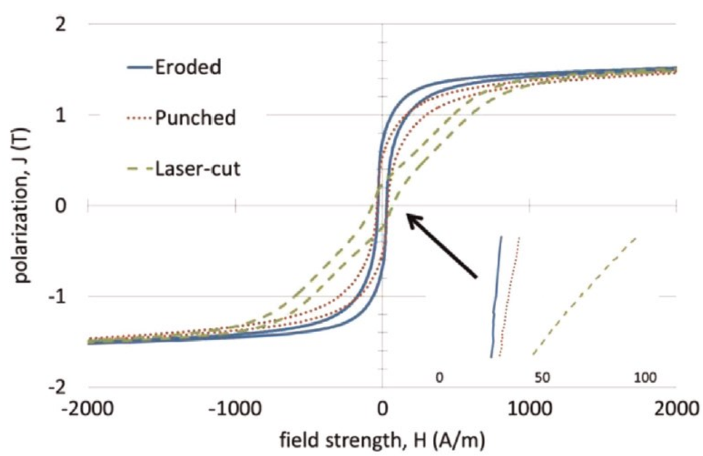

Fig. 2.8 Hysteresis loops for the NOES lamination cut by spark erosion, punching and laser cutting [10].

The degradation of magnetic properties of NOES due to punching affects the overall performance of electric motors. Chiang et al. [59] modeled the affected area due to punching and included that in the finite element analysis for the design of electric motor cores as shown in Fig. 2.9. The punching damage reduced the maximum air gap flux density and thus the torque output of the electric motor. In addition, the effect of punching is different under different operating conditions such as frequency which requires further investigations. Hence, most of the research work done previously has been focussed on the magnetic property measurements with little or no focus on the microstructure changes near the edge and the stresses induced. Recent article by Xiong et al. [50] has reported the microstructure changes due to mechanical cutting of NOES lamination and its effect on magnetic properties. In this article, crystallographic texture was observed near the cut edge by EBSD and misorientation distribution was measured as shown in Fig. 2.10. From Fig. 2.10 (a), the misorientation angle is affected near the mechanically cut edge resulting in an increase in low angle grain boundaries. This increase in low angle grain boundaries near the edge has a detrimental effect on the magnetic properties as shown in Fig. 2.10 (b). Also, the magnetic deterioration depends on the cutting volume per unit mass of the sample. This article was a good attempt to study the crystallographic texture and relate it with magnetic properties but a lot of work is yet to be done in this field to understand the microstructure and texture better.

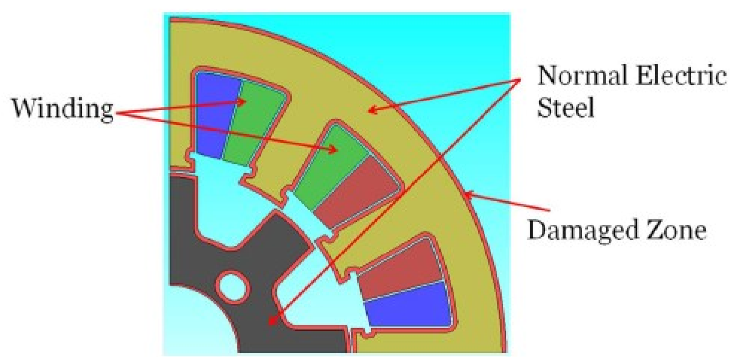

Fig. 2.9 Schematic of the simulation model of motor core lamination with damaged zones due to punching [59].

The magnetic properties are deteriorated to different degrees depending on the modification of microstructure near the edge such as grain size, plastic deformation and residual stress. Kashiwara et al. [60] developed a finite element model to separate the effect of plastic deformation and residual stress on the flux density of NOES. The results of deformation analysis and electromagnetic analysis for a punched sample is shown in Fig. 2.11. It is evident from Fig. 2.11 that large plastic deformation is observed near the edge which results in a significant drop of magnetic flux density. It is also evident that residual stresses are induced due to punching which are compressive in some regions and tensile in other regions. These stresses also affect the magnetic flux density where magnetic flux density further drops in the compressive residual stress regions and rises in tensile residual stress regions.

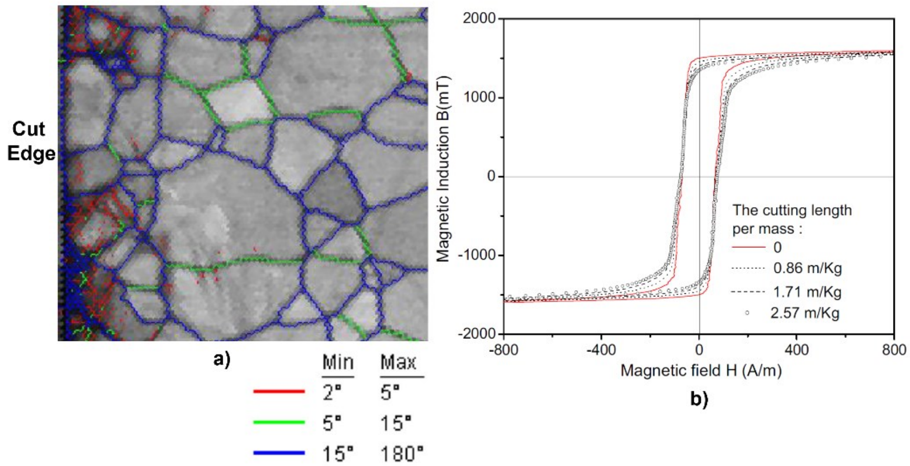

Fig. 2.10 a) Misorientation angle distribution near the mechanically cut edge, and b) hysteresis loops for the cut samples with different cutting length per mass [50].

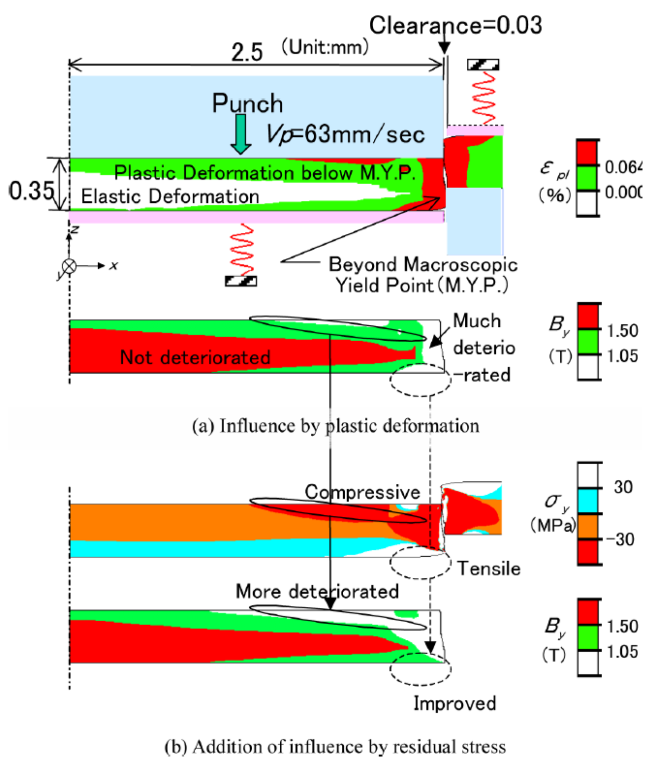

Fig. 2.11 Development of strain and residual stress during punching process of NOES laminations, as simulated by finite element modeling [60].

Hence, the magnetic flux density distribution in the motor cores is non-uniform with the minimum magnetic flux density near the edge. This means that there are different zones of material with different magnetic properties: the maximum deteriorated zone near the edge due to plastic deformation, less deteriorated zone due to elastic deformation and the damage free zone. The microstructure in these regions can be different and this analysis is presented in the current research. Another mechanical cutting process which is similar to punching is guillotine cutting (shear cutting) and is reviewed in the following section.

2.3.1.2 Guillotining (shear cutting)

Shear cutting is a process in which the sheet metal is separated by applying enough force to cause fracture in the sheet using a blade. It is similar to punching and the process involves shearing of the sheet metal by a blade instead of a punch as in punching. During shear cutting, the upper blade is forced past a lower stationary blade (or stationary base) and the sheet metal is held in position by supporting devices. Typically, the upper blade is mounted at an angle to the lower base in shear cutting. The shearing near the edge while cutting results in the modification of the microstructure and material properties near the edge which consequently affects the magnetic properties [47]. Thus, this cutting method is similar to punching and is used when straight cuts are required.

A large fraction of electrical steels is shaped into motor core laminations by shear cutting [47]. Shear cutting results in the modification of the cut edge by inducing plastic deformation and residual stresses near the cut edge. As a result, the magnetic properties are deteriorated as was the case in punched laminations but the deterioration is less than punching [5]. The hysteresis loops, at 50 Hz and 1.5 T, of the NOES laminations cut by shear cutting and laser cutting is shown in Fig. 2.12. The 150 mm × 150 mm spark eroded sample was taken as a reference and the other three curves are for laminations cut by shear cutting, laser cutting and spark erosion. Magnetic characterization was done using double yoke single sheet tester and the Fig. 2.12 shows that losses are increased by shear cutting and the increase in loss is from 30 %

to 70 %. Similar results for shear cutting NOES was reported by Baudouin et al. [47] where a 20-50 % quality drop was observed for the magnetic properties such as permeability and coercivity.

In addition to mechanical cutting which is commonly used for manufacturing motor cores, another cutting method called laser cutting is used for manufacturing motor core laminations. The effect of laser cutting NOES lamination on its magnetic properties is discussed in the next section.

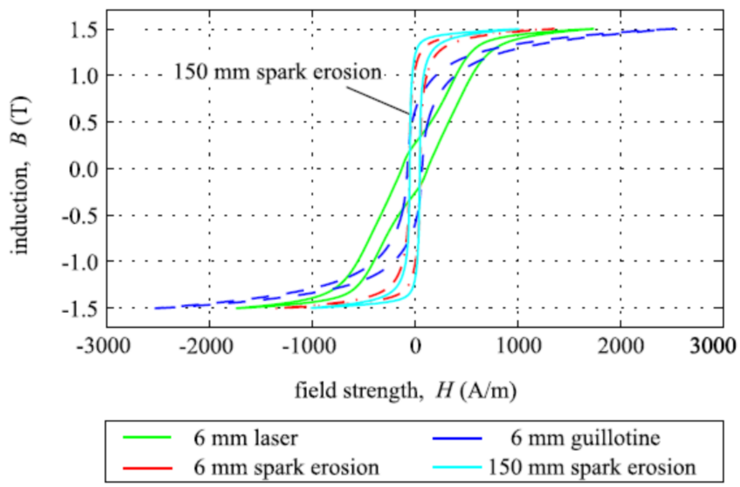

Fig. 2.12 Hysteresis loops of the shear cut (guillotine cut) and laser cut NOES laminations [53].

2.3.1.3 Laser Cutting

Laser cutting is a non-contact cutting technique, which provides flexibility for the design of electrical components and therefore, can appear as the ideal cutting solution for electrical steels manufacturers. Nevertheless, it has been shown that the laser cutting technique leads to more degradation of the magnetic properties of the electrical steels than the mechanical cutting technique [5], [61]. The application of laser cutting in manufacturing motor core laminations is mainly for small batch or prototype manufacturing. However, current developments in laser cutting often deal with the cost reduction and quality improvement for large scale production where mechanical cutting techniques are preferred [62]. This is because markets are changing and set new requirements that motor manufacturers have to face in terms of increased flexibility and reduced time. In this context, new and improved cutting techniques can provide results with significant relevance in industrial application.

Laser cutting the electrical steel lamination involves an incident laser radiation which melts the material and an assist gas jet which removes the molten material. In order to complete a particular cutting job, the gas nozzle and the workpiece has to be moved relative to each other to achieve an optimum cutting speed. The cutting speed for complex two dimensional parts is generally in the range of 20-30 m/min whereas in case of thin sheets, it is higher [62]. It is well established that laser cutting induces thermal stresses near the edge, which deteriorate the magnetic properties [6], [11]. The knowledge of the type of deterioration mechanism and degree of deterioration is important for designing the electrical machines in terms of core loss calculations.

The effect of laser cutting on the magnetic properties of NOES has been investigated in the literature, but the reason of this effect is not yet well understood. This is because most of the researchers focus on the magnetic property deterioration rather than understanding the microstructural modification near the edge which leads to this deterioration. A study to understand the microstructure near the laser cut NOES lamination was done by Belhadj et al. [6], [63] where electron microscope was used for microstructural and crystallographic texture analysis. A heat affected zone (HAZ) consisting of bainitic structure (width around 60 µm) was observed near the cut edge for semi-processed NOES whereas no HAZ was found in fully processed steel. As a result of this, the magnetic properties were deteriorated more in semi processed than in fully processed steel. The drop of permeability was more than 50% in semi-processed steel which is higher for a 60 µm heat affected zone. This means that there are residual stresses which extends beyond this HAZ in semi-processed steel. Also, there were texture developments and change in size of inclusions near the cut edge. After cutting, the texture along the cutting line appeared very heterogeneous. In addition to the material modification, the cutting parameters such as cutting speed and assist gas also affect the extent of deterioration. Hence, no direct link can be made between the magnetic property deterioration and the parameters affecting the extent of deterioration. Furthermore, optimization of the parameters is required to get the good results. In most of the previous literature, laser cutting is considered a bad cutting process compared to mechanical cutting in terms of magnetic properties deterioration [5], [49], [53] whereas some articles [55] have reported good results for laser cutting. Hence, these conflicting results on the effect of laser cutting on magnetic properties of NOES requires more research in this area particularly microstructural characterization which is the cause of this damage.

Many parameters are tunable in the laser cutting and could be optimized for further developments. One way would be the use of a high-frequency pulsed beam which would limit the size of the heating area near the cut edge [6]. Also, the medium used while cutting affects the heating area near the edge such as Oxygen and Nitrogen. Fig. 2.13 compares the hysteresis curves of the samples cut by the four different techniques out of which photocorrosion is considered as reference. The laser-cut sample presents low remanence and higher coercive force than other cutting methods [5]. Similar results were observed in the sections 2.3.1.1 and 2.3.1.2.

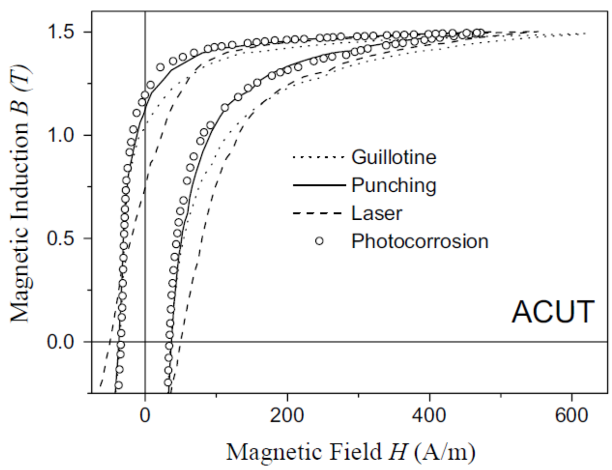

Fig. 2.13 Hysteresis curves of electrical steel cut by different techniques [5].

The changes in mechanical properties near the cutting edge has been investigated by microhardness measurements which gives an estimate of the affected area near the edge [4], [6], [49]. This method gives an estimate of the damaged region (plastic deformation) in mechanically cut samples whereas in laser cutting, no change in mechanical properties is observed as shown in Fig. 2.14. Thus, it is difficult to estimate the damage due to laser cutting and its effect on magnetic properties.

A significant variation of the extent of the degradation by cutting occurs from material to material due to differences in microstructure, crystallographic texture, and silicon content. The method of cutting also has an important effect as discussed above. A review of the microstructure and the residual stresses induced due to different cutting methods is presented in the next section.

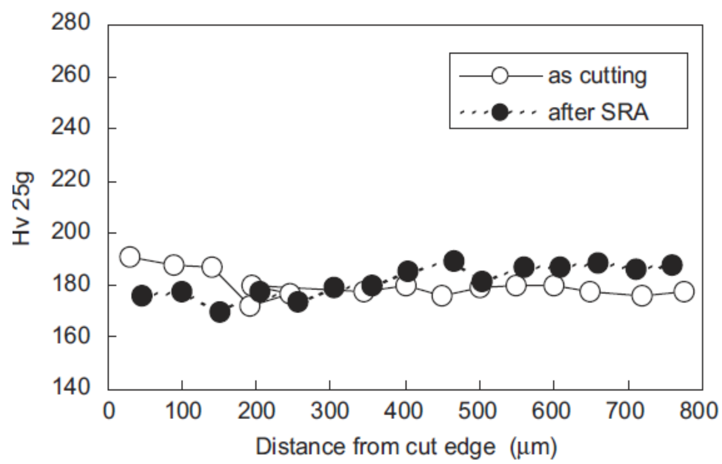

Fig. 2.14 Hardness profiles near laser cut edge of NOES lamination without and with stress relief annealing (SRA) heat treatment [4].

2.3.2 Microstructure and Residual Stress Induced Due to Different Cutting Methods

As discussed above, the microstructural modifications near the edge due to cutting needs more research for better understanding. In this section, the study of microstructure near the cut edge which has been previously done for different cutting methods is presented. The study of microstructure in the literature was done by observing the edge profiles of NOES laminations cut by different methods. An example of such a study is shown in Fig. 2.15 [4] where cross section edge profiles of NOES lamination cut by shearing and laser cutting is given. The sample cut by shearing is having a deformed region near the edge whereas the edge of laser cut sample appeared slanted. Similar edge profiles were observed by Emura et al. [5] and Shi et al. [49] for mechanical and laser cut NOES laminations. These images reveal the general information about the shape of the cut edges after mechanical or laser cutting. Further, investigations of crystallographic texture by EBSD or x-ray diffraction near the cut edges is reported in some articles [6], [48], [49]. The mechanical cutting and laser cutting leads to the development of new texture near the edge which is very heterogenous. This is due to the lattice distortion in case of mechanically cut samples whereas melting in case of laser cut. Hence, it becomes very difficult to explain the changes in magnetic properties by qualitative analysis of the texture components. However, magnetic properties can be best explained by texture factor (TF) which is the ratio of favourable orientation (cube fiber) and unfavourable orientation (γ fiber) with respect to magnetic properties [64]. Texture factor ascertain the effectiveness of the favourable orientations over unfavourable orientations. An attempt to study the texture changes due to mechanical cutting was done by Xiong et al. [50] where TF was calculated in the area from the edge to different distances towards the centre. An increase in TF was observed from the edge towards the centre. This means that mechanical cutting results in the change in orientation of the grains near the edge which are not favourable for magnetic properties. Even if the observation was done by EBSD consisting of more than 100 grains for each scan, the texture results are still limited. In order to get more information regarding the microstructure and texture modification due to cutting, more work is required in this area.

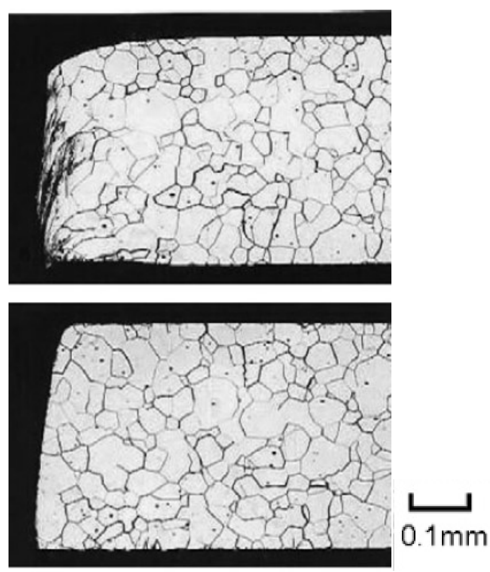

Fig. 2.15 Cross section of the cut edges of NOES lamination a) shearing and b) laser cutting [4].

Another important factor which affects magnetic properties is residual stress induced by cutting. During the past years, different methods were employed to measure residual stress in the material induced due to various processes such as manufacturing, thermomechanical treatment and coating deposition in NOES. Kai et al. [65] used x-ray diffraction method to measure the distribution of residual stress in the tooth of a motor core lamination, Ding et al. [66] observed residual stress distribution due to coating of NOES by nanoindentation and Vourna et al. [67] used magnetic Barkhausen measurement as a tool to estimate the residual stress in the NOES. The study of residual stress distribution due to cutting NOES is limited because residual stress varies from point to point from the cut edge towards the centre and the average residual stress measurement in a specific area (like in x-ray diffraction) will not give the detail required. For point to point measurement, nanoindentation is an appropriate tool which is not explored enough in this area.

Due to the complexities in measurement of residual stress distribution near the cut edge, researchers use finite element model near the cut edge [56], [57], [60], [68]. An example of stress distribution is shown in Fig. 2.16. Negative values of stress mean compressive stress and positive ones are related to tensile stress. High compressive stress regions are observed near the burr region. In the central layer of the sheet cross section, the tensile stress was appeared near the sheared edge, and that stress varied the compressive stress with the distance from the cut edge.

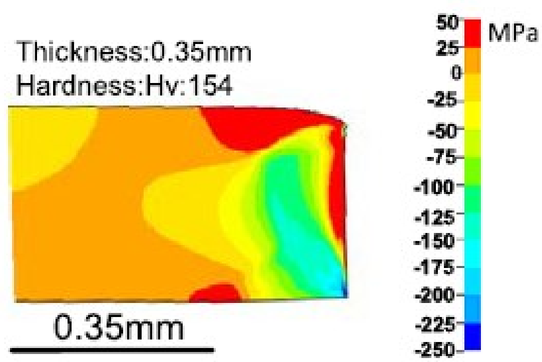

Fig. 2.16 FEM results of stress distribution by the shearing process [56].

The residual stress analysis in the cut NOES laminations has been performed for mechanically cut steel as discussed above whereas no such literature is available for laser cut NOES even if the laser cutting process also induces stresses due to thermal fluctuations. Also, the distance up to which these stresses extend from the cut edge is not clear.

Another way of understanding the reason of magnetic property deterioration due to cutting is the study of magnetic domain structure near the edge. There is very limited research done in this area. A recent work by Naumoski et al. [10] has reported the magnetic domain structure near the punched and laser cut edge of NOES using magneto-optical Kerr microscope. It was found that there is no magnetic domain contrast in the region affected by cutting whereas beyond the affected region, a good contrast was observed. Also, the deterioration by laser cutting was found to be more than mechanical cutting. Comparable results were observed by Hofmann et al. [53] where local magnetic contrast was analysed near the cut edge of NOES by Kerr effect. There are also other methods which can be used to image the magnetic domains such as Bitter patterns and electron microscopy but these are not yet explored in understanding the cutting effects. In the present research, SEM is used to image magnetic domains near the laser cut NOES sample for better understanding the magnetic deterioration. The advantage of using SEM is that it can provide local magnetic contrast with high spatial resolution and provides information about the crystallographic texture which is important in NOES laminations [35].

In the present study, the material and magnetic characterization of cut NOES laminations was done by various equipment such as standard magnetic testers for magnetic measurements and SEM and nanoindentation for material and mechanical characterization. An overview of the measurement equipment is presented in the following sections.

2.4 Experimental Setups for Magnetic Measurements

This section presents an overview of the development in the construction, design and features of several types of magnetic measuring systems (Epstein, single sheet tester and ring testers) being employed over the years. This section will analyze and discuss in detail some of the important testers in each type based on their geometry, advancements, significance, drawbacks and capabilities for precise magnetic measurement under stress.

2.4.1 Epstein Frame

'Epstein frame' standard is one of the most used standard, IEC 60404-2 [69]. Epstein frame is an unloaded transformer comprising of a primary winding, a secondary winding and the specimen to be tested as a magnetic core. Its application is limited to flat strip specimens obtained from magnetic sheets and strips, having a width of 30 ± 0.2 mm and length 280 ± 0.5 mm [2], [69], [70]. It allows studying the magnetic properties of anisotropic materials in any considered direction. The orientation of lamination sheets can be in RD, TD or can be combination of both [2]. Fig. 2.17 (a) shows the frame, a closed circuit typical for standard characterization of soft magnetic materials, also applied in several standards IEC 60404-2-3-4-6-10. The number of steel samples used in tests is at least 12 or a quadruple. Furthermore, it is permissible to apply a force of about 1 N to each corner to fix the lamination and avoid vibrations at high frequency measurements. In practice, beside the primary *H* coil (700 turns) and secondary *B* coil (700 turns), the Epstein frame consists of *H* compensation coil (also known as, air flux compensation coil). This coil compensates the *H* field to avoid distortion of the test results.

One of the disadvantages of an Epstein frame is the difficulty of determination of the mean length of the magnetic path. Also, there is a non-uniform distribution of the magnetic flux density at the corners of the frame which leads to inaccuracy of measurements [71]. However, since the dimensions of the frame are standardized the repeatability between the different setups for the same material is known to be very good. Despite the mentioned imperfections, the measurements obtained on the Epstein frame are generally used as a reference [70]. Epstein testers have been used by researchers [72], [73] for measurement of magnetic properties on plastically deformed (cold rolled) electrical sheets. However, no literature has been found based on in-situ measurement under the application of stress. On commercial scale, standardized Epstein testers are manufactured by various manufacturers (such as Brockhaus Measurement) which also been adopted for magnetic characterization [72], [74].

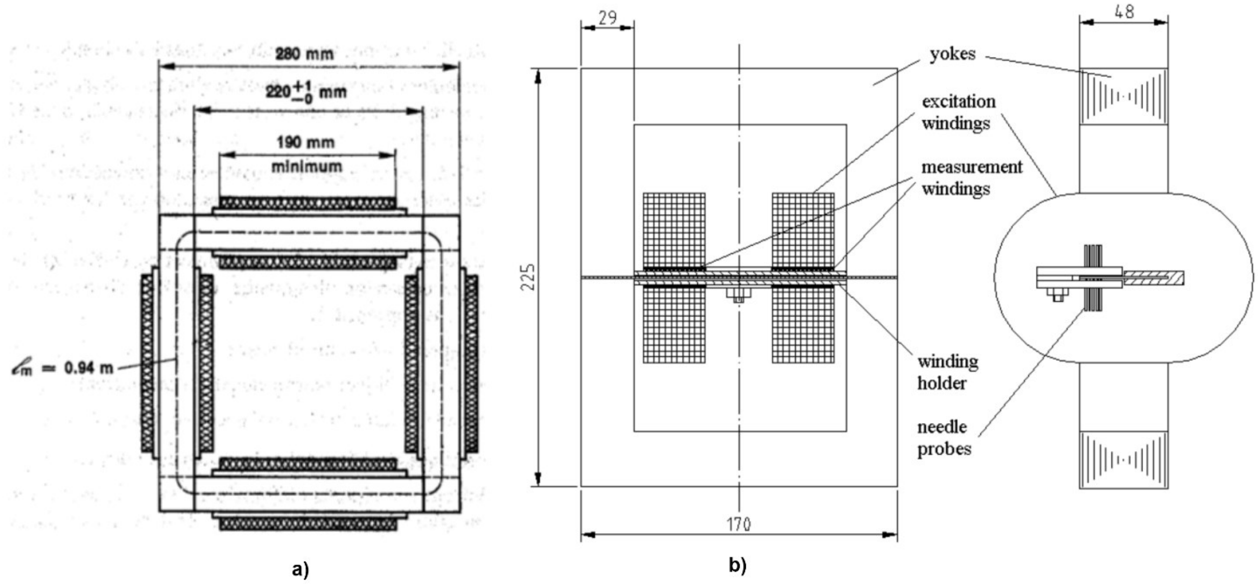

Fig. 2.17 (a) Epstein frame as per IEC 60404-2 [69]; (b) Schematic of SST for local investigation of magnetic properties [70].

2.4.2 Single Sheet Tester (SST)

Another mostly used standard, also called 'SST' standard is based on IEC 60404-3 [75]. In Fig. 2.17 (b), the magnetic sheet specimen is placed inside two windings, an exterior primary winding (the excitation winding) and an interior secondary winding (measurement winding). The setup was found to be most suitable for unidirectional excitation based measurements because it provides uniform flux density in the sample with very low leakage. In conventional SST, the yoke in U or C-form can be made up of insulated sheets of grain oriented Si steel or high permeability Si-Fe [76] or Ni-Fe iron alloy in order to reduce the effect of eddy currents and provide a more homogeneous distribution of the flux. According to standard IEC 60404-3 [75], the air gap between the opposite poles faces must be kept less than 0.005 mm in order to form a suitable closed circuit. The length of the test specimen varies from 200mm [77] to 500 mm, and width less or equal to the width of the yokes. Wulf et al. [78] obtained measured results from SST and co-related with the Epstein frame tester using sinusoidal waveform. An accuracy within 5% deviation was achieved. Annex B of IEC 60404-3 proposes the non-obligatory calibration of the SST [75].

Over the years, several modifications and up-grades have been done on the standard SST to perform magnetic measurements with sample subjected to mechanical load. One of the most primitive and distinct design to conduct magnetic measurements under stress was developed in the year 1980 by Moses et al [79]. This setup was used extensively for the testing of magnetic characteristics of electrical steels under the influence of both compressive and tensile stress [79]–[81] and the maximum stresses that could be induced in the samples of different thicknesses were up to ±40 MPa.. However, in early 2000, a better way to apply tensile load was developed by Iodarche et al. using universal tensile testing machine (Fig. 2.18 (a)) [82]–[84]. The setup had the capability to measure Barkhausen noise energy in addition to in-situ measurement of magnetic characteristics under tensile stress (~650 MPa). The setup showed excellent repeatability and accuracy.

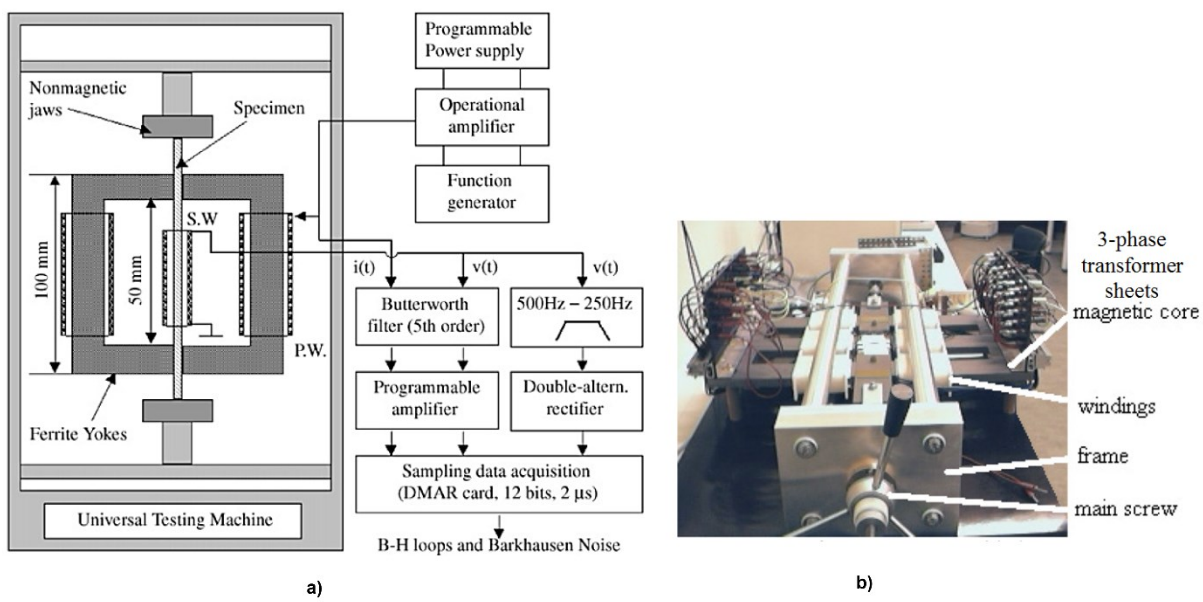

Fig. 2.18 (a) Schematic of Classical Double Yoke SST adapted on a Universal Testing Machine [82], (b) Rotational SST coupled with mechanical assembly for the application of tensile stress [70], [85].

Further modification to increase the capability of the setup for in-situ measurement of magnetic properties in the thickness direction under compressive stress (up to 10 MPa) was done by Miyagi et al. [86]. Using SST, it is also possible to introduce uniaxial compressive stress to a sample along its length using a horizontal tensile (UTM) tester [87], [88]. Over the years, several researchers [8], [87], [89] have used stress-load type SST modified on the conventional Vertical

Double Yoke SST for the in-situ measurement of magnetic properties under both tensile and compressive stress.

Other modified SST like the rotational SST uses two sets of *B* and *H* probes places in the same area as required [71]–[73]. Nakata et al. [90] improved the performance of Nencib's RSST (rotational SST) [91] by using laminated auxiliary yokes to help reduce the leakage fluxes. Nakano et al. [92] did further improvement by positioning the exciting windings as near as possible to the test specimen in order to avoid leakage fluxes. Later, Pulnikov et al. [70], [85] developed an in-situ horizontal mechanical subsystem RSST for the direct investigation of the effect of tensile stress for 0° to 360° orientation of stress with respect to *H*, shown in Fig. 2.18 (b). In the measurement setup, the magnetic circuit consists of a core formed with 3-phase transformer sheets surrounded by the windings, a solid frame to carry a load, a manually driven shaft and a combined system of grips. In the setup, only sample and core parts are magnetic. At one side of the shaft a transducer is installed to measure the applied mechanical load. The direction of the *H* in the magnetic core was altered from 0° to 360° by sequentially activating alternating windings which is an analogue to flat RSST [93] but with an extension to apply mechanical load.

Recently, an interesting setup to allow measurement of vector magnetic property at any orientation (between 0° to 180°) of field, *H,* with respect to RD has been developed, which have been successfully applied in research [94]–[98]. The setup is equipped with six axial strain gauges to measure 2-D magnetostriction (at 0°, 60° and 120° to RD) and mechanical strain (at 0°, 45° and 90° to RD) during stress application. The equipment allows testing of cross-shaped NOES specimen with slits (to obtain uniform stress distribution) using sinusoidal waveform, with in-situ application of stress in orthogonal directions (tension and/or compression up to 30 MPa).

It can be concluded from this section that SST is clearly the most suitable measurement system for unidirectional excitation. It provides a sufficiently uniform flux density in the sample. Also, the leakage is low. However, it increases with the saturation of the sample.

2.5 Electron microscopy

Scanning electron microscopy (SEM) can provide local texture information with high spatial resolution when EBSD is utilized [99]. SEM can also be used to image magnetic domains [100], making it an ideal candidate for imaging magnetic domains of NOES along with capturing local texture information. When using local misorientation maps calculated from the indexed orientation data, EBSD measurements provide additional information about the depth of deformation introduced by the various cutting methods because they highlight local strain variations [48].

The scanning electron micrograph of a non-oriented electrical steel shows different contrast effects such as electron channelling contrast, magnetic contrast and contrast due to deformation (if present). The electron channeling contrast is caused by a variation in the signal resulting from changes in the angle between the incident beam and the crystal lattice of the specimen. Hence, the grains are clearly observed in NOES samples under SEM. Another contrast which is magnetic contrast results in the appearance of magnetic domains in SEM image. This is due to the interference of magnetic field of the domains with the path of the incident electron beam falling on the sample. The deformation induced in the material results in point to point changes in contrast in the sample resulting in a mottled structure within the grains. These produce bands of contrast within the grains which are also called as "bend contours" [101]. Hence, information about magnetic characteristics and deformation can be extracted from SEM besides the information about grain morphology and crystal orientation.

2.5.1 Electron Channelling Contrast

2.5.1.1 Contrast between grains

Electron channelling contrast is caused by a variation in the signal resulting from changes in the angle between the incident beam and the crystal lattice of the specimen. The probability of an electron being backscattered (deflected through an angle greater than 90º) depends on how close it approaches the nucleus of the atom that is scattering it. In a crystalline material, the backscattered electron signal generated by the specimen depends on the crystal lattice structure. If the beam is allowed to scan across a polycrystalline material containing grains of different orientations, each grain will have a different brightness levels relative to its neighbours as shown in Fig. 2.19. Channeling contrast can also be used to study any change in the crystallography inside a grain such as twin or subgrain boundary.

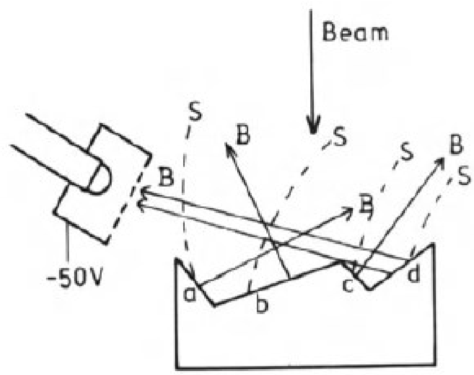

Fig. 2.19 Schematic of backscattered electron emission from facets of different orientations indicating that signal received from different orientations is different resulting in varying brightness levels [102].

A high beam current is required to produce a channeling contrast in order to produce an acceptable signal-to-noise ratio. For a long recording time, such as photographic purposes, an incident current of 10^{-9} A is sufficient, but for visual scan, a current of 10^{-8} A is required [101]. The probe diameter can be reduced while maintaining the same beam current by increasing the incident beam divergence. This results in channeling contrast with a resolution of 0.3 μm or even better if bright electron source is available.

2.5.1.2 Contrast within the grains due to deformation

When linear defects combine in a crystal they produce discontinuities in the lattice which separate sections of the crystal with different orientations. If the orientation change across the boundary is greater than 5º, the defect array is called grain boundary and if it is less than 5º, it is called tilt boundary which separates the subgrains within the single grain. These tilt boundaries are formed if the crystal is deformed. A deformed crystal consists of a mosaic structure of cells surrounded by low angle boundaries within each grain which produces irregular changes in orientation [101]. With a small probe size, this structure will give a significant contrast within the grain. These point-to-point changes in orientation from one mosaic unit to another within the grain follows a regular progression and produces contrast called bend contours as shown in Fig. 2.20.

Fig. 2.20 Bend contours in the channeling contrast image from a specimen of rolled gold [101].

Metalworking processes such as rolling, forging, extrusion, and cold heading that involve large amounts of metal flow under heavy pressures are prone to develop regions of extensive local deformation, particularly when this deformation is carried out at high rates [103]. Deformation inhomogeneties are generated when the strain is localized during processing. These large deformations may lead to the formation of shear bands as depicted in Fig. 2.21 and are formed by very thin and elongated cells containing high dislocations density [104]. In the metalworking processes, the interface friction plays a major role. When a metal is compressed, the interface friction generates a zone of dead metal beneath each tool. The greatest strain discontinuity exists at the boundary between these elastically stressed zones and the more homogeneously plastically deforming region next to them.

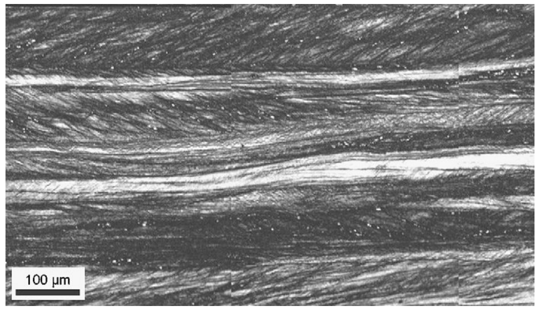

Fig. 2.21 Intensive shear banding in coarse cold rolled silicon steel [104].

2.5.2 Magnetic domain contrast

In order to analyze the micro-magnetic properties of the electrical steel, direct observation of magnetic domains is performed. This can be achieved by magneto-optical Kerr microscope, transmission electron microscope, scanning electron microscope and magnetic force microscope. Magneto optical Kerr microscope has been previously used to image the magnetic domains of NOES laminations [10], [53]. However, resolving finer and complicated domain structure using Kerr imaging is challenging because of its resolution limitation to roughly 300 nm [35]. On the other hand, SEM is used to image magnetic domains with high resolution along with the local texture information which can improve the understanding of orientation and its relationship with domain structure [35]. SEM enables the observation of magnetic domain structures in the specimens by using the deflection of electron beams [105]. The magnetic field associated with the magnetic materials affect the interaction between the electron beam and the material which results in contrast differences in the regions with different magnetization directions, known as magnetic domains [102]. In SEM, the magnetic domain contrast is classified in to three categories: Type I, Type II and Type III. Type I contrast arises from the interaction of secondary electrons with the leakage flux surrounding the material surface. This technique is typically effective for hard magnets, such as Cobalt and Yttrium Orthoferrite, which possesses larger magnitude of leakage flux or stray field. Type II magnetic contrast arises by the interaction of high energy primary electrons with the internal magnetic field and Type III contrast involves the detection of polarization of secondary electrons requiring a specialized detector.

Type II contrast is considered ideal for non-oriented electrical steel and is caused by the deviation of back scattered electrons by the internal magnetic field within the magnetic domains. For the particular beam-specimen magnetization arrangement, the magnetic deflection in alternate domains causes the electron backscatter coefficient to be alternately higher and lower than in the case of no magnetic effect. The domains thus appear in light-dark contrast due to differences in the backscatter coefficient. The specific geometric conditions that must be fulfilled are: the specimen must be tilted relative to the beam and the magnetization vector must lie parallel to the tilt axis as shown in Fig. 2.22. Under these conditions, the cyclotron action of the magnetic field brings the electron closer for one magnetization direction and farther from the surface for opposite magnetization direction. For zero tilt, the cyclotron action of the magnetic field does not cause any change in electron penetration depth in domains of opposite magnetizations. Hence, there is no difference in backscattering coefficient between domains and therefore, no contrast. The contrast is thus dependent on the tilt of the specimen relative to the beam and the optimum tilt angle is 55º.

Since the Lorentz force on the electrons is proportional to the electron velocity, the magnitude of contrast strongly depends on the accelerating voltage. The magnitude of contrast with optimum available SEM conditions (30 KV accelerating voltage, 55º tilt and magnetization vector parallel to the tilt axis) is found to be only 0.3% for iron which has a saturation magnetization of 21000 G [102]. Hence, the magnetic contrast is very weak and high threshold currents and high black level must be used to observe type II contrast. Also, the resolution limit is determined by the probe size or interaction volume and is less than 100 nm.

A recent study by Gallaugher et al. [35] has reported the magnetic domain imaging analysis of NOES laminations done by SEM using type II magnetic contrast and forescatter electron detecter (FSD) attached to electron back scattered diffraction (EBSD) camera. A high magnification image of magnetic domains obtained by type II contrast is shown in Fig. 2.23. The domain structure was observed in different grains and was related to the orientation of the grain using angle β, which was defined as the angle between the closest magnetic axis and the surface of the sample.

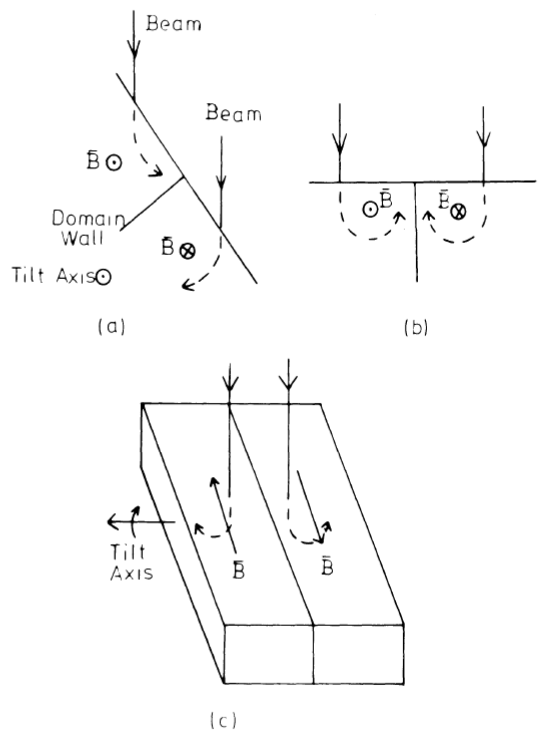

Fig. 2.22 Schematic of mechanism of Type II magnetic contrast [102]. (a) Correct conditions: high tilt (55°) and magnetization parallel to the tilt axis, (b) Incorrect conditions: at normal incidence, the effect of the Lorentz force does not cause a difference in depth of the beam electrons in domains of opposite magnetization, (c) Incorrect conditions: high tilt but magnetization perpendicular to the tilt axis. The cyclotron action does not cause a difference in depth, only rotation in a clockwise or counterclockwise sense in domains of opposite magnetization.

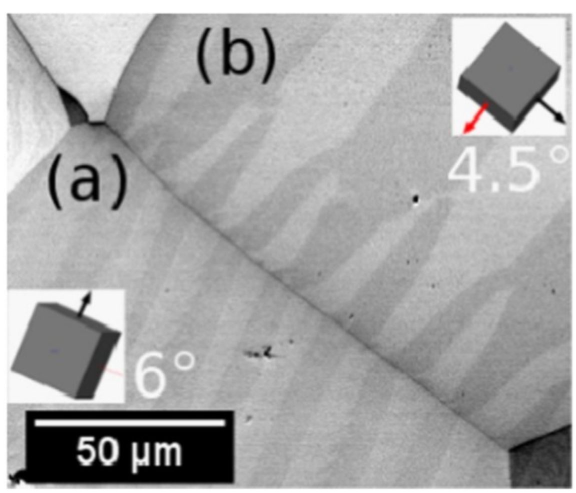

Fig. 2.23 Magnetic domains observed in NOES laminations using scanning electron microscope [35].

2.6 Summary

Manufacturing of the motor core lamination involves various processes such as cutting the laminations to the desired shape, stacking, riveting and clamping as a core inside the motor. The present thesis is more focussed on cutting of non-oriented electrical steel which includes mechanical cutting (punching or guillotining) or laser cutting. Each of these cutting processes is associated with the generation of specific thermal or mechanical stresses, which deteriorate the magnetic properties [53]. The sensitivity of the cutting process depends on the material parameters as well as cutting parameters. The current study mainly deals with the impact of various cutting processes on the microstructure and magnetic characteristics of non-oriented electrical steel as this step of manufacturing is thought to cause the main deterioration and is topical in industry [45].

In a punched lamination, it is difficult to characterize the microstructure near the edge because the property changes can be due to various factors such as residual stresses, plastic deformation, work hardening, increase in dislocation density and grain size modifications. Similarly, the deterioration of magnetic properties due to laser cutting can be due to various factors such as heat affected zone near the edge which exists in some grades of NOES, thermal stresses induced due to temperature gradients while cutting which are difficult to measure and texture modification. Hence, from a material point of view, more research is required in this field, which can bridge the gaps between the magnetic property degradation due to various cutting methods and the actual cause of deterioration in terms of microstructural modification. This will help to improve the manufacturing method of the motor core laminations resulting in lower losses and higher efficiency.

Therefore, from the above literature review on the effect of cutting it is clear that a lot of work has been done in this area but there are certain aspects which are not yet covered. Most of the previous investigations are on the magnetic property deterioration due to cutting with little or no focus on the microstructural or material modification which causes these changes. However, few articles have recently studied microstructure and texture but still many loop holes are there which need to be filled. The present thesis tried to fill some of the loop holes which can bridge the gap between material and magnetic properties in NOES. Some of them are as follows: a) detailed investigation of the microstructure and crystallographic texture in punched NOES lamination, b) the study of elastic and plastic deformation in punched samples at various stages of punching to study interlocking effect, c) relating the microstructure and magnetic properties in shear cut NOES, d) laser cutting NOES and its effect on magnetic properties, e) understanding the reason behind the core loss increase in shear cut and laser cut samples by using techniques such as nanoindentation and SEM, f) comparing the microstructure and magnetic property deterioration for laser cut and shear cut samples. Also, the residual stresses induced by cutting was studied with the help of nanoindentation and magnetic domain structure was observed with the help of SEM.

3. Experimental techniques

3.1 Material used

The material used for the current research is non-oriented electrical steel laminations of different grades. The chemical composition of these laminations was determined by Genitest Inc. and weight % of various elements is given in Table 3.1. These electrical steel grades were cut by different cutting techniques and microstructural and magnetic characterization was performed as shown in the Table 3.2.

Table 3.1 The chemical composition (wt.%) of non-oriented electrical steel grades.

Steel Grade	**Si**	**Al**	**Mn**	**C**	**Co**	**Cr**	**Cu**	**Mo**	**Ni**	**P**	**S**	**Fe**
	(Wt.%)											
35WW300	3.1	.65	.26	.01	.01	.01	.01	.01	.01	.005	.002	95.92
35WW250	3.01	.84	.22	.01	.01	.02	.09	.01	.01	.005	.001	95.75
B35AV1900	3.13	.44	.29	.011	.01	.01	.01	.01	.01	.011	.001	96.1

Table 3.2 List of steel grades used in the current research and the type of cutting.

Steel Grade	**Cutting method**	**Material Characterization**			**Magnetic Testing (SST)**	**Chapter number**
		SEM (BSE & EBSD)	Magnetic Domain Imaging	Nanoindentation		
35WW300	Punching	√		√		4
	Guillotining	√		√	√	6
	Laser cutting	√	√	√	√	7
35WW250	Punching	√		√		5
B35AV1900	Guillotining	√		√	√	6
	Laser cutting	√		√	√	7

3.2 Metallography

3.2.1 Sample Preparation

The samples which have been used for microstructure investigations and nanoindentation measurements were polished. First, the sample was mounted in wax and cut by precision cutting saw. Wax mounting was done to support the sample during cutting and reduce the stress which can be induced while cutting. The cut sample was then unmounted from wax, cleaned and cold mounted in an epoxy resin. Then grinding was done using 600, 800 and 1200 grit SiC paper followed by polishing using 3 µm and 1 µm oil based diamond suspension. It is important to dry the sample using ethanol after every step of polishing to prevent corrosion. Finally, the vibratory polishing was performed for 20 hours using 0.05 µm colloidal silica suspension.

The samples were also prepared in cross section for some part of the research (Chapter 4 and Chapter 5). The cross-section samples were first mounted in wax and cut using precision saw with this cutting-edge perpendicular to the desired edge. Then this sample was mounted using a non-conductive resin. The reason for using a non-conductive resin is that it has better fluidity and less shrinkage after curing. This helped in reducing the gaps between the sample and the mount resulting in better polishing. The mount sample was then polished using the same steps as discussed above up to the final colloidal silica polishing.

It is very important to clean the sample properly after vibratory polishing because the areas where colloidal silica is deposited on the surface are susceptible to corrosion. Therefore, the sample was first cleaned using running water for 5 minutes, then ethanol was used for cleaning followed by drying. This process was repeated 2-3 times until the surface was clear and there were no traces of colloidal silica. If residues of colloidal silica still appeared on the surface, the sample was cleaned using ultrasonic cleaning equipment using alcohol/acetone for 10-15 seconds. After cleaning, the sample was dried and used for nanoindentation measurements. Additional steps were required for high resolution electron microscopy to further improve the surface which includes ion milling the surface and then depositing a thin layer (20 nm) of chromium for electrical conductivity if non-conductive resin was used.

3.2.2 Grain Size Measurement

The grain size measurements were performed according to ASTM standard ASTM E112-10 using lineal intercept method [106]. Horizontal and vertical parallel lines were drawn on the micrograph in order to get a statistically significant number of intercepts per image. After measurement of the number of intercepts for each line, the mean lineal intercept was calculated and converted to average grain diameter. The grain size of the grades used in the present study is shown in Table 3.3.

Table 3.3 The grain size of the steel grades used in the present study.

Steel Grade	Grain size (µm)
35WW300	130 ± 10
35WW250	120 ± 21
B35AV1900	106 ± 13

3.2.3 Texture Measurement

Crystallographic texture of the NOES laminations was examined by a standard Bruker D8-2D diffractometer with Co Kα radiation. Ferritic steels develop characteristic textures during the various processing steps and it is, thus, convenient to depict the ODFs as iso-intensity diagrams in ϕ_2-sections [37]. An orientation is presented in terms of the Miller indices {hkl}<uvw>, where {hkl} describes the crystal plane parallel to the sheet surface and <uvw> the crystal direction parallel to the rolling direction (RD). The texture factor (ratio of volume fraction of {100} orientations along the surface to that of {111}) of the samples was calculated by TexTools software and the values are listed in Table 3.4.

Table 3.4 The texture factor of the steel grades used in the present study.

Steel Grade	Texture factor
35WW300	0.8
35WW250	1.25
B35AV1900	0.87

3.3 Nanoindentation

Nanoindentation is a load and depth sensing indentation technique used for measuring the mechanical properties in thin films and in small volumes of material. A procedure developed by Oliver and Pharr [107] to measure hardness is based on experimentally measurable quantities such as the applied indentation load and the projected area of contact between the material and the indenter. A schematic of indentation load versus depth is shown in Fig. 3.1 where the key parameters can be seen such as peak load (P_{max}), maximum depth (h_{max}) and initial unloading contact stiffness (S). These parameters are used to determine the contact area (A) and consequently, the hardness (H) of the material [107]. The load-depth curve changes with the type of residual stress present in the material as shown in Fig. 3.2. A material subjected to compressive stresses resulted in an underestimation of contact area between the material and the indenter, resulting in an overestimation of hardness. It was determined that the presence of compressive stresses led to an increase of material pile-up about the indenter tip that resulted in an area of contact that cannot be accurately predicted through the use of the standard nanoindentation procedure developed by Oliver and Pharr. Based on this observation, numerous techniques have been developed permitting the identification of residual stresses by measuring the material's resistance to penetration. Suresh and Giannakopoulos have shown that compressive residual stresses behave in such a way to impede indentation and, conversely, tensile residual stresses facilitate indentation [108]. Based on this, they developed a model that assumes an equibiaxial residual stress state, is equivalent to a hydrostatic stress state to which a uniaxial stress state has been added.

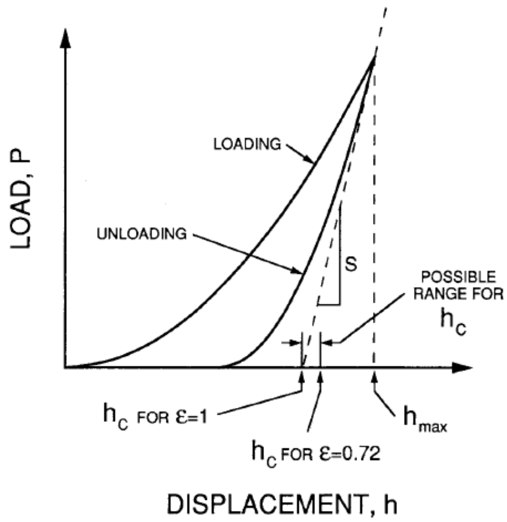

Fig. 3.1 A schematic representation of load versus indenter displacement [107].

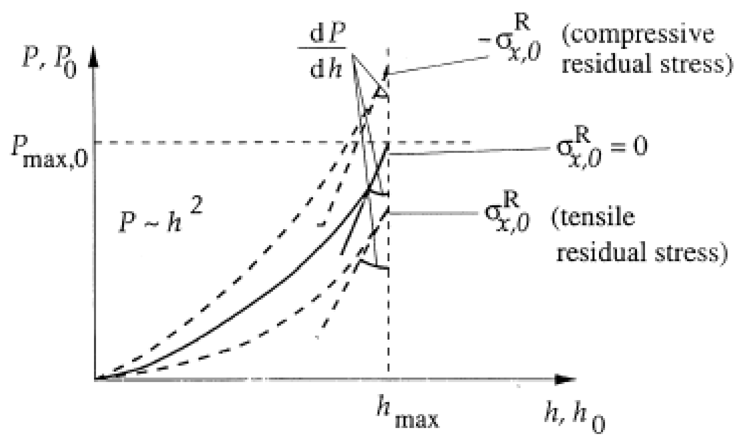

Fig. 3.2 The load depth curves of the sample with and without residual stresses [108].

Nanoindentation measurements were carried out on the sample at room temperature using Hysitron Ubi Indenter. This particular technique was chosen because it permits extremely localized measurement of mechanical properties, permitting measurements on small areas (in nanometers) of material in comparison with conventional microhardness techniques [109]. The standard nanoindenter is equipped with a capacitive transducer, piezoelectric scanner and an optical microscope. The capacitive transducer is the primary component of the machine as it permits the precisely controlled loading and displacement of the indenter tip into the sample, from which hardness and modulus can be obtained. The transducer consists of three plates as illustrated in Fig. 3.3 [109], [110]. The top and bottom plates are stationary and each one carries an alternating current of 180º phase shift with respect to the other, and the middle plate holds the indenter tip and is suspended by springs [110]. When a voltage bias is applied to the bottom plate, this creates an electrostatic force in the center plate which causes a movement of the center plate towards the bottom plate. In this way, load can be applied to the center plate, and hence the indenter.

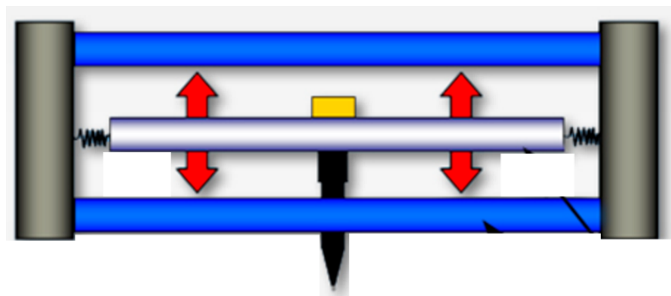

Fig. 3.3 Schematic diagram of a capacitive transducer used for indentation in Hysitron systems [110].

The nanoindentation system was calibrated prior to testing and the area function for the indenter was measured. A schematic of indentation is shown in Fig. 3.4. The contact area (A) is determined from the contact depth (h_c), which is calculated as follows (Eq. 3.1) [110], where h_{max} is the maximum depth of indentation, P_{max} is the maximum load, S is the stiffness calculated from the slope of initial portion of the unloading curve ($S = dP/dh$) and ε is a constant, which is equal to 0.75 for Berkovich indenter geometry [110].

$$h_c = h_{max} - \varepsilon \frac{P_{max}}{S} \qquad \dots(3.1)$$

During the unloading, there is the elastic recovery of both the indenter and the test sample, therefore, reduced modulus (E_r) of the indenter/sample system is given as follows (Eq. 3.2) [110], where ν is the Poisson's ratio and E is the Young's modulus.

$$\frac{1}{E_r} = \frac{1 - \nu^2}{E}\bigg|_{sample} + \frac{1 - \nu^2}{E}\bigg|_{Indenter} \qquad \ldots (3.2)$$

Also, the reduced modulus can be calculated from the stiffness as follows (Eq. 3.3):

$$E_r = \frac{S\sqrt{\pi}}{2\sqrt{A}} \qquad \ldots (3.3)$$

Thus, the hardness is calculated from the nanoindentation using Oliver and Phar technique [107] as follows (Eq. 3.4):

$$H = \frac{P_{max}}{A} \qquad \ldots (3.4)$$

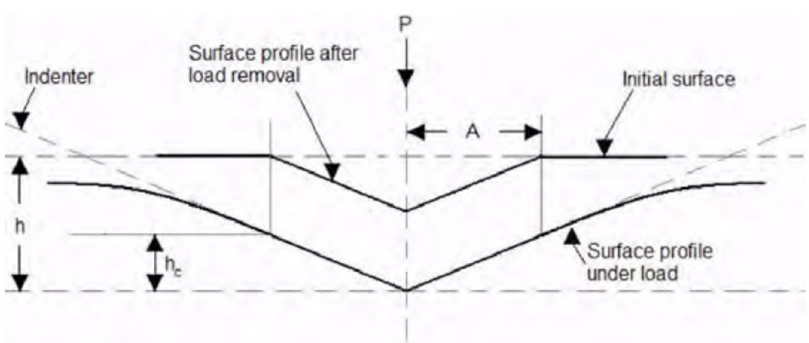

Fig. 3.4 Schematic of nanoindentation [110].

In the present thesis, nanoindentation tests were conducted with a calibrated diamond Berkovich indenter tip. Loading as well as unloading lasted 5s with the maximum force of 5000 μN and the hold period was 2s. Indentation was performed in rows starting from the cut edge of the sample towards the centre with the spacing of ~20 μm between the indents.

3.3.1 Distance of damage from nanoindentation

The cutting of the steel laminations degrades the material near the edge and modifies the material and magnetic properties. The width of the affected region (called as distance of damage in the present thesis) was measured by nanoindentation and scanning electron microscopy. In this section, the distance of damage measured from nanoindentation is discussed. First, the average bulk hardness of the material was determined far away from the cut edge, which can be considered as undamaged region or unaffected region (represented by a solid horizontal line in Fig. 3.5). Then, hardness was measured from the cut edge towards the centre and these hardness values were plotted against the distance as shown in Fig. 3.5 and the point where the solid bulk hardness line intersects the hardness plot was obtained from the graph. The value of x-axis (distance from edge) at this point was termed as distance of damage. In other words, the distance up to which the hardness change extends from the edge with respect to average bulk hardness of the material is referred to as the distance of damage.

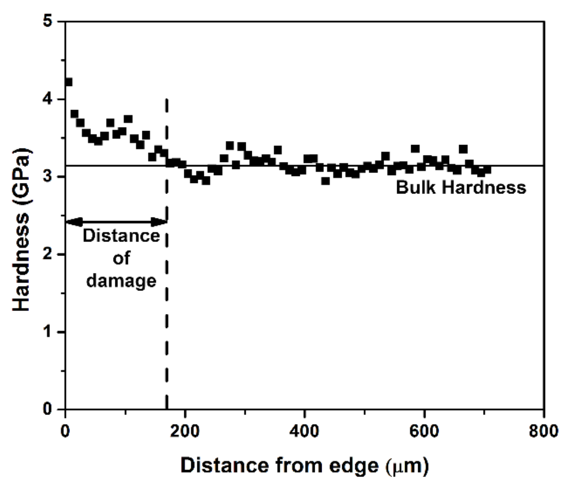

Fig. 3.5 The hardness profile of mechanically cut NOES lamination indicating the distance of damage.

3.3.2 Pop-in analysis

The discontinuity in the load-displacement curve is called the pop-in event and it represents the transition from elastic to plastic behaviour [111]. The pop-in phenomenon is associated with the dislocation activity: nucleation of dislocations, dislocation pile up and dislocation source activation. Therefore, pop-in analysis can be used as a tool to get an idea about the dislocation density and the deformation state of the material. Fig. 3.6 is a typical load displacement curve from nanoindentation, indicating the occurrence of a pop-in event. The pop-in analysis was done on the load displacement curves obtained from nanoindentation performed on the punched and shear cut laminations.

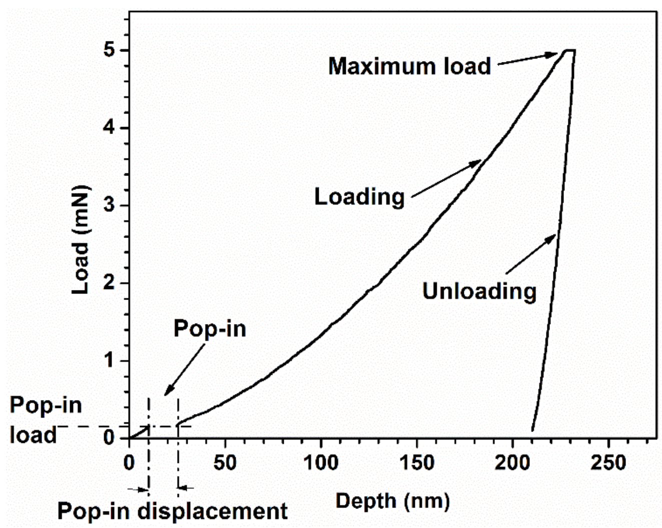

Fig. 3.6 A typical load displacement curve obtained from nanoindentation, indicating the occurrence of pop-in event. Pop-in load and pop-in displacement are highlighted in the figure.

3.4 Scanning electron microscopy

The sample was analysed with a Hitachi SU 3500, SU 8000, SU 8230 and F 50 scanning electron microscopes. SU 3500 and SU 8000 microscopes were equipped with an EBSD camera. The EBSD map was acquired with a 70º tilt and an accelerating voltage of 20 kV. EBSD maps at lower magnification were acquired using SU 3500 microscope in vapour SEM mode. This mode was selected to avoid charging problems due to non-conductive polymer resin in which the steel sample was mount. For high resolution EBSD mapping (using SU 8000), the sample surface was further improved by ion milling using a Hitachi IM 3000 Flat Milling system. Also, to avoid charging and for better beam stability, the sample was coated with chromium with a coating thickness of few nanometers. Chromium was used to make the surface of resin conductive for the better flow of electrons.

The electron back scattered images were captured at an accelerating voltage of 5 kV to facilitate the study of grain morphology after cutting. The images were captured with a pixel density of 1024 × 768.

Magnetic domain imaging was done using the two front detectors attached to the EBSD detector with a high accelerating voltage of 30 kV and high spot intensity of 80, to improve magnetic contrast and reduce signal-to-noise ratio. The sample was tilted by an angle of 70º and images were captured with a dwell time of 200 s and 3 frames averaging. The images were captured with a pixel density of 1024 × 768.

3.4.1 Distance of damage from SEM

The distance of damage was also measured from SEM micrographs. There is a change in contrast due to deformation and residual stress which was discussed in section 2.5. An example of this change in contrast observed near the mechanically cut edge is shown in Fig. 3.7. This distance up to which this contrast effect due to cutting is observed is referred to as distance of damage.

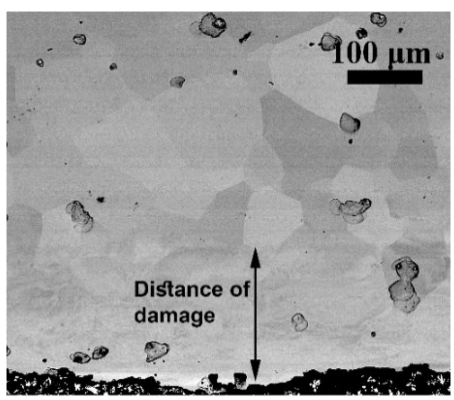

Fig. 3.7 The SEM micrograph of mechanically cut NOES lamination indicating the distance of damage.

3.5 Punching

3.5.1 Punched sample prepared in the laboratory

The punched sample discussed in this section was studied in Chapter 4. The initial dimensions of the 35WW300 lamination were 300 mm × 30 mm × 0.35 mm. This steel lamination was first cut into a square shape with the dimensions of 30 mm × 30 mm and then the coating was removed from both the sides by grinding on 600 or 800 SiC grit papers. Then it was annealed in a vacuum furnace at 750º C for 2 hours followed by furnace cooling to the room temperature. Annealing was done to remove the residual stresses which may be previously induced in the material due to cutting.

Shear punch equipment with a punch diameter of 10 mm was used to prepare the samples. First, the lamination was punched through to determine the load at which it fractures into two pieces which was selected as the maximum load for this study. Then, the sample was punched at different loads but the punching was not complete which means the sample didn't fracture into two pieces. This was done to study the microstructure and mechanical properties during various stages of punching, which could further help in understanding the changes in the material properties due to interlocking process. The process was started at 550 N load where this load was applied by the punch on the lamination and the holding time was set to 2-3 seconds followed by releasing the load and disengaging the punch and the sample. Similar steps were followed for preparing the samples at 1100 N, 1650 N, 2200 N, 3300 N and 4000 N.

3.5.2 Industrial punched sample

The punched sample obtained from the industry was examined in Chapter 5. The steel lamination of grade 35WW250 was provided by TM4 company in the form of motor core lamination as shown in Fig. 3.8. The punching of the steel lamination was carried out using a standard punch where the fracture of the sample into two pieces occur due to shearing process as shown in Fig. 3.9. The punched edge was of the tooth of the core was prepared in cross section and characterized by electron microscopy and nanoindentation.

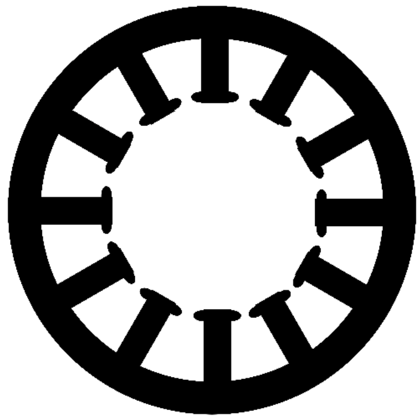

Fig. 3.8 Schematic of the design of motor core lamination.

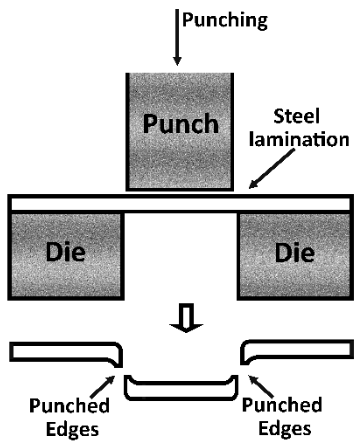

Fig. 3.9 Schematic illustration of designing the sheet metal by punching, indicating the formation of burr near the punched edges.

3.6 Guillotining (Shear cutting)

Shear cutting sample discussed in this section was studied and reported in Chapter 6. The steel laminations of initial dimensions 300 mm x 30 mm x 0.35 mm were cut along the longitudinal direction (rolling direction) into two pieces, each with dimensions of 300 mm x 15 mm x 0.35 mm and also into three pieces each with dimensions of 300 mm x 10 mm x 0.35 mm. These specimens were cut with a commercially available guillotine cutter (Fig. 3.10). The steel sheet was placed on the flat rectangular base of the guillotine and clamped near the cut edge during cutting. The bending of steel was avoided by supporting the steel lamination with polymer sheets during cutting. The guillotine blade was a little inclined, and hence the sample was cut in a skew fashion.

This study was performed on two grades of NOES namely 35WW300 and B35AV1900. The grade 35WW300 was selected because the same grade was used for preparing punched samples (interlocking) and similar grade was also provided by TM4 as punched core laminations. This means the material is same for different cutting techniques which helps in comparing the cutting methods. Here another grade B35AV1900 was also studied because it has different grain size but similar wt.% Si, which means the effect of grain size can be understood.

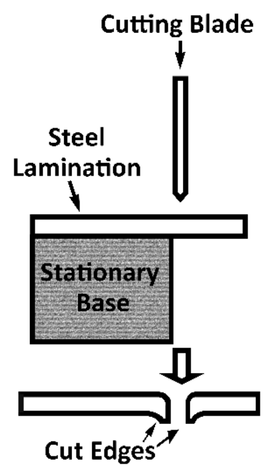

Fig. 3.10 Schematic of guillotining (shear cutting), indicating the formation of burr near the cut edge.

3.7 Laser cutting

The sample preparation discussed in this section was used in Chapter 7. The steel laminations of initial dimensions 300 mm x 30 mm x 0.35 mm were cut by a high-power laser beam along the longitudinal direction (rolling direction) into two pieces, each with dimensions of 300 mm x 15 mm x 0.35 mm and also into three pieces each with dimensions of 300 mm x 10 mm x 0.35 mm. The laser cutting was performed by “Metal CN” company using a standard high-speed Amada FO 3015 CO_2 laser cutting equipment. The focused laser beam was directed at the material resulting in melting of the material and N_2 was used as an assist gas for the removal of cut debris, prevent high temperature oxidation and therefore, improve the overall cut quality.

3.8 Single Sheet Magnetic Tester

The magnetic measurements described in this section were used in Chapter 6 and Chapter 7. A commercial single sheet tester (SST), shown in Fig. 3.11, was used for testing the magnetic properties of the laminations. The measurements were performed using the standard IEC 60404-3 for single sheet tester [75]. A commercial single sheet tester consists of yokes which are made of high quality iron silicon or preferably a nickel-iron alloy (permalloy). Two separate coils are installed in the coil unit: one is magnetizing coil (primary winding) which provides the field intensity and the other is measuring coil (secondary winding) which measures the flux density [112]. The standard sample is a sheet specimen with the dimensions 300 mm × 30 mm and is inserted between the two yokes (Fig. 3.11). The steel specimen acts as a core of the transformer and the vertical double yokes completes the magnetic circuit. The field strength, H, is calculated from the current in the magnetizing coil as follows (Eq. 3.5) [112], where i_p is the current in primary winding, N_p is number of turns and l_p is the magnetic path length of the primary winding.

$$H = \frac{i_p \,.\, N_p}{l_p} \qquad \ldots(3.5)$$

The magnetic flux density, B, is measured from the voltage induced in the secondary winding and is written as follows (Eq. 3.6) [112], where N_s is the number of turns of secondary winding, A_{cs} is the area of cross section and $V(t)$ is the induced voltage in secondary winding.

$$B = \frac{1}{N_S.A_{CS}} \int_{t_1}^{t_2} V\,(t).\,dt \qquad \ldots(3.6)$$

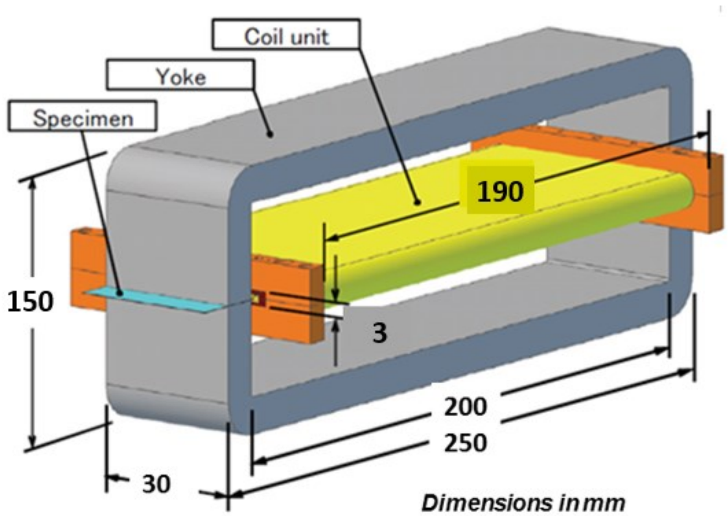

Fig. 3.11 Schematic of a double yoke Single Sheet Tester, indicating the dimensions in mm [89].

The single sheet tester was used in Chapter 6 and Chapter 7 to characterize the shear cut and laser cut samples, respectively. First, measurements were executed on samples before cutting. Later, the samples were cut and again measured its magnetic properties. To avoid the influence of geometrical shape on the magnetic properties, the cut pieces were put together into the testing device and measured simultaneously like a sample with a width of 30 mm. Core loss was evaluated for a range of frequency starting from 3 Hz to 1000 Hz, under sinusoidal waveform, and induction levels from 0.1 to 1.5 T.

4. Study of change in microstructure and mechanical properties in a non-oriented electrical steel lamination due to interlocking

Aroba Saleem, Mengfan Zhang, Dina Goldbaum and Richard R. Chromik

Department of Mining and Materials Engineering, McGill University, Montreal, Canada

This chapter is intended to be published and is focussed on the study of damaged region in non-oriented electrical steel laminations due to punching at different punching loads (which represents the stages of punching from elastic to plastic deformation). Punching is used to simulate the deformed state found in interlocked non-oriented electrical steel. Hardness changes near the punched edge is measured and is related to the microstructural modifications.

4.1 Introduction

The reduction of electric power consumption has become critical as part of the worldwide trend in saving energy and environment [4]. Since electric motors are widely used in a range of electrical equipment for industrial and domestic applications, it is important to reduce the energy loss in them. Non-oriented electrical steel laminations are used in motor cores and the use of electrical steel lamination with lower core losses is an effective way to improve the overall motor efficiency. The manufacturing process of motor core includes various steps like cutting the laminations and clamping them as a core which is assembled in the motor frame. All these processes can substantially effect the magnetic properties of the electrical steel core [4], [46]. Mechanical cutting (punching or shear cutting) is generally used for manufacturing the motor cores whereas laser cutting is used for batch production. Clamping the steel laminations is performed by interlocking or welding in most cases [4].

Interlocking is the commonly used method for automated fabrication of motors and generators where dowels are formed in an early stage of punching. These interlocking dowels act as protuberances on the surface of the laminations and are used to clamp the laminated steel sheets by ramming their protuberances down into next lamination from the corresponding backside holes [113]. The fastened strength is very important for the core making process because imperfect fastening causes troubles during the coil winding. The shape of the dowel also influences the fastening strength [113]. There are different shapes of the dowels used for interlocking such as flat bottom circular, V-cut bottom circular, flat bottom rectangular and V-cut bottom rectangular. An example of the V-shaped dowel is shown in Fig. 4.1. Despite the usefulness of interlocking process, it is known to deteriorate the magnetic properties [4], [7], [113], [114]. The studies on interlocking process in the literature are limited because the degradation of magnetic properties due to interlocking is mainly focussed whereas microstructural modifications or residual stresses induced are least considered.

Fig. 4.1 Photograph of a V-shape interlocking dowel in electrical steel lamination used as motor core [7].

The magnetic property degradation due to interlocking can be explained as follows. The formation of dowels in the laminations require the sheet to be punched at a load lower than the actual punching load at which the material separates into two pieces. From the previous knowledge, punching induces plastic deformation and residual stress in the material near the edge [4], [52], [56], which deteriorates magnetic properties. In addition to the punching damage, residual stress can be induced when the laminations are combined together as a core, which further deteriorates the magnetic properties. Also, the deterioration of magnetic properties is caused by presence of dowels that acts as an obstacle for the flow of magnetic flux in the lamination [7], [113]. Finally, when the laminations are combined, there is a formation of short circuits at the dowels which can also be the reason for deterioration. Kurosaki et al. [4] evaluated the influence of interlocking on the magnetic property degradation and reported that eddy current losses are increased due to short circuits at the dowels which results in the flow of magnetic flux from lamination to lamination. Despite these previous studies, a detailed and quantitative analysis of the factors responsible for magnetic property degradation due to interlocking is still lacking.

The purpose of the present research is to study the material modification due to punching NOES laminations at various stages of punching. A schematic representation of the stages of punching is shown in Fig. 4.2. In a standard punching process, the punch press is used to force a tool, called a punch, through the lamination to create a hole. A die is located on the other side of the lamination to support it during punching. The punch and die are close to the same dimensions causing shearing at the edge where they meet. Shearing occurs by severe plastic deformation locally followed by fracture which propagates deeper into the thickness of the lamination. More specifically, separation of sheet metal during punching involves a consecutive series of events (Fig. 4.2), first of which is when the punch contacts the sheet causing it to roll over. This leads to an increase in the load until it reaches fracture stress of the sheet. At this step, a crack is initiated which produces the rapid breakthrough of the part involving ductile fracture and formation of burr [47]. Usually shearing begins with the formation of cracks on both sides of the lamination which propagates with the application of shear force.

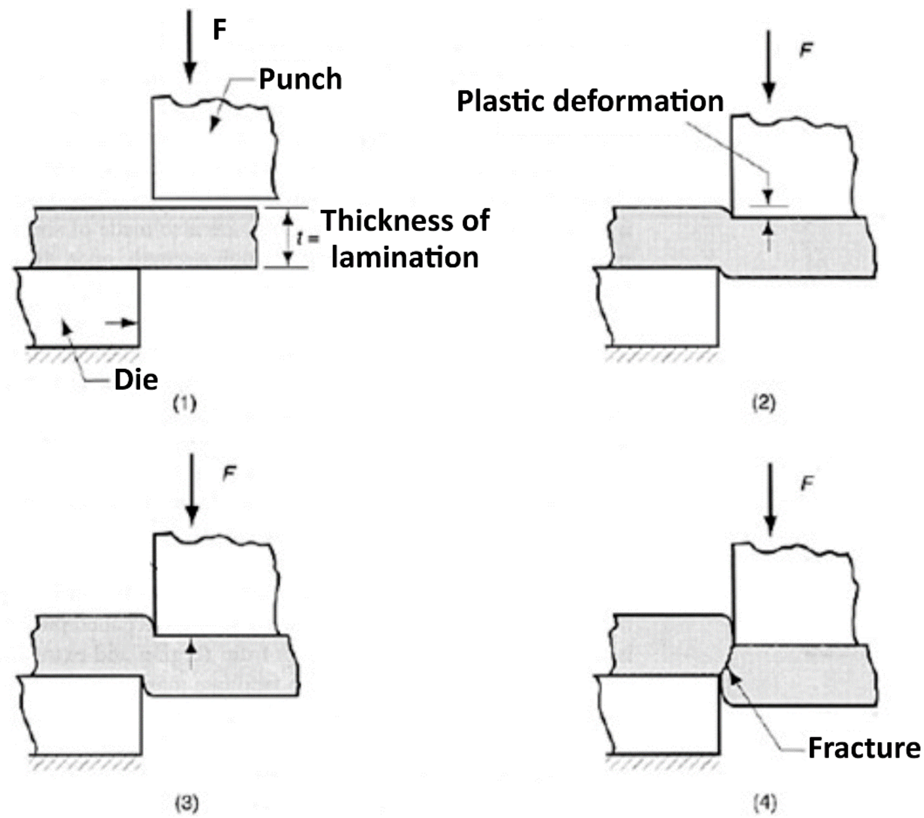

Fig. 4.2 Schematic of the punching process indicating the changes undergone by the material during punching [115].

In the present work, punching was performed on NOES lamination using shear punch equipment at different punching loads until fracture. The microstructure and mechanical properties were analysed in the area affected by punching by SEM and nanoindentation, respectively. Hardness profiles were obtained by nanoindentation near the punched edge of the planar as well as cross section of the lamination. Nanoindentation is useful to study point to point spatial variations of the mechanical properties, including residual stress where hardness decreases with tensile residual stress and increases with compressive [108]. The research conducted by Frutos et al. [116] addressed on the determination of residual stress in sandblasted austenitic steel using nanoindentation techniques focused on the contribution factors to hardening in the specimen in order to avoid the overestimation of the residual stress. Frutos et al. [116] proposed that that the hardness increase is caused by three factors: grain size refinement, presence of residual stress and work hardening. An effort is made in the present chapter to separate the effect of hardness change near the punched edge due to above mentioned factors.

Work hardening was estimated from the pop-in behaviour in load displacement curves. Pop-in events phenomenon, which can be described as a sudden burst of displacement on continuous load–displacement curves, were observed and have been investigated over a wide variety of materials. This displacement discontinuity results from the indenter tip suddenly penetrating into the specimen without the load having to increase during the loading process in the nanoindentation. It is believed that the segment before the pop in of load-displacement curve is associated with elastic behavior whereas the displacement discontinuity is associated the onset of plastic deformation. Therefore, the first pop-in event in the loading process reflects the transition of perfect elastic regime to plastic deformation regime of the material during indentation, which corresponds to a yield point also the onset of plasticity of the material [117]. Hence, the occurrence of pop-in in load-displacement curves depends on the density of pre-existing dislocations in the material. Work hardening increases the dislocation density and hence, reduces the chances of getting pop-in in load displacement curves.

4.2 Experimental methodology

The samples were made from non-oriented electrical steel lamination 35WW300 and were punched at different loads using a standard shear punch machine. The sample preparation was performed as per the following steps:

4.2.1 Cutting the NOES laminations followed by punching

The initial dimensions of the lamination were 300 mm × 30 mm with a thickness of 0.35 mm. This lamination was cut into small square shaped pieces of dimensions 30 mm × 30 mm by shear cutting. Then the coating of the sample was removed from both sides by grinding the sample using 600 and 800 grit size SiC papers. The non-oriented electrical steel laminations are generally coated by electrically insulated coatings to reduce the eddy current losses when these laminations are combined as a motor core [118]. These coatings are mainly organic coatings with a thickness of a few microns. The coatings can cause contamination if the coated NOES lamination is annealed at elevated temperature. This is the reason that the coating has been removed prior to annealing in this study. Annealing of the square shaped samples was done at 750 ºC using a vacuum furnace for 2 hours followed by furnace cooling. The annealing process was important to eliminate any stresses induced in the sample prior to punching.

Punching was performed using a standard shear punch machine at the centre of the square shaped NOES laminations. The shape of the punch was cylindrical with a cross section diameter equal to 10 mm. Hence, a circular impression of 10 mm diameter was made at the centre of the NOES laminations which were punched at lower loads and a hole was created at higher loads. Therefore, the present study deals with the characterization of samples which were punched but the process of punching was not completed to understand the effect of flat based circular dowels in actual motor core laminations.

The punching was performed in steps which are as follows. First, the die and the punch were aligned such that the axis of both the components coincided. Then the sample was placed on the die and fixed in place so that the punch falls exactly at the centre of the lamination. After that the sample was punched and a circular piece was separated from the lamination. This was done to measure the load at which the material fractures into two pieces and was used as a maximum load (4500 N). Then the punched sample was unmounted from the machine and another square shaped sample loaded. The starting load was selected as 550 N and the punch was made to contact the lamination for 3-5 seconds followed by the release of load and unmounting the sample. Similar procedure was used to prepare samples at other loads such as 1100 N, 1650 N, 2200 N, 3300 N and 4000 N.

4.2.2 Microstructural Characterization and Nanoindentation

After punching, the samples were prepared for microstructural characterization and nanoindentation. Each sample was cold mounted in an epoxy resin mixed with conductive Cu-based filler followed by grinding using 600, 800 and 1200 grit SiC papers. Then polishing was done on cloth polishers using 3 µm and 1 µm oil based diamond suspension and finally, vibratory polishing was performed for 20 hours using 0.05 µm colloidal silica suspension. All the samples were prepared to study the surface characteristics of the punched laminations (planar samples) whereas three samples were also prepared in cross section which were punched at lower, intermediate and higher loads. The cross-section samples were prepared by cold mounting in an epoxy resin without conductive filler to ensure better fluidity and less shrinkage of the mount after curing. The polishing was done in a similar manner as was done for planar samples.

Microstructural investigations were done using SU3500 electron microscope with electron backscattered diffraction (EBSD) system attached. Local EBSD maps were obtained in VP-SEM mode at an accelerating voltage of 20 kV. This mode was selected to avoid charging effects when sample with non-conductive epoxy resin was observed under electron microscope. The regions affected by punching were also analysed by back scattered diffraction (BSE) imaging and the average grain size was calculated by mean lineal intercept method [106].

Nanoindentation measurement was done near the punched region in the planar as well as cross section laminations, as shown in Fig. 4.3, using Hysitron Ubi Indenter. The indentation was performed using a diamond Berkovich tip with a maximum load of 5000 µN and 2 seconds holding time at that load. The loading period lasted for 5 seconds and same for the unloading. The distance between the indents was 20 µm for planar samples and 30 µm for cross section samples. The hardness was calculated from nanoindentation measurements using Oliver and Phar analysis [107].

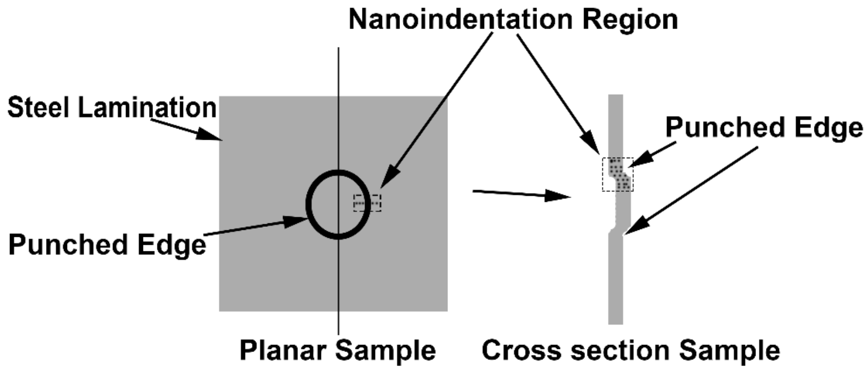

Fig. 4.3 Schematic of the NOES lamination with a circular impression at the centre due to incomplete punching and its cross section. The dotted rectangular boxes represent the area where indentation was performed.

4.3 Results

4.3.1 Initial microstructure

The average grain size of the sample calculated from SEM micrographs by mean lineal intercept method is 130 ± 10 µm [106]. The BSE image of the sample before punching is shown in Fig. 4.4 which shows the regions of different contrast called grains. This contrast is produced by electron channelling which is a function of the angle of incidence and the crystal lattice [101]. The angle between the incident beam and the crystal lattice changes with the orientation of the grains and therefore, the grains with different orientations shows different contrast. When the incident electron beam scans the surface, each grain in the micrograph image shows a uniform contrast level which has a value appropriate to that which would have been obtained at the centre of a channelling pattern obtained from that grain [101]. Therefore, each grain has a different brightness level relative to its neighbours. The grains in the micrograph (Fig. 4.4) are clearly observed with no other contrast effects due to deformation or stress. This micrograph is used as a reference for comparing the effect of punching on the microstructure of the sample.

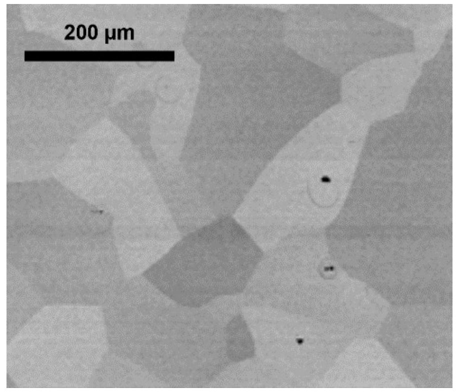

Fig. 4.4 The microstructure of 35WW300 sample before punching obtained by SEM.

4.3.2 Effect of punching on mechanical properties

4.3.2.1 Load-displacement curves

The load-displacement curves of different samples representing various stages of punching from lower to higher loads is shown in Fig. 4.5. These curves are obtained from indents near the punched edge of different samples (punched at different loads) performed by nanoindentation. From the Fig. 4.5, the indentation depth is decreased as punching load is increased which consequently affects the hardness. The hardness is increased as depth decreases for a constant indentation load [107], which means that hardness near the punched edge increases with increasing punching load. Also, from Fig. 4.5, the change in indentation depth of punched samples with respect to the sample before punching is small for lower loads until 1650 N but the depth decreases abruptly for the load of 4000 N. The change in hardness for the samples punched at various loads is explained in the following section.

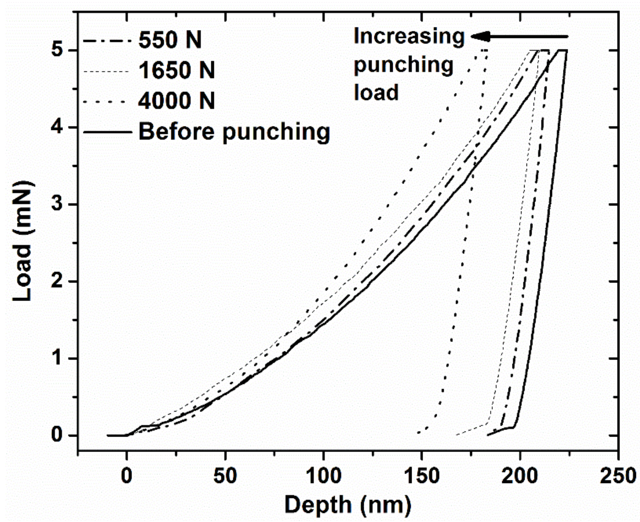

Fig. 4.5 Load-displacement curves for various stages of punching from lower to higher loads.

4.3.2.2 Hardness profiles

The average hardness of the sample before punching is 3.2 ± 0.13 GPa and the change in hardness is observed in the punched region which increases with increase in load. The hardness profiles of the samples punched at different loads are shown in Fig. 4.6. At lower loads (550 N), the hardness is increased from the bulk hardness of 3.2 GPa to the peak hardness of 3.5 GPa whereas at higher loads (4000 N), the value of hardness is increased up to 4.5 GPa. The increase in hardness is significant at higher loads and can be due to several factors such as plastic deformation which leads to work hardening, residual stress and grain refinement [116]. Thus, the hardness of the sample can be divided into different components as follows (Eq. 4.1), where H_0 is the bulk hardness of the lamination before punching, $H\ (G.Ref)$ is the hardness change due to grain refinement, $H\ (Res.Stress)$ is the hardness change due to residual stress and $H\ (W.H)$ is the hardness change due to work hardening.

$$H = H_0 + H\ (G.Ref) + H\ (Res.Stress) + H\ (W.H) \qquad \ldots(4.1)$$

The type of residual stress (tensile or compressive) also affects the magnitude of the hardness where compressive residual stress increases hardness and tensile decreases [108]. In the past, studies on the residual stress analysis in the punched lamination has been done by finite element simulations [57], [60], [68]. It was reported that in addition to plastic deformation near the edge, punching induces compressive residual stresses as well as tensile. The type of residual stress varies from top surface to bottom surface across the thickness of the lamination. Hence, it is difficult to separate the factors that causes the increase in hardness due to punching. Therefore, in the present chapter, individual factors responsible for hardness change are studied at various stages of punching from lower to higher loads.

The reason for hardness change in the punched region is different for various stages of punching. The hardness change is 0.2 – 0.3 GPa at 550 N which is attributed to the residual stresses induced at that load. This is because this load doesn't induce plasticity in the lamination so $H\ (W.H)$ is eliminated from the hardness equation. Also, at lower loads the stress is not enough for the formation of new grains, therefore, $H\ (G.Ref)$ is eliminated. This reduces the hardness equation (Eq. 4.1) to only two components as follows (Eq. 4.2):

$$H = H_0 + H\ (Res.Stress) \qquad \dots (4.2)$$

Similarly, the hardness change for 1100 N and 1650 N load is 0.2 – 0.3 GPa which is due to residual stress induced. At higher loads such as 2200 N, 3300 N, 4000 N and punched through samples, the hardness increase is more than 1 GPa which is attributed to the work hardening and residual stress. At higher loads, the grain refinement component can also contribute to the hardness increase which can be confirmed from the microstructural observations in the next section (4.3.3). These results are in good agreement with the load-displacement curves observed in previous section.

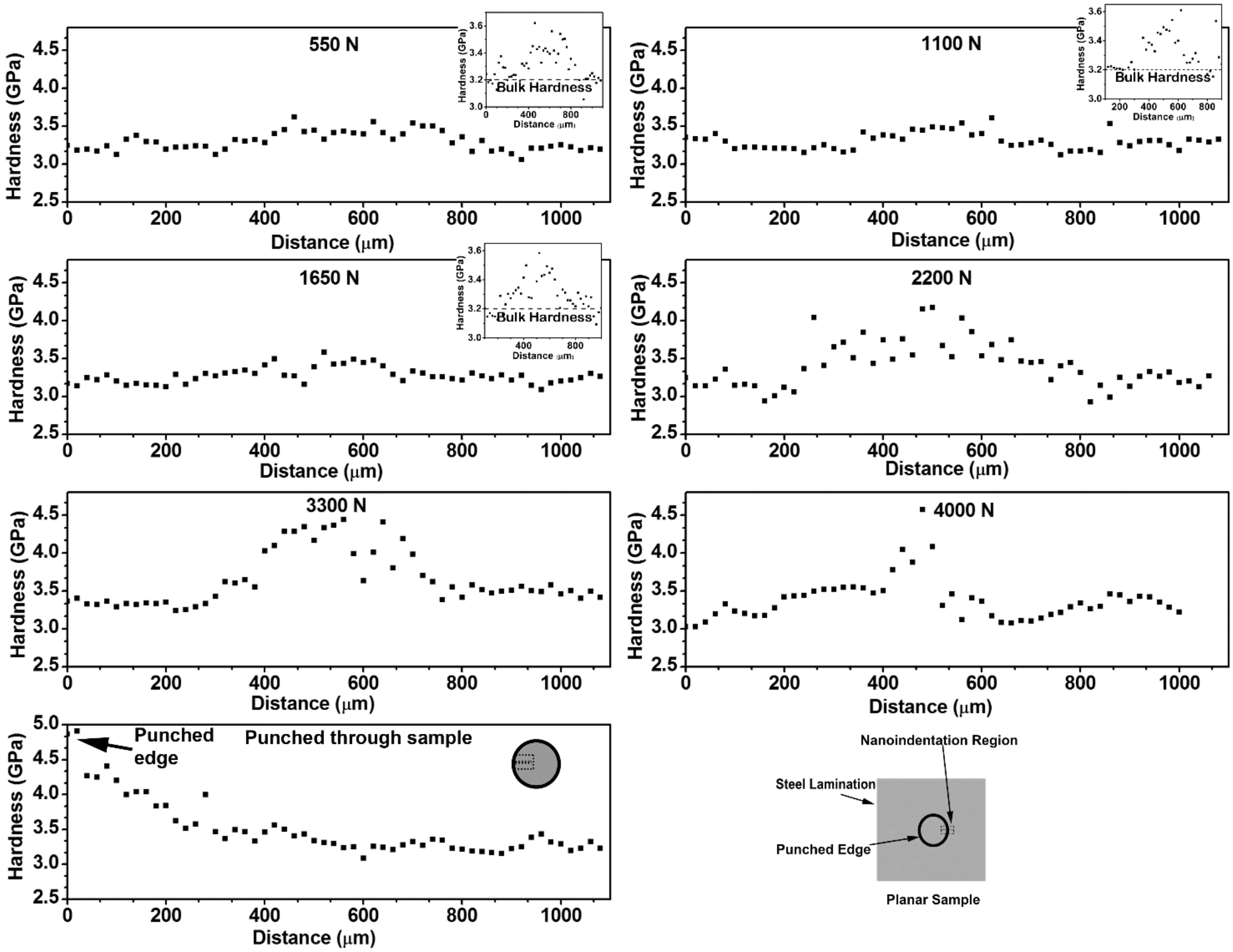

Fig. 4.6 The hardness profiles of 35WW300 steel lamination (planar samples) at different punching loads. The hardness measurements were performed in the punched region of the lamination represented by a black dotted rectangle in the schematic. The small boxes in 550 N, 1100 N and 1650 N represent the hardness values from a section of main graph, showing the peak hardness due to punching.

Further, hardness measurements performed on the samples in cross section and their microstructure is presented in the following section.

4.3.3 Microstructural characterization and hardness measurements of cross-section samples

In this section, the cross section of the samples prepared at different punching loads was examined. The microstructure was examined with SEM with EBSD attached for texture analysis.

Hardness maps were obtained near the punched region by nanoindentation. Hardness profiles were measured across the cross section near the punched region to see the effect of punching load across the depth of this steel. The punching loads selected for this analysis are lower loads such as 550 N and 1100 N and higher loads such as 4000 N.

4.3.3.1 550 N load

The hardness map of the cross section of sample at 550 N load is shown in Fig. 4.7, along with the EBSD map. The hardness variation is not significant in this sample but slight hardness increase is observed near the edges where punching was performed. These results are in good agreement with the hardness profiles in planar samples discussed in the previous section. The hardness change is not uniform across the cross section of the punched edge. Also, the hardness change is only due to the residual stress component as discussed in section 4.3.2.2 because there is no plastic deformation or the grain size change at this load which is clear from the EBSD image in Fig. 4.7. In the present case, maximum hardness is observed near the grain boundary of (111) and (101) grains and grain boundary of (111) and (001) grains (left edge of EBSD map in Fig. 4.7), therefore, this region is considered to be close to the punched edge. Hence, the grain orientation near the punched edge is near (111) orientation and the change in hardness varies across the thickness of the steel with maximum change at the surface where punch or die comes in contact with the lamination. Also, the hardness increase on the other edge (right edge of EBSD map in Fig. 4.7) is observed near the grain boundary of (111) and (101) grains. This means that the effect of punching load is only observed near grain boundaries with negligible effect within the grains. Also, bigger grains are least effected.

4.3.3.2 1100 N load

The cross section of a sample punched at 1100 N and its hardness map is shown in Fig. 4.8. The hardness change is observed across the thickness of the lamination and peak hardness is found close to the surface (both edges of sample in Fig. 4.8) that comes in contact with the die or punch during the punching process. The hardness increase is due to residual stress induced during punching similar to 550 N sample. Also, the peak hardness is observed near the grain boundaries, which means that the grain morphology and orientation affects the residual stress induced due to punching.

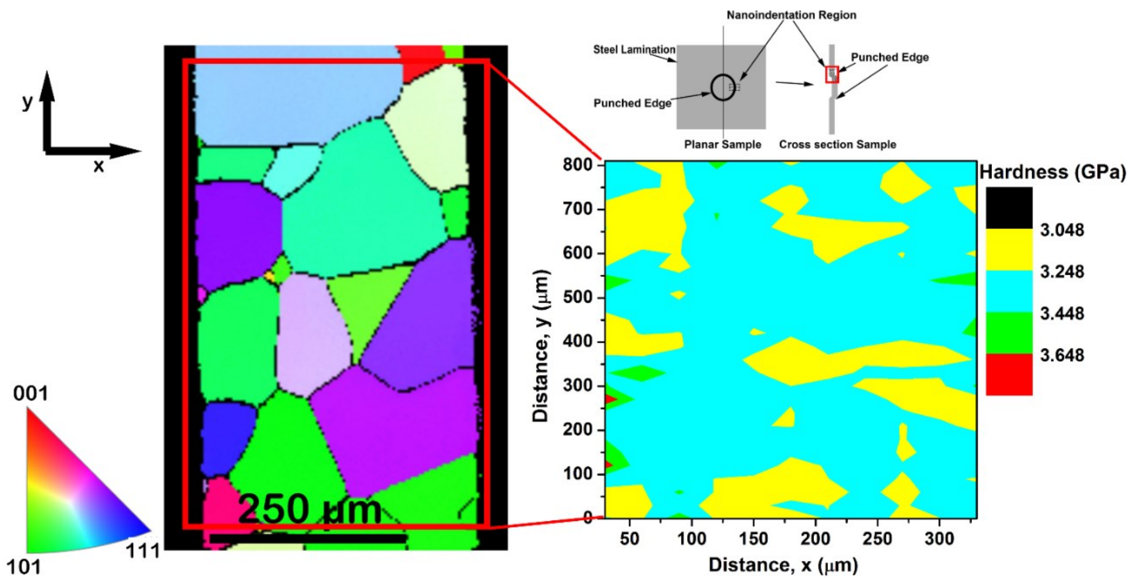

Fig. 4.7 EBSD map for 35WW300 steel punched at 550 N load along with the hardness map across the thickness of steel. The measurements were performed in the cross-section sample near the punched edge represented by red rectangular box in the schematic.

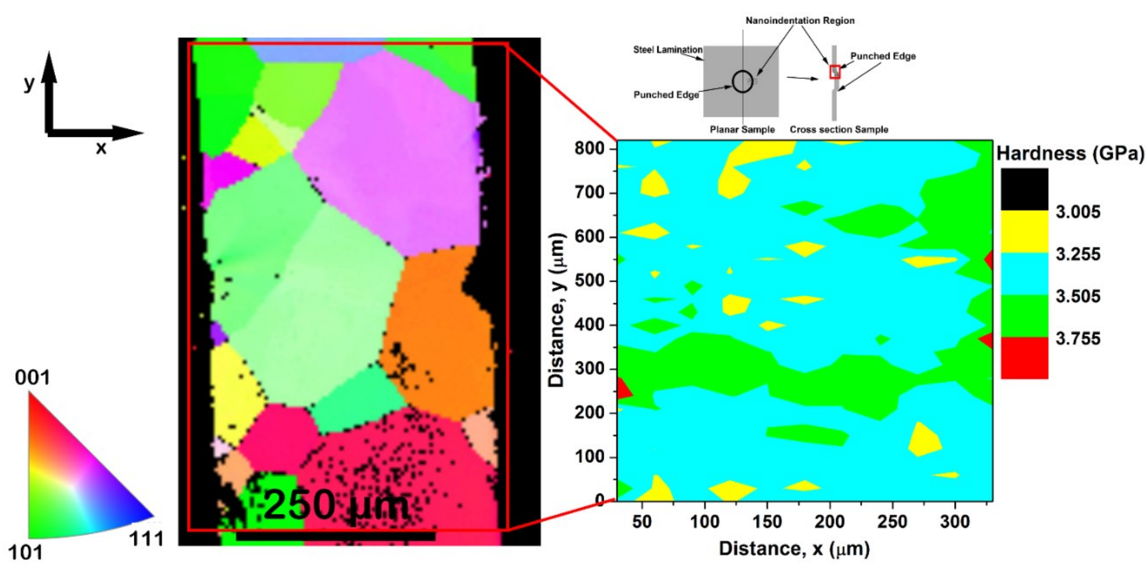

Fig. 4.8 EBSD map for 35WW300 steel punched at 1100 N load along with the hardness map across the thickness of steel. The measurements were performed in the cross-section sample near the punched edge represented by red rectangular box in the schematic.

4.3.3.3 4000 N load

The cross section of a sample punched at 4000 N is shown in Fig. 4.9. A significant hardness increase is observed near the punched edge, which is due to various factors (Eq. 4.1). The lamination is deformed at this load but the load is not high enough to break the lamination into two pieces. From the EBSD maps, the grains are deformed near the punched region and a resulting contrast due to deformation is observed. This means that the color index within one grain is not uniform, indicating the change in orientation within a grain due to deformation. For example, the color of (001) grain on the left edge of EBSD map in Fig. 4.9 is not uniform and has slight variations near the punched edge. However, color index of grains away from punched edge has no such variations. Also, there are regions where the poor EBSD signals are received resulting in black areas in the map. These black areas are found near the surface of the lamination on both sides of the punched edge. The poor EBSD signal in these areas are due to the deformation induced due to punching [119]. Therefore, the hardness increase in 4000 N sample is due to the residual stress induced and work hardening due to plastic deformation. The change in grain size due to punching is not observed in the EBSD map in Fig. 4.9, which means that the grain refinement factor can be eliminated from the total hardness change equation (Eq. 4.1). This may not be true for the areas where black region was observed near the edge. It is because the poor quality of EBSD signals in these areas is due the difficulty of characterizing the regions of deformation with high strains, which may result in the formation of submicron grains [119]. Therefore, the hardness increase near these areas is due to residual stress, work hardening and possibly grain refinement. Also, from the hardness map, the hardness is increased to 3.8 GPa from 3.2 GPa bulk hardness in most of the area near the punched region whereas there are few regions where hardness is increased to 4.3 GPa. Therefore, the hardness increase is not uniform across the thickness of the sample and the factors which are responsible for this increase are different in different areas.

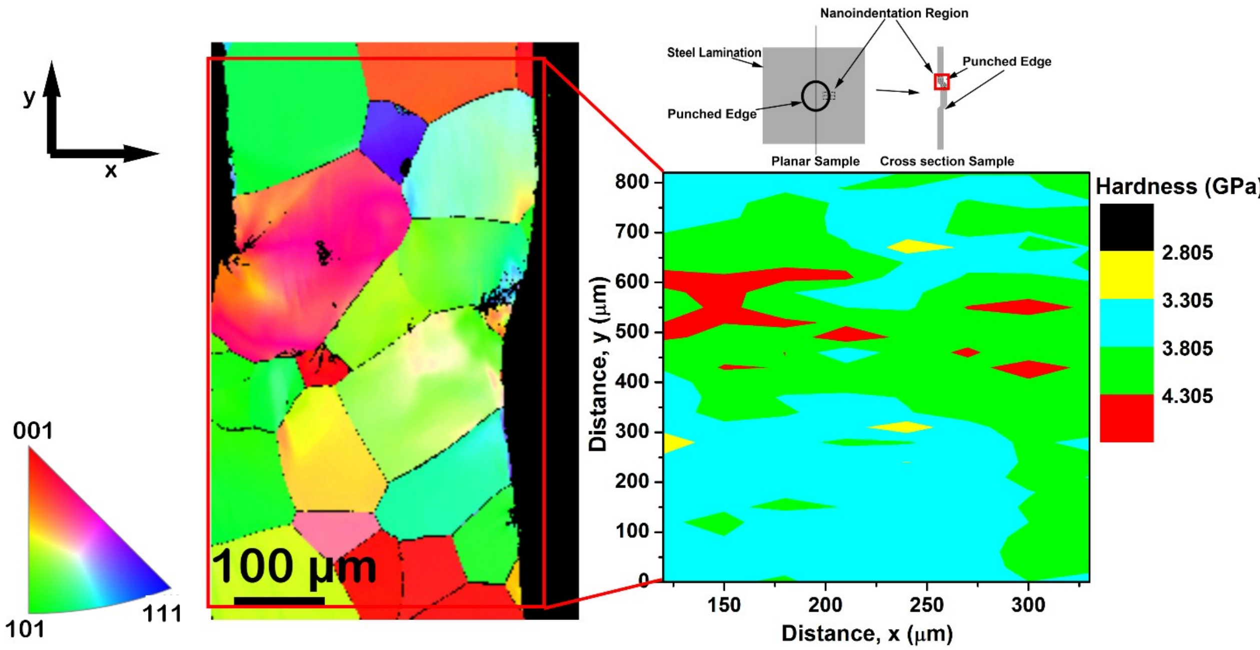

Fig. 4.9 EBSD map for 35WW300 steel punched at 4000 N load along with the hardness map across the thickness of steel. The measurements were performed in the cross-section sample near the punched edge represented by red rectangular box in the schematic.

The back scattered images of the cross section of punched samples is shown in Fig. 4.10. In the first image from left (550 N), the grains are clearly visible due to electron channelling contrast with no signs of deformation seen from the micrograph. The image in the centre is for 1100 N sample and no contrast due to deformation is found. The third image which is 4000N sample clearly shows contrast due to deformation. This contrast appears as contour lines within the grains and is called bend contours [101].

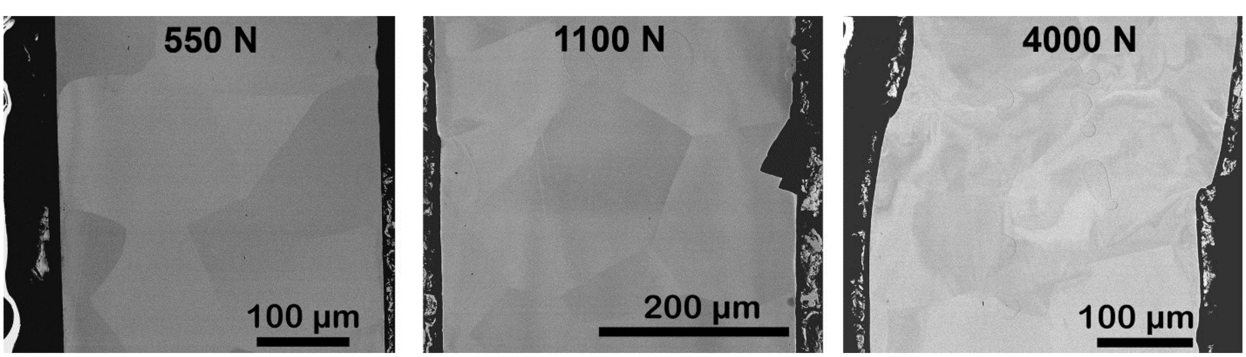

Fig. 4.10 BSE micrographs of 550N, 1100N and 4000N cross section punched samples.

4.4 Discussion

The hardness is increased near the punched edge at various stages of punching and the reason for change in hardness at lower loads is different than at higher loads. The maximum hardness near the punched edge at different loads is shown in Fig. 4.11. The hardness increase at lower loads is not significant (0.2 – 0.3 GPa) whereas hardness increase at higher loads is more than 1 GPa. Therefore, the peak hardness values at lower loads are fitted separately and points at higher load separately. The relationship between peak hardness obtained at the punched edge and load is linear in both low and high load regions. However, the slope of the line in the lower load is significantly smaller than the slope in the high load. By extrapolating both the lines, it is found that these two lines intersect at around 1000 N load and both shows an increasing trend with load.

The line formed from lower load samples is used as to estimate the hardness change only due to residual stress because hardness change at lower loads is attributed only to residual stress whereas the work hardening and grain refinement components are eliminated from the hardness equation (see section 4.3.2.2). However, at higher loads, the hardness increase is attributed to the residual stress and work hardening. Grain refinement component is eliminated since the regions with possible grain refinement are very small (black regions close to the punched edge in EBSD map of 4000 N sample in Fig. 4.9).

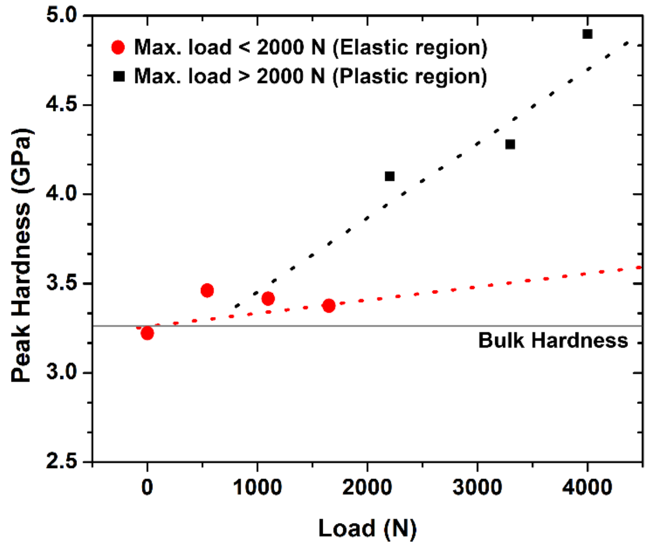

Fig. 4.11 The peak hardness of the sample at different punching loads. Red data points (circle) represent the lower punching loads (elastic region) and black data points (square) represent higher punching loads (plastic region). The red dotted line is the linear fit of the points in elastic region and black one is for plastic region. The slope of these lines gives the magnitude of hardness increase with respect to the bulk hardness value in the elastic and plastic regions.

In addition to the analysis of hardness measurements near the punched edge at various stages of punching, another type of analysis was done to separate the regions of high dislocation density (work hardened and highly strained regions) and residual stress regions. This analysis was done using pop-in phenomena as a tool which is obtained from load-displacement curves and occurs in the from of a discontinuity in the loading curve. The magnitude of the pop-in load or displacement is related to the extent of deformation in the material, which is in turn related to the dislocation density. Zero pop-in load means that the dislocation density is higher enough for smooth transition from elastic to plastic region. This means there is no discontinuity in the load displacement curve, indicating that elastic-plastic transition occurred by the movement of pre-existing dislocations [111]. Thus, the hardness increase in zero pop-in regions must include work hardening effect. For the non-zero pop-in regions, the extent of work hardening is lesser. Pop in load versus distance for the punched sample (planar samples) at 550 N and 4000 N is shown in Fig. 4.12. At 550 N load, there is no zero pop-in region except for few indents. This means the density of pre-existing dislocations is not higher enough to eliminate pop-in effect. Increase in load (4000 N) induces a zero pop-in region. This confirms that the hardness increase at higher loads is due to work hardening and residual stress whereas at lower loads, the hardness change is due to residual stress.

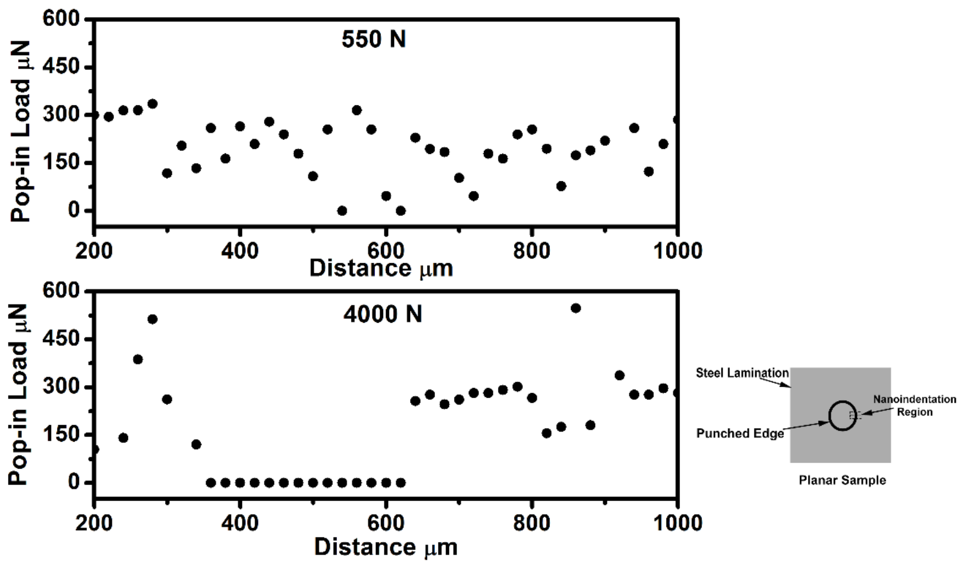

Fig. 4.12 The pop in load vs distance in 550 N and 4000 N punched 35WW300 samples (planar samples). The measurements were performed in the punched region represented by a black dotted rectangle in the schematic.

The pop-in behaviour in cross section samples punched at 550 N and 4000 N is shown in Fig. 4.13. The pop-in load is almost zero in 4000 N sample, indicating the work hardening whereas the pop-in load in 550 N sample is approximately 350 μN near the edge and decreases away from the edge. This non-uniform pop-in behaviour across the thickness of the lamination in 550 N sample is in good agreement with the hardness map observed in Fig. 4.7. A similar trend is observed in pop-in displacement vs distance plots for the 550 N and 4000 N samples in Fig. 4.13.

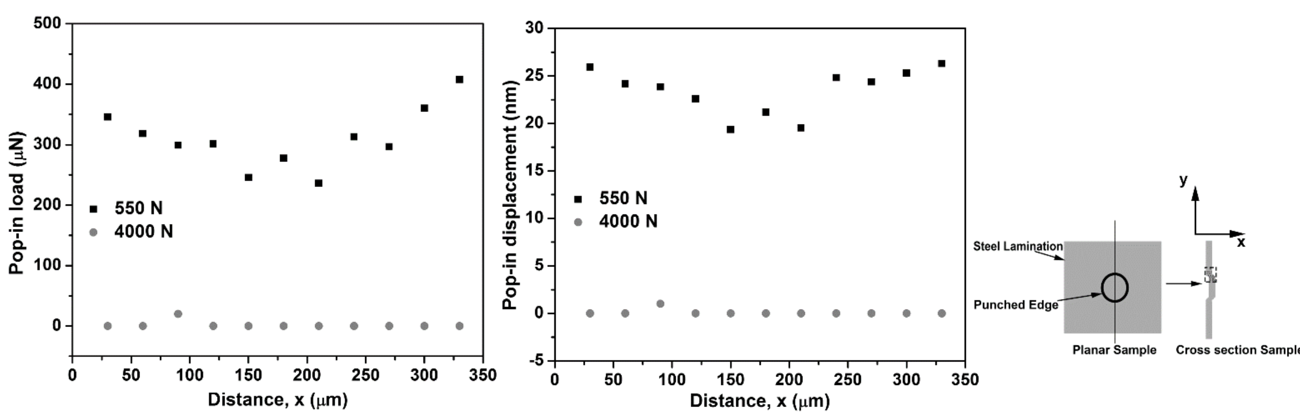

Fig. 4.13 Pop-in load and pop-in displacement vs distance for 500 N and 4000 N samples measured across the thickness of 35WW300 punched steel. The black dotted rectangle in the schematic represents the region where measurements were performed.

4.5 Conclusions

1. The hardness near the punched area increases with the increase in punching load and the hardness increase at lower loads is attributed to the residual stress induced whereas at higher loads, the hardness increase is due to the residual stress, work hardening and/or grain refinement.

2. The pop-in behaviour is more visible at lower loads than at higher loads. Pop-in load/displacement have zero values in deformed regions and near the regions of grain boundaries.

4. The hardness change in cross section samples is similar to the planar ones with the similar peak hardness but the hardness profile is not uniform across the section of the punched steel.

5. The pop-in displacement in samples punched at higher loads is very small compared to those punched at lower loads.

6. The microstructure of the samples shows no change at lower loads but at higher loads bend contours are observed.

5. Microstructure and mechanical property connections for a punched non-oriented electrical steel lamination

Aroba Saleem, Nicolas Brodusch, Raynald Gauvin and Richard R. Chromik

Department of Mining and Materials Engineering, McGill University, Montreal, Canada

This chapter is intended to be published. In the previous chapter, the damaged region near the edge was characterized at various stages of punching. This chapter focusses on the microstructural characterization of the punched non-oriented electrical steel, using higher resolution SEM, for better understanding of microstructural evolution due to punching and other deformation induced changes. Also, the hardness measurements were performed using nanoindentation, in order to understand the relationship between the microstructure and mechanical properties (hardness).

5.1 Introduction

Manufacturing processes used for electrical steels such as laser cutting, guillotining and punching change microstructure and create residual stresses that affects their magnetic performance. Mechanical punching is a low cost, easy to use process to fabricate machine cores from laminations [4], [52]. This method introduces plastic deformation near the edge and therefore, creates a damaged region with increased hardness due to residual stress and work hardening. These effects along with microstructural changes will cause deterioration in magnetic properties such as increase in losses and drop in flux for a given field strength [48], [120].

The effect of punching on the magnetic properties has been investigated in the past by direct magnetic property measurement [4], [5], [49] or study of microstructural modification near the punched edge [48], [50]. However, the study of microstructural changes near the edge due to punching is not well understood. A recent work by Xiong et al. [50] studied the changes in microstructure of the mechanically cut NOES lamination and tried to relate the microstructural changes to the magnetic deterioration. The microstructure of the top surface and bottom surface was separately analysed by EBSD and the increase in misorientation angle distribution near the edge was reported. Similar results were reported by Harstick et al. [48] where EBSD was used to observe local change of properties. The misorientation angle distribution gives and idea about the dislocation density where high misorientation angle represents more dislocations. The dislocations act as pinning sites for the movement of magnetic domains resulting in the increase in losses [48]. In addition to the increase in dislocation density near the edge, punching causes severe plastic deformation, which can change the grain morphology of the sample. There is lack of data in the literature regarding the effect of severe plastic deformation on the grain structure of the lamination because of difficulty in characterizing the deformed region.

The effect of the punching process on the material can be understood as a series of consecutive events. First, the punch comes in contact with the metal sheet causing it to roll over. This leads to an increase of the load until it reaches fracture shear stress of the metal. At this stage of punching, the load increases until a crack is initiated leading to ductile fracture and the formation of burr [47], [50]. Thus, the cross section of the punched edge can be divided into four sections: roll over, the shear zone, the ductile fracture and the burr. As mentioned above, there has been very little work reported in the literature on the microstructure changes near the punched edge [48], [50] and less attention is given to the deformation structure formed during punching. Understanding the mechanical property and microstructure changes due to punching can help the materials engineers and motor designers to better account for the extent of damage and the effect on the magnetic properties.

In addition to the microstructural modifications near the edge, punching induced residual stresses will also lead to the deterioration of magnetic properties. It is difficult to measure residual stresses induced by punching experimentally, however, some researchers in the past used microhardness to measure internal stress due to mechanical cutting [4]. The main issue with this method is that hardness is affected both by work hardening as well as residual stress and, therefore, the hardness change cannot be attributed to residual stress only. Further, some researchers tried to measure residual stresses by x-ray diffraction [65] but the measurement was not limited to the edge of the punched lamination. Therefore, finite element analysis has been done recently by Weiss et al. [57], Fujisaki et al. [68] and kashiwara et al. [60] to analyze the residual stress distribution in the punched lamination.

The present work focusses on the microstructural modifications near the edge due to punching and its relation to mechanical properties. An idea of hardness change only due to residual stresses is given in this chapter by relating nanoindentation measurements with microstructure. Hardness and pop-in displacement are used along with microstructural characterization to determine not just the extent of damage in the steel, but also the nature of the damage in the different regions of the steel. This information on the precise nature of the material modifications due to punching are useful for understanding better the effects of these phenomenon on magnetic properties. Microstructure is analysed by SEM equipped with EBSD.

5.2 Experimental

5.2.1 Material

The material used was punched non-oriented electrical steel lamination of grade 35WW250 which was provided by the TM4 Company. It was punched into a motor lamination design by standard industrial process. In a standard punching process, the punch press is used to force a tool, called a punch, through the lamination to create a hole. A die is located on the other side of the lamination to support it during punching as shown in Fig. 5.1. The punch and die are close to the same dimensions causing shearing at the edge where they meet.

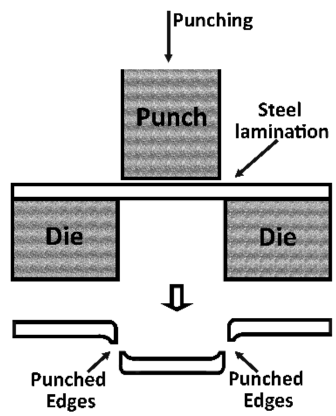

Fig. 5.1 Schematic illustration of designing the sheet metal by punching, indicating the formation of burr near the punched edges.

5.2.2 Microstructural Characterization

For microstructure investigations of the punched edge, Hitachi SU8000 and SU3500 electron microscopes with electron backscatter diffraction (EBSD) systems were used. EBSD analysis and nanoindentation require a flat and highly polished surface. The steel cross sections were cold mounted in an epoxy resin, ground to 1200 grit SiC paper followed by polishing using 3 µm and 1 µm oil based diamond suspension. Finally, the vibratory polishing was performed for ~ 20 hours using 0.05 µm colloidal silica suspension [121]. Lower magnification (~200 X) EBSD and band contrast (BC) maps were obtained by SU3500 in VP-SEM mode (Vapour pressure mode) and at the accelerating voltage of 15 – 20 kV. This mode was selected to avoid the charging effect in the image due to non-conductive resin. For high resolution maps at higher magnification, SU8000 was used. The surface finish of the sample was improved by ion milling before obtaining high resolution maps. To avoid charging due to non-conductive resin mount and for better beam stability, the mount was coated with chromium with a coating thickness of few nanometers. Chromium was used to make the surface conductive for the better flow of electrons.

Areas near the punched edge were also analysed by back scattered electron (BSE) imaging by SU8000 at lower accelerating voltage of 5kV. Grain size was calculated by mean lineal intercept method from SEM micrographs [106].

5.2.3 Nanoindentation

Nanoindentation measurements were carried out on the cross section of the tooth of motor lamination (Fig. 5.2) at room temperature using Hysitron Ubi Indenter. The tests were conducted with a calibrated diamond Berkovich indenter tip. The hardness and reduced modulus of steel specimens were determined from nanoindentation tests using a standard Oliver and Pharr analysis [107]. Loading as well as unloading lasted 5s with the maximum force of 5 mN and the hold period was 2s. Indentation was performed in rows starting from the punched edge of the sample towards the centre with the spacing of ~20 μm between the indents as shown in Fig. 5.2. The first row was started from the roll over side of the cross section and the total number of rows was 24 with ~20 μm spacing between them. The load – displacement curve for one indent is shown in Fig. 5.3 where the indent was performed away from the damaged region. There is a discontinuity in the loading curve at lower loads due to the generation of dislocations which marks the transition from elastic to plastic region. This is called pop-in effect [122].

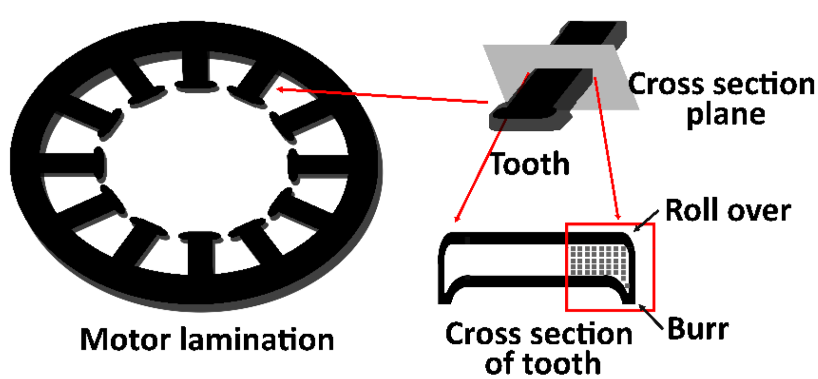

Fig. 5.2 Motor lamination with segmented sections, called as teeth of the lamination, prepared by punching. A single tooth and its cross section is shown to locate the area of interest in the present study. The region within the red box describe the position where nanoindentation and SEM measurements were performed.

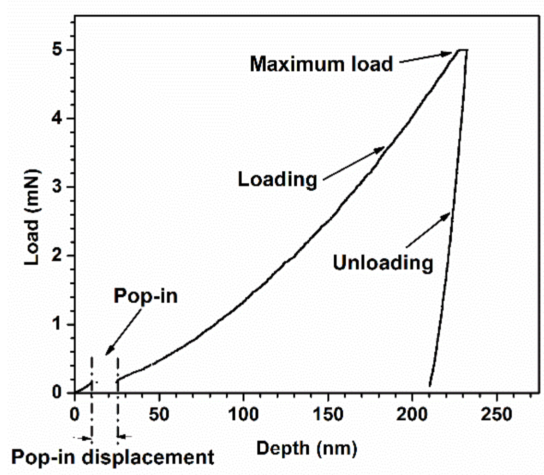

Fig. 5.3 Load versus displacement curve for the given non-oriented electrical steel, indicating the occurrence of pop-in event. The indent was performed in the region away from the punched edge.

5.3 Results

5.3.1 Microstructure and Texture

The edge profile (BSE image) of the 35WW250 punched sample (grain size 120 ± 21 μm) observed by SEM is shown in Fig. 5.4. The image on the left is the region away from the cut edge where undeformed grains are visible due to electron channelling contrast caused by the differences in crystallographic orientation. Right hand side image shows the contrast effects due to severe plastic deformation near the punched edge. Due to plastic deformation, there is generation of dislocations and other crystal defects along with the residual stress that results in the reduction in the quality of electron channelling contrast. There are point-to-point changes in orientation within the deformed grain that results in bands of contrast called as bend contours [101]. The plastic deformation structure is observed along with the severe burr near the edge. This deformation structure appears to be heterogeneous with different microstructural features at different points.

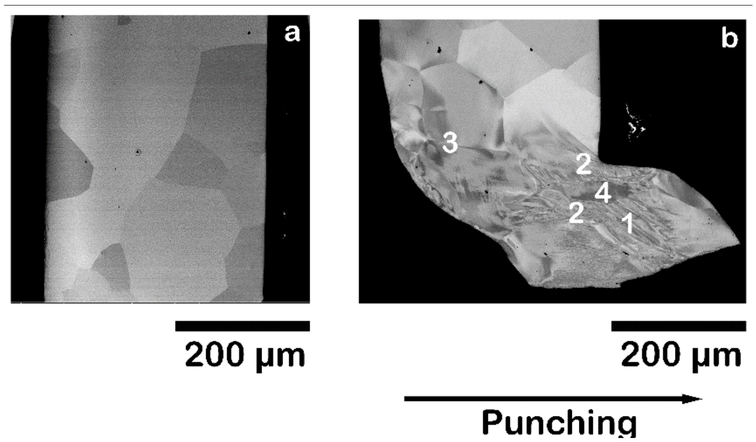

Fig. 5.4 SEM (BSE) micrographs of the cross section of 35WW250 steel. The micrograph on the left (a) is the cross section of the steel sheet away from the edge which shows the undeformed grains. The image on the right (b) is the cross section of punched edge which indicates the formation of burr and other microstructural inhomogenities.

Band contrast and Inverse Pole figure maps (Fig. 5.5) of the punched edge were derived from EBSD. These images can be compared with the SEM (BSE) images in Fig. 5.4 because the microstructural features are highlighted in a similar way. Deformation bands (shear bands) are formed due to severe plastic deformation at the edge which can be clearly recognised as linear features with poor pattern quality (region 2). The EBSD pattern quality generally becomes worse with increasing crystal lattice distortions due to a high dislocation density [123]. The poor EBSD pattern quality indicates that the stored energy of the grain is high whereas high EBSD pattern quality represents low stored energy [123]. The deformation structure developed near the punched edge is highly heterogeneous, which is in agreement with the SEM micrographs. It is because of the fact that the deformation structure depends on the orientation of the deformed grains [124]. There are regions in Fig. 5.5 which corresponds to the high density of shear bands. These shear bands consist of high angle grain boundaries deforming with different slip systems rotated towards higher misorientations [119].

Similar observations were made on another tooth of the punched 35WW250 steel lamination and the band contrast images are shown in Fig. 5.6. Higher density of shear bands was observed at the point where burr started to form (region 2). Elongated grains are inclined to the punching axis forming a splintered or fish bone microstructure (region 1). The orientation of these grains is near {011} orientation. Similar structure was observed by Hutchinson et al. [124]

in {011} oriented grains in cold rolled steel. The only difference in the figure is that there is no undeformed grain within the burr section (region 4) as was in the case of previous tooth region (Fig. 5.4 and Fig. 5.5). So, in general there are at least three microstructural inhomogenities that are observed in the punched steel: elongated grains (region 1), shear bands (region 2) and residual stress (region 3).

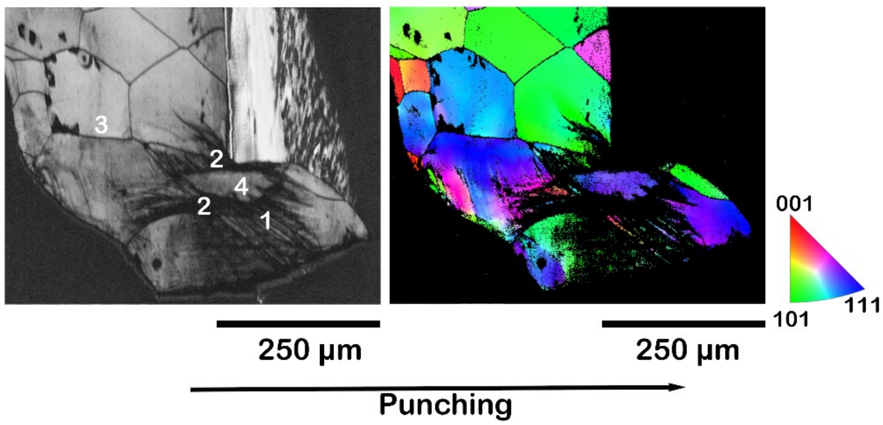

Fig. 5.5 Band contrast and Inverse pole figure EBSD map of the cross section of punched 35WW250 steel. Four regions are highlighted in the figure which matches with those in Fig. 5.4.

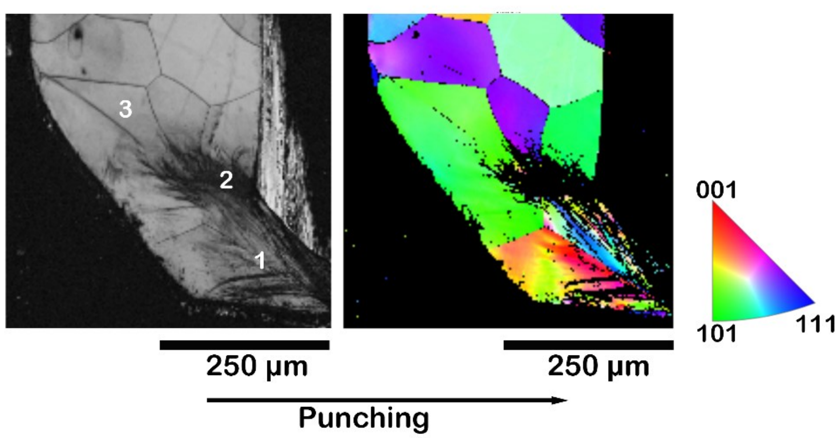

Fig. 5.6 Band contrast and inverse pole figure EBSD map of cross section of punched 35WW250 steel from another tooth of the steel lamination (see Fig. 5.2). The highlighted regions are similar to those marked in Fig. 5.4 and Fig. 5.5.

The band contrast map along with inverse pole figure for the region with elongated grains (region 1 from Fig. 5.5) at higher magnification is shown in Fig. 5.7. These flattened grains are formed in {110} orientations, which is one of the slip planes for bcc metal and are elongated in a direction inclined to the punching axis. This is in good agreement with the fact that these ribbon grains develop from the regions of stable crystal orientations [119]. Also, volumetric stored energy for {110} is higher compared to {111} and {100} which means slip starts on {110} orientation [124]. From the figure, it is clear that these ribbon grains can break up into submicron grains at higher strains because we can see shear bands have started forming perpendicular to the ribbon grains.

The development of shear bands is a feature of accommodating large strains. Different sets of shear bands are observed in the sample as shown in Fig. 5.4 and Fig. 5.5 (region 2). Individual shear bands become hard to resolve by SEM but it can be seen that shear bands consist of submicron sized grains (Fig. 5.8). This means that the new fine grains are not evolved homogenously throughout the deformation structure by severe plastic deformation but mainly inside the shear bands.

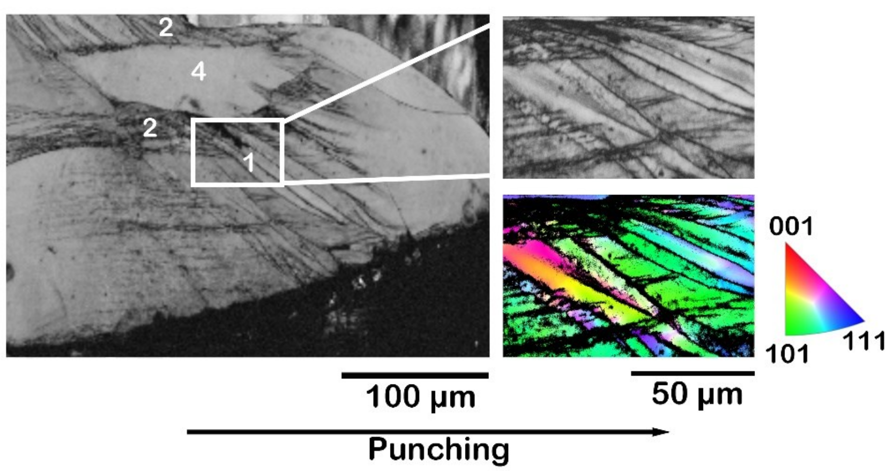

Fig. 5.7 Band contrast and inverse pole figure EBSD map of the burr section (cross section) of punched 35WW250 steel (see full scan in Fig. 5.5). This image also highlights regions 1, 2 and 4 from Fig. 5.5.

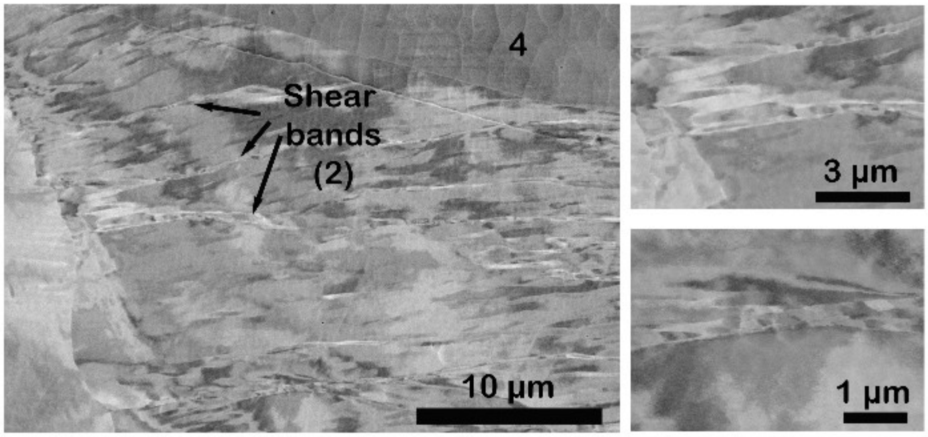

Fig. 5.8 SEM (BSE) images of shear bands observed in the damaged region in 35WW250 steel. It gives a magnified view of region 2 from Fig. 5.4.

The band contrast and inverse pole figure maps of the shear bands are shown in Fig. 5.9. Ultrafine grains with grain size <500 nm are found within the shear bands and these deformation structures are found in those regions which have higher strains. The shear bands are mostly found in the region where burr starts to form (region 2 in Fig. 5.5). In the present case, these bands are observed near the burr region and surrounding the undeformed grain within the burr.

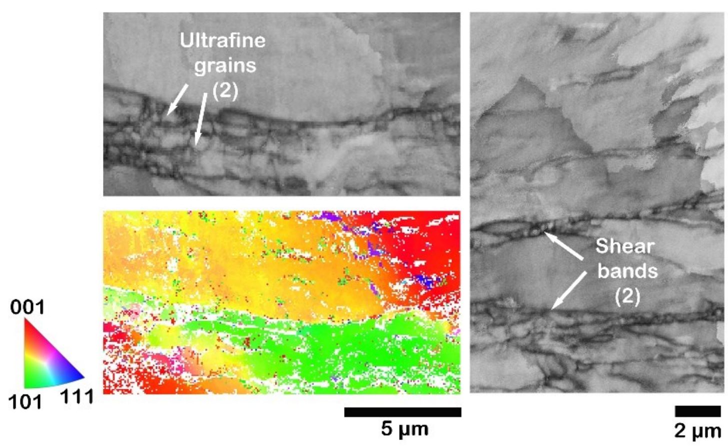

Fig. 5.9 Band contrast and Inverse pole figure EBSD map of shear bands observed in the damaged region in 35WW250 steel (region 2 from Fig. 5.5).

From the electron channelling contrast and band contrast maps (Fig. 5.4 – 5.9), we found that the damaged region is highly heterogeneous with different microstructural features at different points. These regions underwent different levels of strain that results in ultrafine grain development within shear bands in one section and ribbon grains in another. Some grains in the damaged zone are not changed but still residual stresses are observed by channelling contrast imaging (Fig. 5.4) as bend contours within the grains.

5.3.2 Load-displacement curves

The load displacement curves measured by nanoindentation from different regions of the cross section (Fig. 5.4 and Fig. 5.5) of the given steel sample is shown in Fig. 5.10. At a constant load of 5 mN, the indentation depth is maximum for undamaged area (Fig. 5.4 (a)) and decreases in the damaged region (Fig. 5.4 (b)) which means the hardness increases in the damaged area. Also, inside the damaged region the hardness varies from one region to another depending on the distance from the cutting edge which is physically related to the microstructure. The curve for undamaged area shows an obvious pop-in behaviour whereas no pop-in is observed in damaged regions.

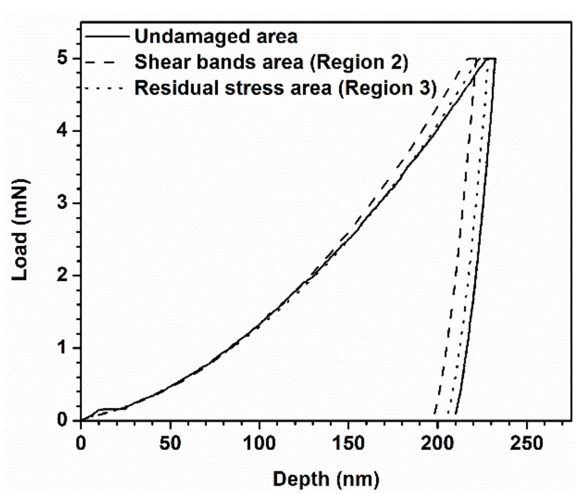

Fig. 5.10 Load versus displacement curves from three different regions of cross section of punched 35WW250 steel. The undamaged area corresponds to the area in the image at the left in Fig. 5.4. Region 2 and region 3 are the regions highlighted in the right-hand side image (b) in Fig. 5.4.

5.3.3 Hardness profiles

The hardness profiles of the cross section of the sample (Fig. 5.4) were obtained from nanoindentation near the punched edge. Hardness profiles were different for different sections: roll over, sheared, fracture and burr section. This change in hardness was attributed to the different microstructural features (highlighted regions in Fig. 5.4 and Fig. 5.5) associated with each section due to different strain levels. Therefore, the total hardness in the damaged region can be written as (Eq. 5.1) [116], where $H_0$is the average hardness of the undamaged region (Fig. 5.4a), $H\ (G.Ref)$ is the hardness change due to grain refinement (region 1 and 2 in Fig. 5.4), $H\ (Res.Stress)$ is the hardness change due to residual stress (region 3 in Fig. 5.4) and $H\ (W.H)$ is the hardness change due to work hardening.

$$H = H_0 + H\ (G.Ref) + H\ (Res.Stress) + H\ (W.H) \qquad \dots(5.1)$$

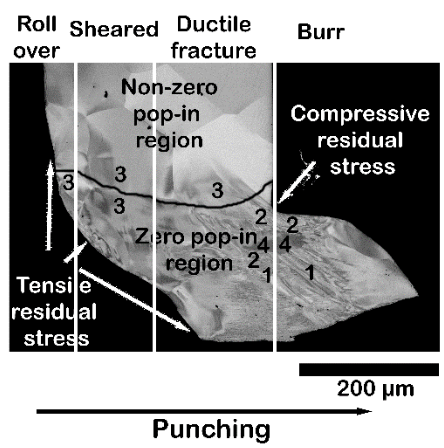

Fig. 5.11 SEM (BSE) image of the cross section of punched 35WW250 steel (see Fig. 5.4) indicating different sections namely: roll over, sheared, ductile fracture and burr.

Work hardening is the strengthening of the material due to increase in dislocation density caused by plastic deformation and therefore, increase in dislocation density is the quantification of work hardening. Region 2 in Fig. 5.5 represents the high dislocation density regions because of poor quality EBSD in those regions. Fig. 5.11 shows BSE image of the sample indicating different sections where nanoindentation measurements were performed. The figure also indicates the type of residual stress induced by punching, based on previous literature [56], [60].

5.3.3.1 Roll over

The hardness as a function of distance from edge for roll over section is shown in Fig. 5.12. The hardness near the punched edge is increased to 3.5 GPa compared to the bulk hardness of the steel which is 3.15 GPa. The microstructure of punched edge is shown in Fig. 5.4 and Fig. 5.5 which clearly indicates that there is no change in the grain size in roll over section but the residual stress is induced (region 3 in Fig. 5.4). The strain in this section was not high enough to start the formation of shear bands or ultrafine grains. Therefore, hardness change for this section can be attributed to residual stress and work hardening.

5.3.3.2 Sheared

The hardness profile of sheared section is shown in Fig. 5.13. The hardness increase in this section is higher than that of roll over and maximum hardness is increased to ~ 4 GPa. The microstructure of this section is comprised of grains with no change in grain size and residual stress induced which can be seen from Fig. 5.4 (region 3).

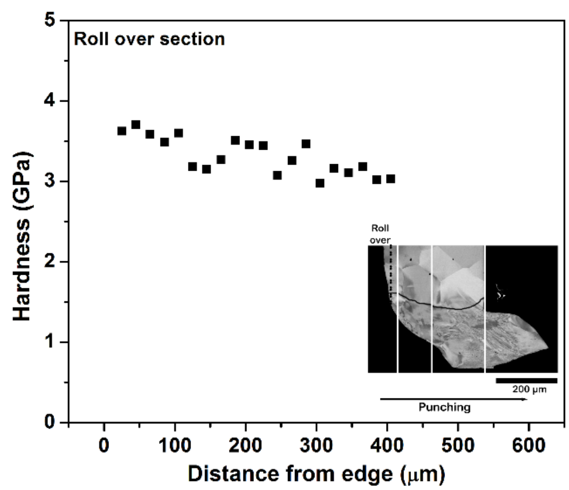

Fig. 5.12 Hardness vs distance from the edge in roll over section is shown. This section mainly consists of region 3 (residual stress), which is clear from Fig. 5.4 and Fig. 5.5.

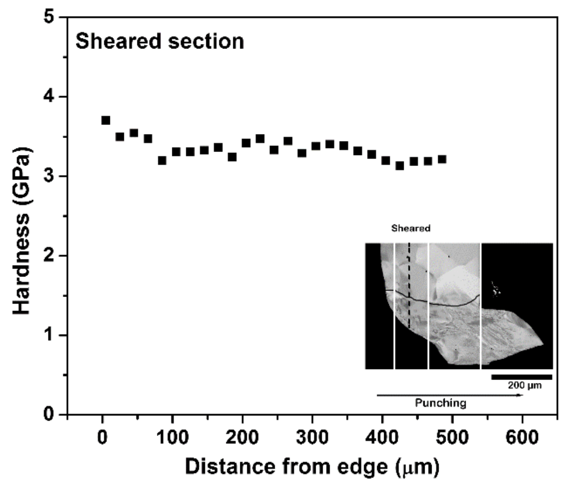

Fig. 5.13 Hardness vs distance from the edge in sheared section is shown. This section mainly consists of region 3 (residual stress), which is clear from Fig. 5.4 and Fig. 5.5.

5.3.3.3 Ductile fracture

Ductile fracture section starts when the applied stress is enough to initiate a crack for the rapid breakthrough of the sheet which involves a ductile fracture. The relation between hardness and distance from the edge is shown in Fig. 5.14. The hardness shows an increasing trend initially, reaches a maximum and then decreases to the average bulk hardness. It is evident from Fig. 5.4 and Fig. 5.5 that fracture section comprises of maximum shear bands (region 2) and deformation heterogeneities. The microstructure of this section consists of ultrafine grains within the shear bands and also residual stress induced grains with no change in grain size. Tensile residual stress is present near the edge which results in lower hardness [56], [57], [60], [68] and then hardness increase can be attributed to higher density of dislocations in the shear band area (region 2 below region 4 in Fig. 5.4). The peak hardness is also due to the combined effect of compressive residual stress and higher dislocation density near the point where burr started to form (shear band area in region 2 above region 4 in Fig. 5.4). Fujisaki et al [68] confirmed the presence of compressive residual stress at this point by finite element simulations. Higher density of dislocations can lead to work hardening and hence, the hardness change can be attributed to work hardening, residual stress and grain refinement.

5.3.3.4 Burr

Severe burr was observed in the punched sample which is formed by plastic deformation. The hardness profile in the burr section shows that hardness is higher than the bulk hardness of the sample throughout this section (Fig. 5.15). The microstructure is comprised of shear bands and elongated grains formed as a result of severe plastic deformation.

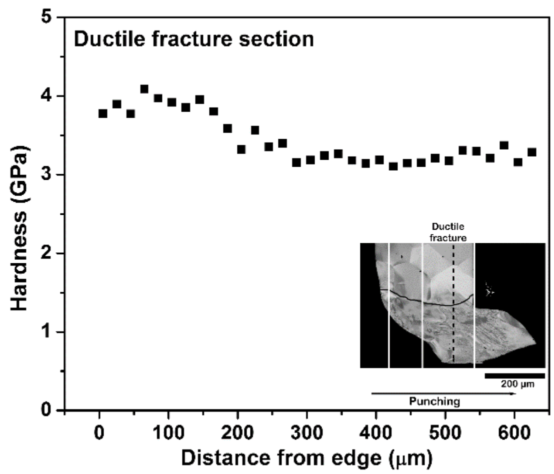

Fig. 5.14 Hardness vs distance from the edge in fracture section is shown. This section mainly consists of region 2 (shear bands) which is clear from Fig. 5.4 and Fig. 5.5. The microstructure in this section also consists of region 1, 3 and 4.

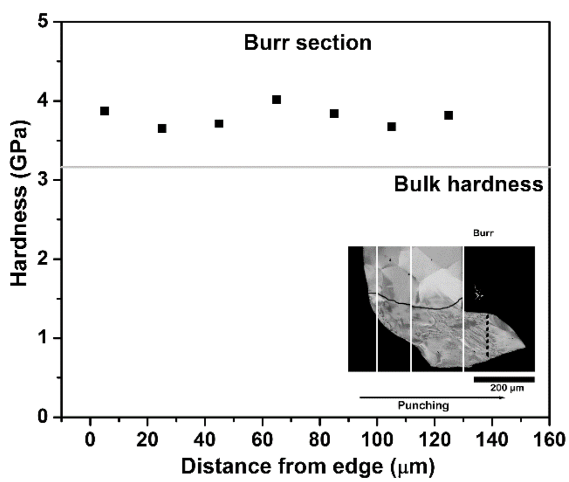

Fig. 5.15 Hardness vs distance from the edge in burr section is shown. This section mainly consists of region 1 (elongated grains) which is clear from Fig. 5.4 and Fig. 5.5. The microstructure in this section also consists of region 2, 3 and 4.

5.3.4 Pop-in analysis

The pop-in analysis is used to separate the work hardened region and ultrafine grained region from residual stress region. Zero pop-in displacement means that the dislocation density is higher enough for smooth transition from elastic to plastic region. This means there is no discontinuity in the load displacement curve indicating that elastic-plastic transition occurred by the movement of pre-existing dislocations. Thus, the hardness increase in zero pop-in regions must include work hardening effect and ultrafine grains. For the non-zero pop-in regions with no change in grain size, the extent of work hardening is less. The pop-in displacement versus distance plots for all the four sections is given in Fig. 5.16. The distance of zero pop-in is maximum for ductile fracture section compared to other sections. There is an increasing trend of pop-in displacement versus distance beyond zero pop-in region for all the sections. Also, zero pop-in displacement is observed for some indents away from the damaged area. This is due to the fact that the indent was on grain boundary, precipitates or other material defects which has higher dislocation densities than the grain interiors [125].

The difference in the pop-in behaviour in damaged and undamaged areas from all the four sections is because of the difference in density of dislocations. The density of dislocations in the damaged region is high, thus the probability of mobile dislocations underneath the indenter is significantly high. Therefore, plasticity can be initiated by the activation of existing mobile dislocations resulting in very low (or zero) pop-in displacement. The region with low dislocation density have lesser mobile dislocations and hence, nucleation of dislocation occurs during indentation resulting in a significant pop-in displacement. The movement of pre-existing dislocations require lower loads than nucleation of dislocations [122]. Also, higher pop-in load corresponds to higher pop-in displacement and vice versa as shown in Fig. 5.17. Hence, the increasing trend of pop-in displacement with distance away from the punched edge can be explained by dislocation theory [111].

Hence, the hardness profiles and pop-in behaviour vary in these four sections as discussed above based on the microstructure. The reduced modulus values at different points were also measured from nanoindentation and plotted against distance as shown in Fig. 5.18. The reduced modulus seems to have a constant value throughout and the average value is around

218 GPa. Therefore, the elastic modulus of the sample calculated from Eq. 3.2, using ν_{sample} = 0.3, $E_{indenter}$= 1140 GPa, $\nu_{indenter}$ = 0.07 [107], is 166.7 GPa.

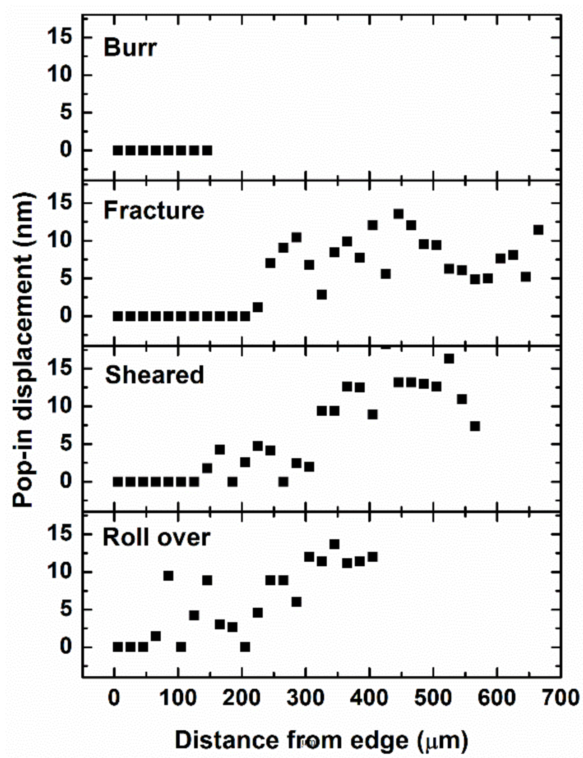

Fig. 5.16 Pop-in displacement vs distance for all the sections in cross section of punched 35WW250 lamination from Fig. 5.11.

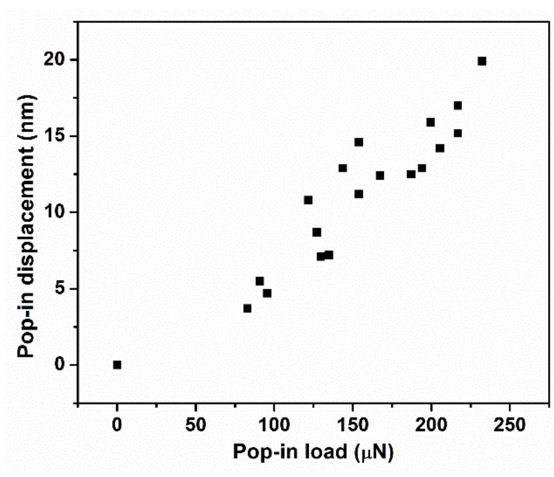

Fig. 5.17 Pop-in displacement vs pop-in load of the cross section of punched 35WW250 steel. The figure indicates that higher loads are required for higher pop-in displacement. The figure corresponds to the pop-in displacement curves from Fig. 5.16 focussing on the region beyond the zero pop-in area.

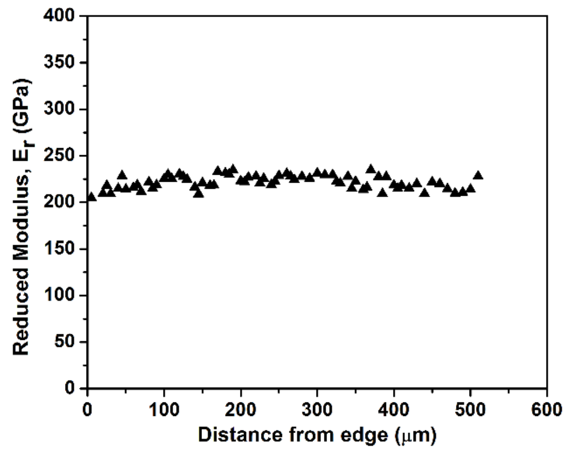

Fig. 5.18 Reduced modulus of the given steel lamination vs distance from the edge for few rows of indents.

5.4 Discussion

Electrical steel is a large-grained ferrite with a relatively low density of dislocations [24]. Punching induces work hardening, residual stress and microstructural changes, such as grain refinement and formation of shear bands. The nanoindentation response of such dramatically different microstructures is very different. During a nanoindentation test on a single grain with relatively low dislocation density, the first stages of plasticity often initiate suddenly and are identified on the loading curve by a so-called "pop-in" [111], [117]. This phenomenon is associated with dislocation activity like dislocation nucleation and dislocation pile ups. There is a strong influence of the density of pre-existing dislocations on the pop-in phenomenon. As the density of pre-existing dislocations increases, the load, frequency and width of the pop-in decrease [111], [117]. Also, a nanocrystalline material will not exhibit pop-in due to interactions of the dislocations with the grain boundaries [126].

Other than the effects on pop-in phenomenon, residual stress also has an effect on hardness [108]. Also, work hardening which results from the pile up of dislocations due to severe plastic deformation near the punched edge affects mechanical properties. It strengthens the material resulting in increase in hardness. Another microstructural feature induced due to punching is grain refinement which increases the dislocation density and hence, increases hardness. All the above-mentioned factors affect the hardness but these effects are often difficult to separate.

The present results explain the development of heterogeneous deformation structure formed due to severe plastic deformation near the punched edge as shown in Fig. 5.4 and Fig. 5.5. The deformation structure contained ribbon grains (elongated grains) corresponding to stable crystal orientations and deformation bands (shear bands) formed from volumes of unstable crystal orientation. This deformation structure evolves by the formation of low angle and high angle grain boundaries. The development of shear bands subdivides the cellular structure and a deformation substructure with a number of mutually crossed bands are evolved at higher strains which was observed in fracture and burr section of the sample. The points of intersection of shear bands can be considered as a preferential site for the development of highly misoriented submicrocrystalline structure [127]. A study by Bowen et al [119] also reported that ultrafine grains are formed by severe plastic deformation in steel.

Punching also affects mechanical properties near the edge. The hardness profiles and pop-in analysis (Fig. 5.12 - Fig. 5.16) of the cross section of the punched sample shows that there are four distinct sections: roll over, sheared, ductile fracture and burr. Roll over section (Fig. 5.12) is characterised by plastic strain and tensile residual stress with no significant microstructural change (Fig. 5.4 and Fig. 5.5). It was confirmed by Kashiwara [60] by simulating plastic strain and magnetic induction. Zero pop-in displacement in this region means higher density of dislocations. The occurrence of pop-in event is linked to the nucleation of dislocations which results in abrupt plastic flow [117]. In a stress-free crystal, the pop-in is primarily the result of homogeneous dislocation nucleation because the maximum shear stress corresponding to the pop-in load approaches the theoretical strength of the materials.

The second section of punched cross section was sheared section (Fig. 5.13) which was characterised by higher hardness near the edge compared to roll over and zero pop-in displacement. Fracture section (Fig. 5.14) showed peaks of hardness at a distance from the edge which was in good agreement with the microstructural observations from the band contrast maps (Fig. 5.5). Severe burr section (Fig. 5.15) was observed which showed zero pop-in displacement over the entire region due to plastic deformation.

The maximum shear stress underneath the indenter for each pop-in load was calculated by the formula (Eq. 5.2) [122], [128], where E_r is the reduced modulus, P is the pop-in load and R is the defect radius of the diamond Berkovich tip which is 200 nm in the present study.

$$\tau_{pop-in} = 0.31 \left(\frac{6\,E_r^2}{\pi^3 R^2} P\right)^{\frac{1}{3}} \qquad \ldots (5.2)$$

The maximum shear stress for pop-in was found to be increasing from 0 to 1.8 GPa (Fig. 5.19) which is less than the theoretical strength of steel. This means that enough mobile dislocations are present in the steel which results in plasticity at lower loads rather than nucleation of new dislocations at higher loads [129]. The cumulative frequency distribution curves for shear stress (Fig. 5.19) shows that the maximum stress for roll over and sheared region reached ~ 1.8 GPa whereas it is 1.2 GPa for fracture section. Also, more than 80 % of pop-ins are activated at lower stresses in fracture region where as around 50 % pop-ins are activated at lower stresses for roll over and sheared section. This means the density of pre-existing dislocations is more in fracture region than sheared and burr regions.

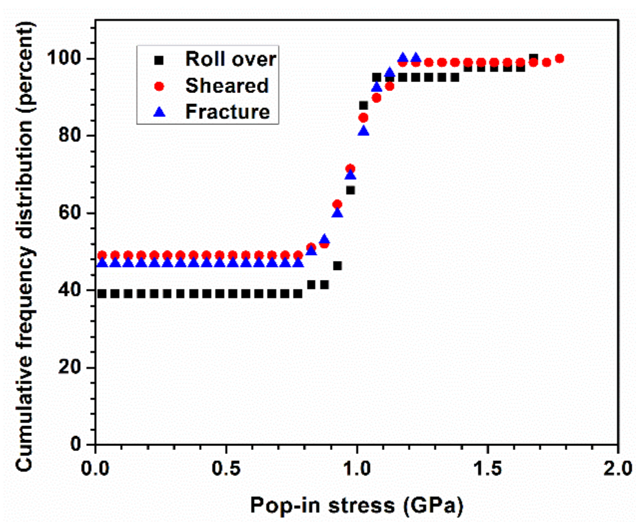

Fig. 5.19 Cumulative frequency distribution of maximum shear stress underneath the tip at the moment of pop-in for roll over, sheared and fracture sections of the punched 35WW250 lamination.

Dislocation density was estimated by the Taylor's relation which relates flow stress with dislocation density (Eq. 5.3) [122], [130], [131], where α is a constant, μ is shear modulus, *M* is Taylor factor, *b* is Burgers vector and ρ is dislocation density. The value of α was chosen to be 0.5, *b* = 0.258 nm, μ = 81 GPa and *M* = 3 [131].

$$\sigma_y = \alpha \mu M b \sqrt{\rho} \qquad \ldots (5.3)$$

Stress was calculated from Tabor's relation as shown in Eq. 5.4 [132], where H is hardness and σ_y is yield stress of the material.

$$H = 3\,\sigma_y \qquad \ldots (5.4)$$

The dislocation density was calculated for all the four regions from hardness profiles in Fig. 5.12, Fig. 5.13, Fig. 5.14 and Fig. 5.15. From the dislocation density calculations and pop-in analysis (Fig. 5.16), the minimum dislocation density required to avoid the pop-in event from the load-displacement curve (i.e. zero pop-in displacement) was estimated to be 7×10^{14} m^{-2}. The magnitude of maximum dislocation densities for burr and fracture section is given in Fig. 5.20, where black dashed line represents the minimum dislocation density above which pop-in displacement becomes zero. The calculated value of maximum dislocation density for punched non-oriented electrical steel is around 1×10^{15} m^{-2}. The dislocation density of polycrystalline ferrite was reported by Schafler et al. [133] and was equal to 3×10^{15} m^{-2}. It was measured experimentally by using x-ray peak profile analysis and the sample (ferrite) was deformed by torsion. The value of dislocation density of deformed ferrite measured experimentally is similar to the calculated value of dislocation density of deformed ferritic steel (punched NOES), which further validates the current measurements and calculations.

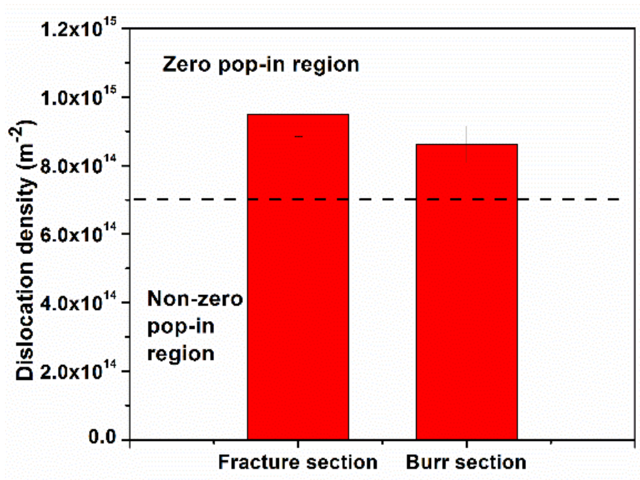

Fig. 5.20 Calculated dislocation density of fracture and burr sections in zero pop-in area. The black dashed line represents the minimum dislocation density above which the pop-in displacement becomes zero.

The summary of the mechanical properties of different microstructural features is given in Table 5.1. The total hardness change near the damaged edge can be attributed to the combined effect of grain refinement, work hardening and residual stress. The type of residual stress is also important to consider because tensile residual stress decreases hardness whereas compressive increases [108]. The amount of hardness increase due to work hardening can also vary depending on the stress and strain level in that particular region which may change the density of dislocations and hence the mechanical properties. So, the process seems to be complex and therefore, we will discuss each section separately.

Roll over region is mainly characterized by stress induced grains with no change in grain size. The stress level is not high enough to form shear bands but the dislocation density increases which is confirmed by pop-in zero distance near the edge (Fig. 5.16). Therefore, the hardness increase is due to work hardening and residual stress as shown in Table 5.1. The sheared section also comprises of stress induced grains with no grain size change. The strain in this section is higher than roll over and dislocation density increased even more. This is confirmed by pop-in zero displacement region extending up to ~140 μm from the edge (Fig. 5.16). The third region which is fracture section having maximum heterogeneities have the total hardness increase by all the three factors. From the above discussion, it can be concluded that the hardness increase can be due to work hardening, grain refinement and residual stress and it is difficult to separate the compressive residual stress effect from the tensile residual stress because of the complexity of microstructure.

From all the above results and discussion derived from SEM and nanoindentation, the distance of damage near the punched edge was found out to be ~300 μm. This damaged zone consists of severely plastic deformation regions and some undeformed grains with residual stress induced. The complex microstructural features of the damaged region near the punched edge can affect the magnetic properties of the electrical steel, such as core loss and permeability. The increase in the number of dislocations due to work hardening and shear band formation increases the pinning sites for magnetic domain movement [52]. This results in the increase in core loss and drop in permeability of the steel lamination. Also, the residual stress induced by punching affects the magnetic properties of the electrical steel lamination where compressive residual stress increases losses and tensile decreases [60]. Therefore, the magnetic properties vary from one region to another near the punched edge of the lamination based on microstructure. This dependence of magnetic properties on microstructure requires an appropriate database to enable the adaption of an accurate model for punching effects during the design process.

Table 5.1 Mechanical properties in different sections of punched 35WW250 steel.

Section	**Microstructural features**	**Av. hardness GPa**	**Max. Hardness GPa**	**Min. Hardness GPa**	**Std. Dev.**	**Possible reason for hardness increase**
Roll over	Region with no grain size change but zero pop-in	3.39	3.68	3.01	0.34	Work hardening + Residual stress
	Region with no grain size change and non-zero pop-in	3.3	3.46	3.08	0.19	Residual stress
Sheared	Region with no change in grain size but zero pop-in value	3.43	3.6	3.1	0.17	Work hardening + Residual stress
Fracture	Ultrafine grains within the shear bands	3.98	4.54	3.48	0.38	Grain refinement +Work hardening + Residual stress
	Region with no change in grain size and non-zero pop-in value	3.24	3.34	3.05	0.13	Residual stress
	Region where burr starts to form	4.39	4.41	4.38	0.02	Grain refinement +Work hardening + Residual stress
Burr	Region with elongated grains	3.61	4.01	3.49	0.31	Grain refinement +Work hardening + Residual stress
	Region within undeformed grain	3.56	3.69	3.3	0.17	Work hardening + Residual stress

5.5 Conclusions

1. The deformation structure formed due to punching is heterogeneous and consists of shear bands and ribbon grains
2. The ribbon grains are formed in more stable crystal orientations e.g {110} for Si-steel
3. The punched edge can be divided in to four sections based on the hardness profiles and microstructure. The sections are named as: roll over, sheared, fracture and burr.
4. The increase in hardness for roll over section is small which may result from plastic strain and tensile residual stress. Sheared section is also characterised by plastic strain.
5. Ductile fracture section showed maximum change in hardness near the edge.
6. Burr section was characterised by plastic strain which was indicated by zero pop-in displacement in the entire section.

6. Effect of Shear Cutting on Microstructure and Magnetic Properties of Non-Oriented Electrical Steel

Aroba Saleem[1], Natheer Alatawneh[1], Richard R. Chromik[1] and David A. Lowther[2]

[1]*Department of Mining and Materials Engineering, McGill University, Montreal, Canada*

[2]*Department of Electrical and Computer Engineering, McGill University, Montreal, Canada*

This chapter is published in IEEE Transaction of Magnetics. The previous chapters (Chapter 4 and Chapter 5) presented the changes in hardness and microstructure near the edge due to mechanical cutting (punching). This chapter focusses on the magnetic property deterioration due to mechanical cutting (shear cutting) and correlates the magnetic property deterioration with microstructural modification near the edge.

6.1 Introduction

Electrical steel sheets are cut in the process of manufacturing rotor and stator components of rotating electrical machines. Cutting operations induce mechanical stresses [4]–[6], [11] in electrical steels, and consequently the magnetic properties are partially deteriorated. The degree of deterioration due to manufacturing and assembly of the motor core components is called the "building factor" [4], and it is very important to understand the effect of manufacturing on the magnetic properties in order to reduce energy loss in motors. The building factor takes into account the type of cutting, amount of cutting per unit volume and the angle of cutting relative to the rolling direction [5]. More detailed knowledge of the effects of cutting on microstructure, material and magnetic properties is required for better selection of material and cutting methods to minimize the building factor and associated losses.

This chapter presents experimental results on the relationship between material properties and degradation of magnetic properties by mechanical cutting. The changes in microstructure and stress state at the cutting edge have been investigated by nanoindentation and electron microscopy. Nanoindentation is useful to study point-to-point spatial variations of mechanical properties, including residual stress where hardness decreases with tensile stress and increases with compressive stress [108]. Material characterization results were correlated to magnetic properties, which were measured with a commercial single sheet tester (SST) for two grades of non-oriented electrical steel.

6.2 Experimental

6.2.1 Materials

Materials tested were 35WW300 and B35AV1900 steel laminations in the as-received state with dimensions of 300 mm x 30 mm x 0.35 mm and also cut specimens (see Fig. 6.1). Specimens were cut along the longitudinal direction (rolling direction) into two pieces, each with dimensions of 300 mm x 15 mm x 0.35 mm and also into three pieces each with dimensions of 300 mm x 10 mm x 0.35 mm.

Specimens were cut with a commercially available guillotine cutter. The steel sheet was placed on the flat rectangular base of the guillotine and clamped near the cut edge during cutting. The bending of steel was avoided by supporting the steel lamination with polymer sheets during cutting. The guillotine blade was a little inclined, and hence the sample was cut in a skew fashion. In the present study, an attempt is made to link the cutting process, the microstructure and the magnetic properties of the materials.

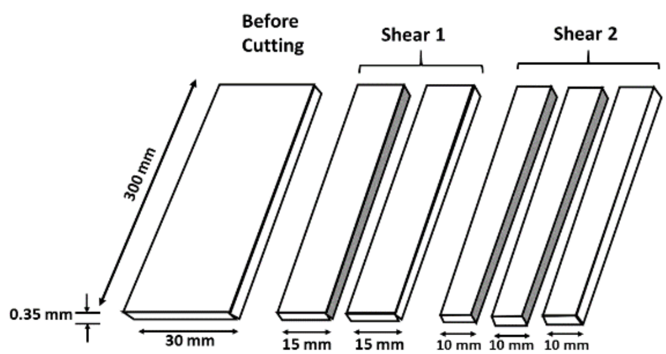

Fig. 6.1 Schematic of samples before and after cut by guillotine (shear cutting).

6.2.2 Magnetic measurements

A commercial single sheet tester (SST) was used for testing the magnetic properties of the laminations. First, measurements were executed on samples before cutting. Later, two piece and three piece cut samples were tested. To avoid the influence of geometrical shape on the magnetic properties, the cut pieces were taped together and placed into the testing device and measured simultaneously like a sample with a width of 30 mm. Core loss was evaluated for a range of frequency starting from 3 Hz to 1000 Hz, under sinusoidal waveform, and induction (flux density) levels from 0.1 to 1.5 T. The main feature of the standard measurement of the magnetic properties is the waveform control of the secondary voltage. The form factor (FF) was considered as a measure for the purity of the sinusoidal flux density waveform, which indicates the accuracy of the measurements. The smaller the form factor (ideally 1), the more accurate the measurements. Fig. 6.2 shows the value of form factor as a function of peak flux density which is almost 1.11 from 0.1 T to 1.0 T for all the excitation frequencies. It shows slight variation beyond 1.0 T but the error is below 1 % which means the measurements are reliable for all the flux density levels and frequencies according to the standard IEC 404-3 [75].

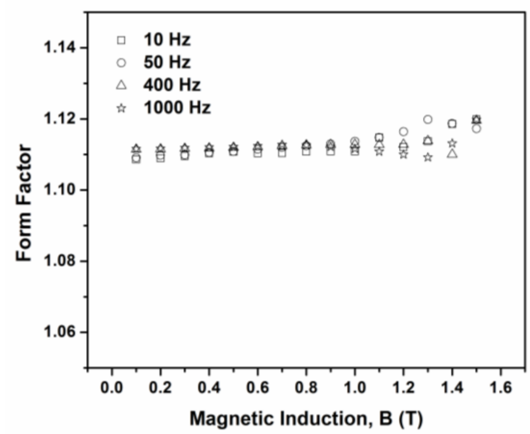

Fig. 6.2 Form factor versus B plot for various frequencies.

6.2.3 Material Characterization

The steel samples were prepared by grinding on 600, 800 and 1200 grit SiC papers and polishing using 3 μm and 1 μm diamond paste to obtain a mirror-like finish followed by vibratory polishing. Specimen microstructure was examined both by optical microscopy and scanning electron microscopy (SEM). The grain size was determined by mean lineal intercept method.

Nanoindentation measurements were carried out at room temperature using Hysitron Ubi Indenter. The tests were conducted with a calibrated Berkovich diamond indenter tip. The hardness and elastic modulus of steel specimens were determined using a standard Oliver and Pharr analysis [107]. Loading and unloading each lasted 5 s with a maximum force of 5000 μN and the hold period at maximum force was 2 s. Indentation was performed in a row starting from the edge of the sample towards the center with a spacing of ~10 μm between the indents.

6.3 Results

6.3.1 Microstructure

The average grain size of B35AV1900 and 35WW300 was found to be 106 ± 13 μm and 130 ± 10 μm, respectively. SEM images of the edge of samples cut by guillotine are shown in Fig. 6.3. In the upper region of each image away from the cut edge, the undeformed grains are visible due to electron channeling contrast caused by differences in crystallographic orientation. However, near the bottom of the images where the specimens were cut, there are different contrast effects due to the plastic deformation near the edge. Formation of defects and residual stress in the crystal lattice results in a reduction in the quality and contrast due to the electron channeling. As such, in the edge region, individual grains are not observable. Instead, there are bands of contrast in the damaged area (Fig. 6.3) caused due to small point-to-point changes in orientation within the deformed grain. These bands of contrast are also known as "bend contours" [101]. The width of the damaged area was determined from the distance from sample edge to where the bend contours disappear. For B35AV1900, the damage extended to a distance of 195 ± 10 μm and for 35WW300 it extended up to 165 ± 4 μm. This difference in damaged area near the cut edge for these two samples may be due to various factors such as grain size, texture near the edge, Si % and yield strength. It is difficult to determine the effect of each factor on the damaged area, as we have only studied these two grades of steel thus far.

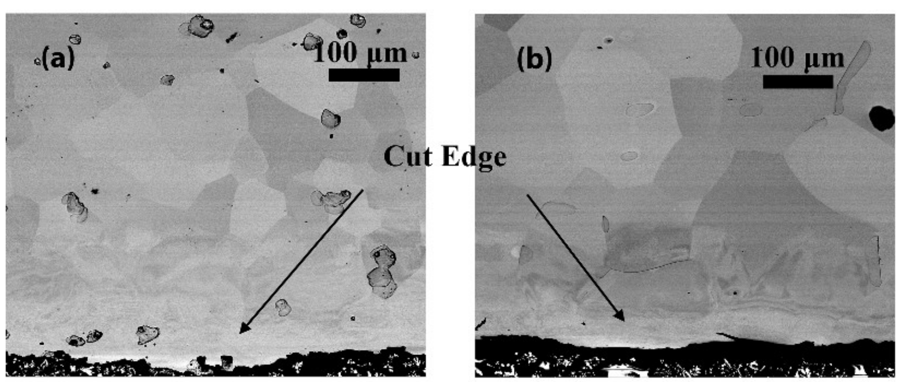

Fig. 6.3 Micrographs of shear cut edge of a) B35AV1900 b) 35WW300.

Fig. 6.4 shows the hardness profiles near the cut edges. The hardness in the vicinity of the cut edge was observed to be higher due to plastic deformation and residual stresses induced by cutting. When the material experiences plastic deformation, energy is supplied to the material, which is absorbed by the lattice resulting in the appearance of microstructural defects [52]. These defects change the mechanical properties of material near the edge and also affect the magnetic domain structure and domain wall motion during the magnetization process [134]. The distance of damage from the cut edge extends up to ~170 μm for B35AV1900 and ~140 μm for 35WW300.

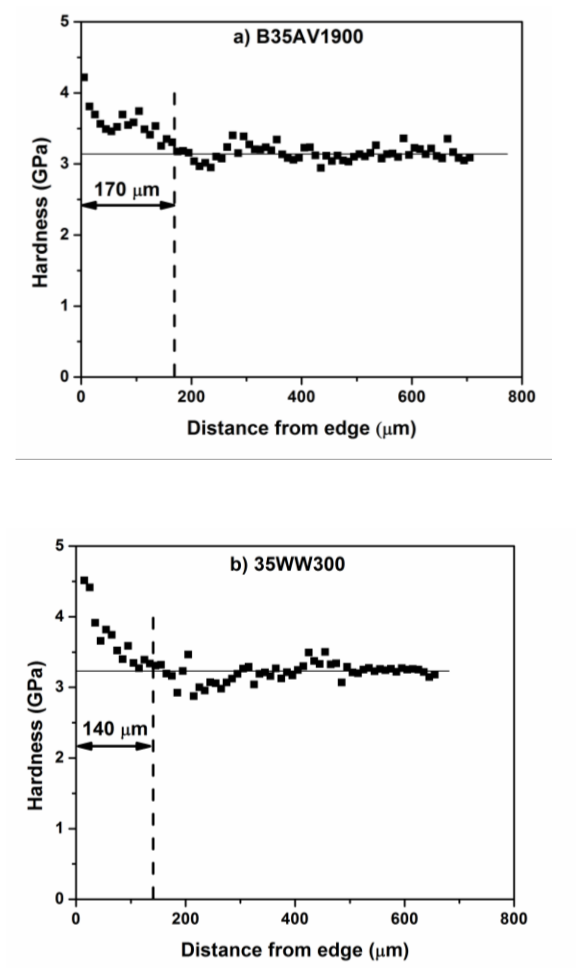

Fig. 6.4 Hardness profile from nanoindentation of a) B35AV1900 b) 35WW300.

6.1.1 Hysteresis loops

The hysteresis loop is the key factor in determining the magnetic behavior of materials and is strongly dependent on various factors such as experimental conditions and the processes involved in manufacturing of the steel laminations. Cutting has the effect of ''shearing'' the hysteresis curves, resulting in lower remanence and permeability as shown in Fig. 6.5. This change in magnetic behaviour can be attributed to the plastic deformation caused by the cutting near the edge. The stress field caused by the deformation hinders the magnetization process of the damaged zone, and makes the cut edge harder to magnetize [11].

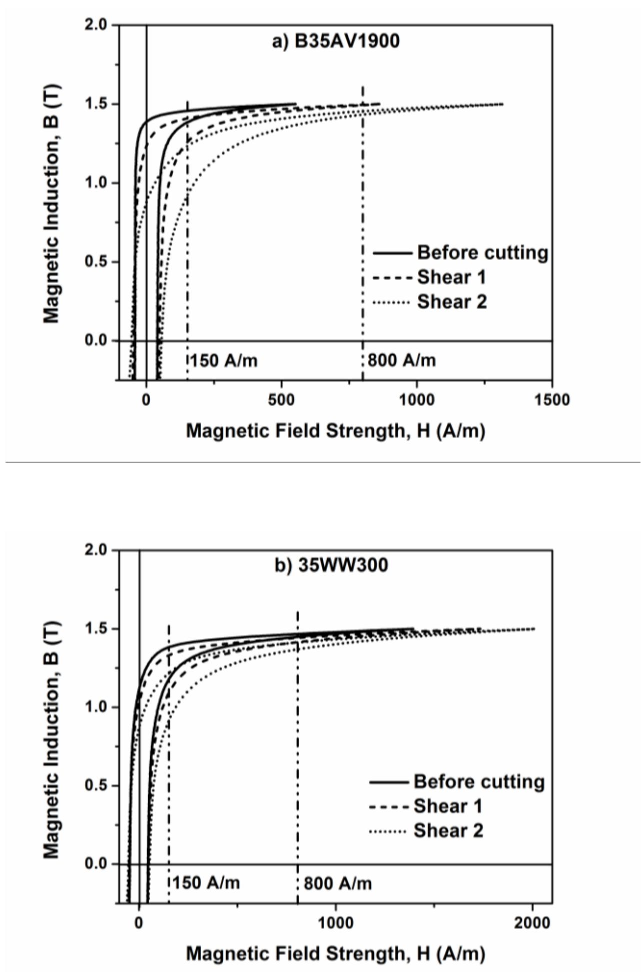

Fig. 6.5 Hysteresis loops at 1.5 T and 50 Hz before and after cutting for a) B35AV1900 b) 35WW300.

6.3.2 Power loss curves

Fig. 6.6 illustrates the effect of cutting on the characteristics of core loss as a function of magnetic flux density (B) for B35AV1900 and 35WW300 grades. The magnetic losses are increased due to cutting in the whole range of flux density from 0.1 T to 1.5 T and the increase in loss is higher for higher frequencies.

The increase in total loss due to cutting is more pronounced in the B35AV1900 when compared to the 35WW300 sample, which is in agreement with the microstructural observations near the edge. The percent increase in total loss at 50 Hz and 1.5 T is ~20% for shear1 sample and ~40% for shear 2 sample for the B35AV1900 grade whereas it is ~9% for shear 1 and 23% for shear 2, for the 35WW300 grade. Similar results were obtained by Schmidt [135], where an increase in loss up to 40% was found, in 1% Si steel, using an Epstein tester. A study by Baudouin et al. [47] found that the magnetic properties are severely deteriorated by guillotine cutting, introducing quality drops in the range of 20-50% for the magnetic parameters such as permeability and losses.

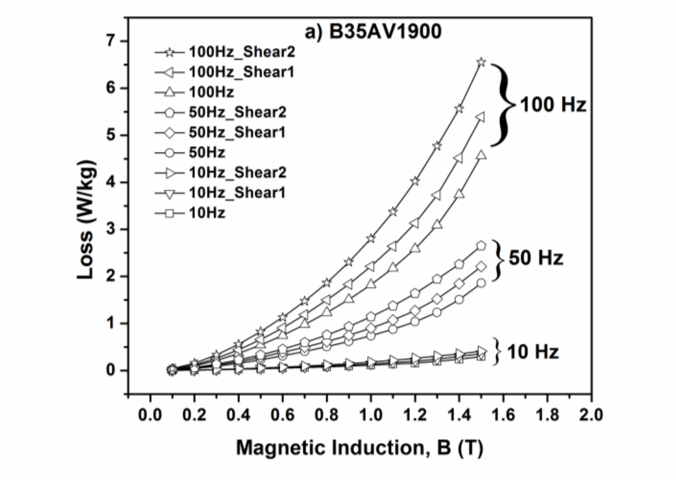

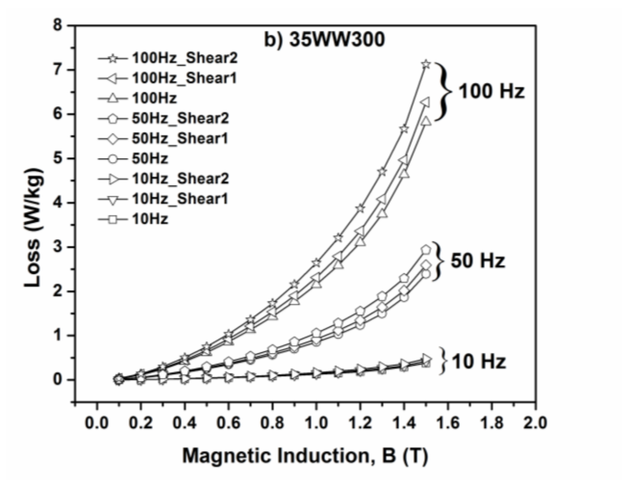

Fig. 6.6 Core loss versus B plots for various frequencies for a) B35AV1900 b) 35WW300.

6.4 Discussion

The changes in magnetization behaviour of electrical steel samples may be correlated with the microstructural changes near the cut edge. There is a deformation affected zone near the edge due to mechanical cutting which causes structural inhomogeneity in the material. The plastic deformation due to cutting induces defects in the damaged area which act as pinning sites for domain movement [52], resulting in an increase in core loss. Also, residual stress is induced due to cutting and strongly depends on stress-strain characteristics of the material [11], which means, materials with different yield strengths will have different magnitudes of residual stress induced by cutting. The residual stress due to cutting also has a component perpendicular to the rolling direction resulting in perpendicular magnetic anisotropy [11]. The magnetic anisotropy affects the hysteresis behaviour of the material, hence, the hysteresis loops are flatter for the shear 2 compared to the shear 1 sample for both the grades (Fig. 6.5).

The magnetization curve of the samples before cutting has the highest permeability and reaches the highest flux density, compared to the cut samples, as shown in Fig. 6.5. Also, it has the lowest coercivity. The induction values for cut samples didn't reach the maximum value for a lower (150 A/m), as well as a higher (800 A/m), field amplitude. The value of flux density was lowered by 2.6%, for the shear 1 B35AV1900 grade, at 150 A/m and 0.6% at 800 A/m. This means that with increase in field amplitude, the deterioration due to cutting decreases. Similar behaviour was observed by Naumoski et al. [10] in punched non-oriented electrical steel, where the average magnetic properties were related to micro-magnetic observations from the magneto-optical Kerr-effect. For a lower field amplitude, poor magnetic domain contrast was found near the edge indicating a degradation of the magnetic properties whereas this region of poor contrast was reduced at higher field amplitude. The magnetic flux density for 35WW300 shear 1 was also decreased by 4.3% at 150 A/m and 1.56% at 800 A/m. The decrease in flux density, due to cutting, for B35AV1900 was less than that of 35WW300 but the increase in coercivity for B35AV1900 was higher (19.3%) than 35WW300 (5.94%). The total loss increase, due to cutting, was more pronounced for B35AV1900 than for 35WW300, as shown in Fig. 6.6.

The percent change in core loss as a function of frequency, at 1.5 T, for B35AV1900 and 35WW300 steel grades, is shown in Fig. 6.7. The "percent loss increase" is higher for B35AV1900 than 35WW300 and it decreases with an increase in frequency for both grades. This can be explained by dividing total loss into its components: a static (frequency independent) hysteresis component and a dynamic (frequency dependent) eddy current loss component [48]. At a lower frequency, the loss change is mainly due to the hysteresis loss component and cutting increases hysteresis loss by increasing pinning sites near the edge [11]. The increase in pinning sites results in increase in coercivity and decrease in remanence.

At higher frequency, the eddy current loss component becomes more dominant and is not significantly affected by cutting [10]. There are many factors which affect the eddy current loss such as, sample thickness, resistivity of the material and skin depth during magnetization [119]. The resistivity increases due to cutting, resulting in lowering the eddy current loss component whereas the skin effect is more observed in cut samples, resulting in an increase in the eddy current loss component. It is desirable to apply loss separation models for calculating eddy current and hysteresis loss components in order to quantify and clarify the magnitude of the effect. This will be the subject of future work.

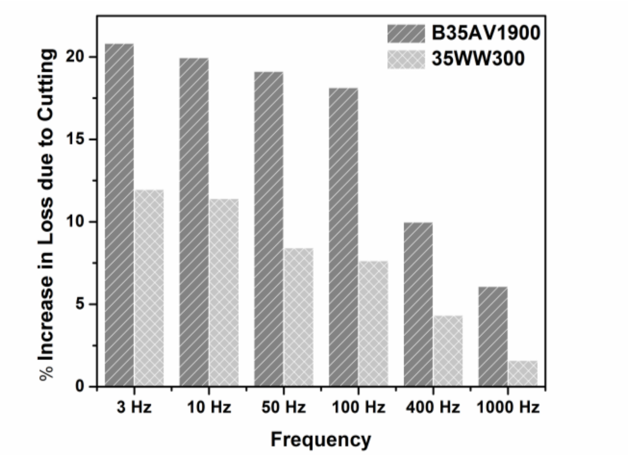

Fig. 6.7 Percent increase in core loss, for shear 1 sample, as a function of frequency, at 1.5 T, for B35AV1900 and 35WW300.

6.5 Conclusions

1. An increase in hardness was observed near the cut edge compared to the bulk hardness of the material, which is attributed to the plastic deformation and the residual stress induced by cutting.
2. Magnetic losses increased and permeability decreased due to cutting and the effect was more pronounced in B35AV1900 than in 35WW300.
3. The percent increase in total loss, for shear 1, was about ~20% for B35AV1900 and ~9% for 35WW300.
4. Losses were also higher for shear 2 than for shear 1 which means that losses also depend on the width of damaged area.

7. Effect of Laser Cutting on Microstructure and Magnetic Properties of Non-Oriented Electrical Steel

Aroba Saleem[1], Natheer Alatawneh[1], Tanvir Rahman[2], Richard R. Chromik[1] and David A. Lowther[2]

[1]*Department of Mining and Materials Engineering, McGill University, Montreal, Canada*

[2]*Department of Electrical and Computer Engineering, McGill University, Montreal, Canada*

This chapter is intended to be published. The work done in the previous chapters (Chapter 4, Chapter 5 and Chapter 6) was mainly focused on mechanical cutting non-oriented electrical steel laminations and its effect on microstructure, mechanical and magnetic properties. This chapter focusses on another cutting type called laser cutting and correlates the microstructure and magnetic properties.

7.1 Introduction

The manufacturing of electric machines leads to the development of residual stresses in the electrical steel laminations, which degrades its soft magnetic properties. As a result, the magnetic properties of the laminations in the finished device are significantly different than the values stated in the datasheet of the steel. This discrepancy can affect the performance and efficiency of the electric machine and therefore, an in-depth understanding of the manufacturing effects is necessary.

Cores of the electric motors are manufactured by cutting the non-oriented electrical steel lamination into a specified shape, stacking and clamping the cut sheets. The mechanical cutting is the most common way to manufacture core laminations whereas laser cutting is used for batch production or prototyping [4]. Laser cutting is a time consuming process but provides flexibility for the design of large or very small complex geometries since it is a non-contact cutting technique [6], [137]. The deterioration of magnetic properties due to cutting is referred to as building factor [11]. More detailed knowledge on the effect of cutting on the magnetic properties of steel laminations is desirable to minimize the building factor and therefore, to reduce the energy loss in motors.

The laser cutting of non-oriented steel lamination and its effect on magnetic properties has been investigated previously [4]–[6], [138]. Quantifying the effect is difficult because the affected area is limited to the cutting edge and the measurement of local magnetic properties is not an easy task. Also, there is a conflicting evidence on the deterioration of magnetic properties due to laser cutting compared to mechanical cutting. Hofmann et al. [53] reported that laser cutting deteriorates magnetic properties more than mechanical cutting. Similar results were found by Kurosaki et al. [4], Emura et al. [5], Shi et al. [49] and Namoski et al. [10] for NOES laminations. However, the results reported by Baudouin et al. [138] and Loisos et al. [55] found that laser cutting process is superior to mechanical cutting in terms of magnetic performance of the laminations. The reason for these varied observations is that the interaction between the material, laser and the assist gas is complex and no direct link can be made between the magnetic properties and the cutting parameters [6]. Also, laser cutting can lead to the modification of microstructure, crystallographic texture, composition and inclusion fraction near the cut edge, due to melting and solidification of the material, which affects the magnetic properties. Inclusions act as pinning sites resulting in the modification of magnetic domain structure and wall motions.

In addition to the microstructural and texture modifications, laser cutting induces residual stresses in the lamination. The residual stresses are harmful for the magnetic performance of the lamination and the experimental determination of residual stress distribution is hard to realize. For that reason, researchers use the observed changes in the magnetic properties as an indicator for the appearance of residual stress after laser cutting [11]. There are recent studies on the local magnetic domain contrast imaging near the laser cut edge by Kerr microscope for estimating the region up to which the stresses are induced due to cutting [10], [53] but the effect of residual stress on the magnetic contrast imaging is not yet well understood.

In the present chapter, the magnetic deterioration due to laser cutting two grades of NOES laminations is studied. Further, microstructure, crystallographic texture and magnetic domain analysis is done near the cut edge to understand the reason of magnetic property deterioration. SEM and nanoindentation is performed for microstructural analysis and mechanical property determination near the cut edge, respectively. For magnetic measurements, a standard vertical double yoke single sheet tester is used.

7.2 Experimental

7.2.1 Materials

Non-oriented electrical steel samples, 35WW300 and B35AV1900, were used in the present study. These samples were used in the as-received state with dimensions of 300 mm x 30 mm x 0.35 mm and also cut specimens. Specimens were cut along the longitudinal direction (rolling direction) into two pieces (laser 1), each with dimensions of 300 mm x 15 mm x 0.35 mm and also into three pieces (laser 2) each with dimensions of 300 mm x 10 mm x 0.35 mm as shown in Fig. 7.1.

The laser cutting was performed by “Metal CN” company using a standard high-speed Amada FO 3015 CO_2 laser cutting equipment. The focused laser beam was directed at the material resulting in melting of the material and N_2 was used as an assist gas.

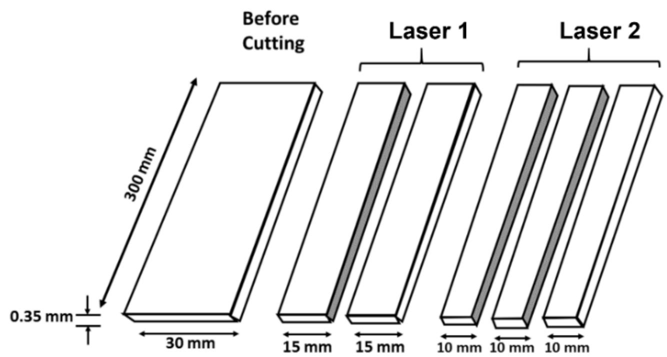

Fig. 7.1 The schematic of samples before and after laser cutting.

7.2.2 Magnetic measurements

A commercial single sheet tester (SST) was used for testing the magnetic properties of the laminations. First, measurements were executed on samples before cutting. Later, two piece and three piece cut samples were tested. To avoid the influence of geometrical shape on the magnetic properties, the cut pieces were taped together and placed into the testing device and measured simultaneously like a sample with a width of 30 mm. Core loss was evaluated for a range of frequency starting from 3 Hz to 1000 Hz, under sinusoidal waveform, and induction levels from 0.1 to 1.5 T. The main feature of the standard measurement of the magnetic properties is the waveform control of the secondary voltage. The form factor (FF) was considered as a measure for the purity of the sinusoidal flux density waveform, which indicates the accuracy of the measurements. The smaller the form factor (ideally 1), the more accurate the measurements. Fig. 7.2 shows the value of form factor as a function of peak flux density which is almost 1.11 from 0.1 T to 1.0 T for all the excitation frequencies. It shows slight variation beyond 1.0 T but the error is below 1 % which means the measurements are reliable for all the flux density levels and frequencies according to the standard IEC 404-3 [75].

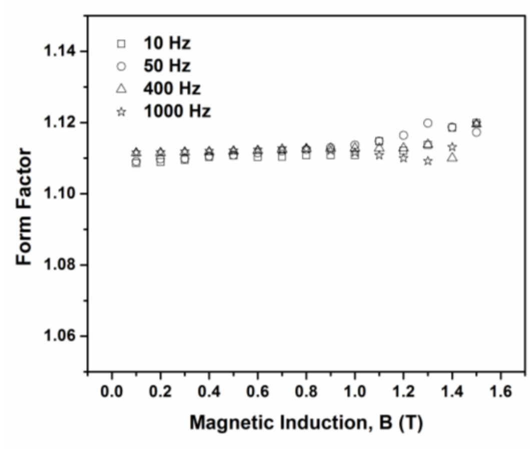

Fig. 7.2 Form factor versus B plot for various frequencies.

7.2.3 Material Characterization

The steel samples were prepared for microstructural observation and nanoindentation by polishing. First, the sample was cold mounted in an epoxy resin (conductive) and grinding was done using SiC grit papers 600, 800 and 1200. Then the cloth polishing was performed using 3 μm and 1 μm oil-based diamond suspension followed by vibratory polishing using 0.05 μm colloidal silica suspension for 20 hours.

Nanoindentation measurements were carried out at room temperature using Hysitron Ubi Indenter. The tests were conducted with a calibrated Berkovich diamond indenter tip. The hardness of steel specimens were determined using a standard Oliver and Pharr analysis [107]. Loading and unloading each lasted 5 s with a maximum force of 5000 μN and the hold period at maximum force was 2 s. Indentation was performed in a row starting from the laser cut edge of the sample towards the center with a spacing of ~30 μm between the indents.

Microstructural characterization was done using Hitachi SU3500 attached with EBSD, Hitachi SU8000 and Hitachi F50 electron microscopes. The electron dispersive spectroscopy (EDS) was used for analysis of chemical composition near the cut edge using F50 microscope at an accelerating voltage of 20kV. The magnetic domains imaging was done using SU3500 microscope equipped with EBSD. For magnetic domain imaging, the surface of the sample was further improved by ion milling and chromium layer (20 nm) was also deposited on the sample to improve electron flow. The images were acquired with a 70^o sample tilt and an accelerating voltage of 30 kV to improve the magnetic contrast. To image the domains, BSE images were recorded by two bottom fore scattered diode (FSD) detectors attached with EBSD camera. The images were captured with a pixel density of 1024 × 768 at a 24-bit depth, with a pixel dwell time of 200 seconds per scan with an average of 3 scans for one image. EBSD maps were captured at the same settings near the cut edge. High magnification images were also captured by SU8000 microscope at an accelerating voltage of 30 kV.

7.3 Results

7.3.1 Magnetic measurements

7.3.1.1 Hysteresis loops

The typical hysteresis loops of B35AV1900 and 35WW300 steel laminations before and after laser cutting are shown in Fig. 7.3. The laser cutting process deteriorates the magnetic properties which causes the flattening of the hysteresis loops. There is a decrease of remanent magnetic flux, B_r, and increase of coercive field strength, H_c, due to laser cutting, which indicates the presence of residual stresses induced due to cutting [11]. In case of B35AV1900 steel grade, the shape of the hysteresis curve changes significantly than that of 35WW300 steel. This means the deterioration in B35AV1900 steel is higher due to cutting compared to 35WW300. Also, there is a significant increase of coercivity and reduction in remanence in laser cut B35AV1900 sample, which causes the shape of the hysteresis to change. Similar results were reported by Naumoski et al. [10] for laser cutting NOES lamination.

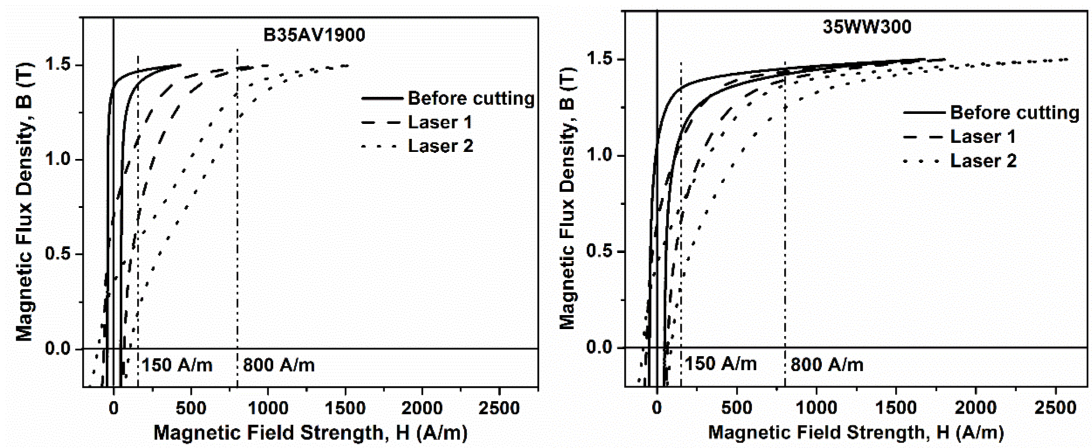

Fig. 7.3 The hysteresis loops of B35AV1900 and 35WW300 steel samples before and after laser cutting at 50 Hz and 1.5 T.

7.3.1.2 Permeability curves

Permeability is an important magnetic property to consider while designing the motor cores because it gives the ease with which the material can be magnetized. The high permeability material used as a core inside the motor concentrates the magnetic flux lines inside the motor core resulting in a better magnetic field and consequently, better motor performance. Permeability curves are used as an important input data for software packages because it is a measure of the material quality. A typical magnetic permeability curve plotted as a function of magnetic flux density increases initially with magnetic flux density, reaches a peak value at around 0.5 – 0.8 T and then decreases again as shown in Fig. 7.4. The reason for this can be explained by domain wall movement and domain wall rotation during magnetization [3]. At lower flux densities, the magnetization of steel is due to domain wall movement, whereas at higher flux densities, it is due to domain rotation which is comparatively hard than the domain wall movement. Laser cutting had a significant effect on the permeability of the steel lamination as shown in Fig. 7.4. The percentage decrease in permeability for laser 1 sample is 57 % and 72 % for laser 2 B35AV1900 steel, whereas it is 8 % for laser 1 and 35 % for laser 2 35WW300 steel at 1.5 T and 50 Hz frequency. The maximum change in permeability due to laser cutting is observed at 1 T for B35AV1900 and 0.6 T for 35WW300 steel. The drop in permeability due to laser cutting indicates that the residual stresses are induced in the material, which restricts the motion of the domain walls during magnetization [6].

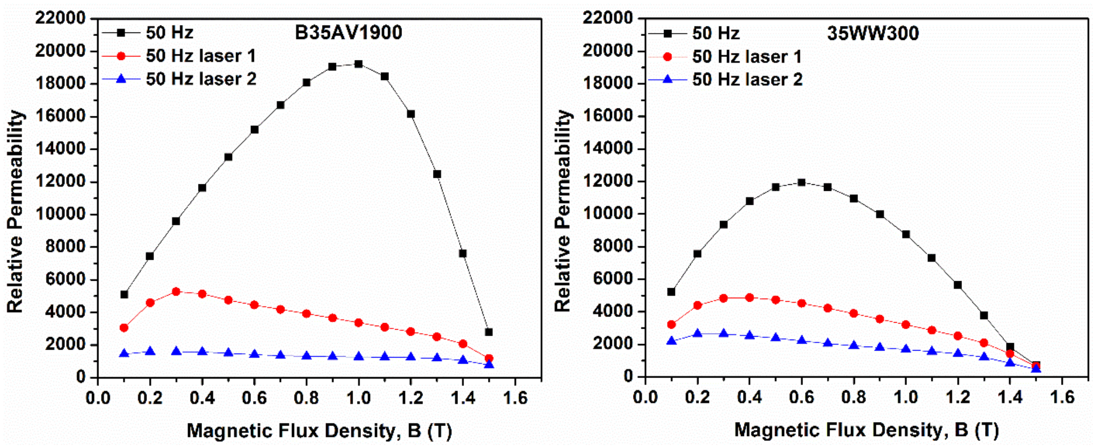

Fig. 7.4 The relative permeability of 35WW300 steel before and after laser cutting at 50 Hz frequency.

7.3.1.3 Core losses at different frequencies

The core loss of B35AV1900 and 35WW300 steel laminations at various frequencies is shown in Fig. 7.5 and Fig. 7.6, respectively. The core loss increases significantly due to laser cutting for both the grades of steel with the percentage increase in B35AV1900 higher than in 35WW300 steel. The percent increase in core loss in laser 1 sample is 56 % and 83% in laser 2 for B35AV1900 at 1.5 T at 50 Hz whereas for 35WW300, it is 22 % in laser 1 and 53 % in laser 2. This means that the increase in core loss due to laser cutting depends on the on the type of steel lamination and amount of cut volume in a lamination.

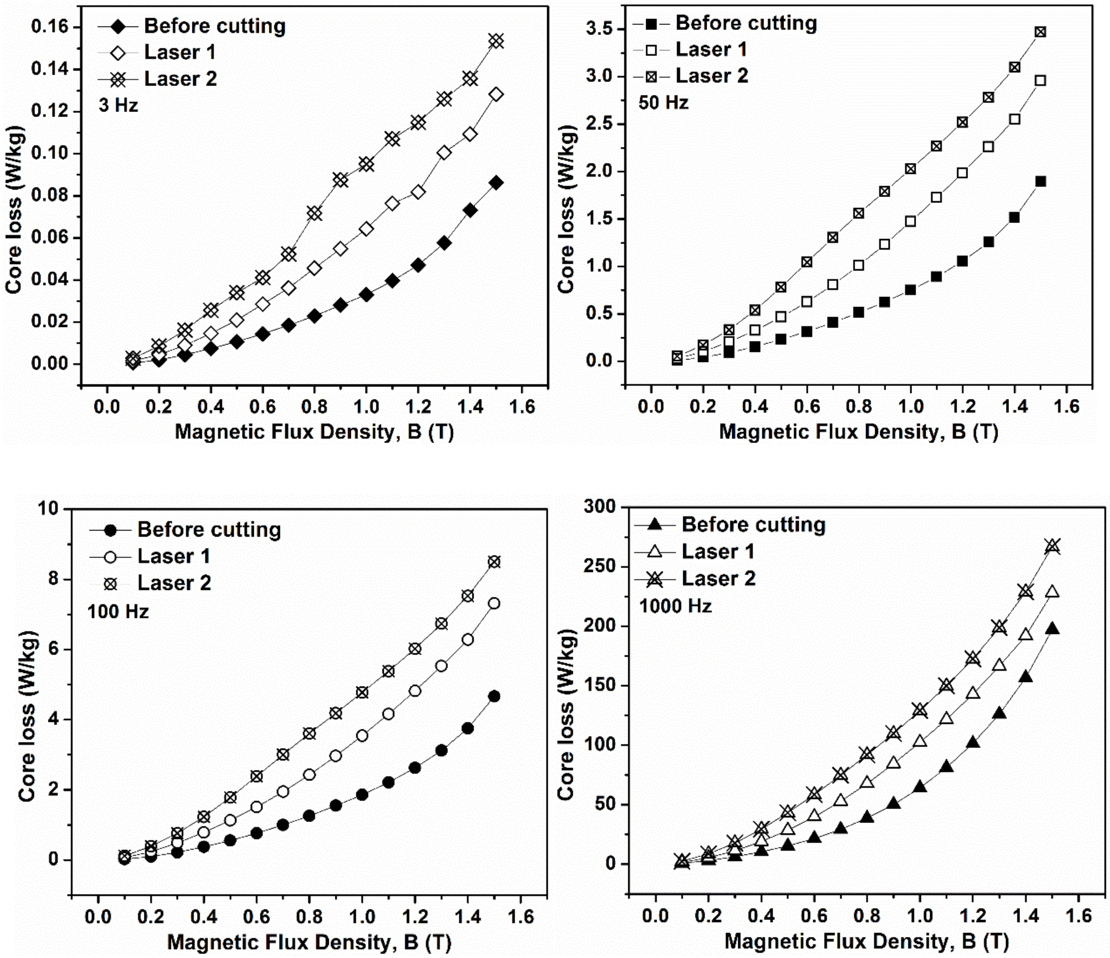

Fig. 7.5 The core loss as a function of maximum magnetic flux density of B35AV1900 steel at various frequencies.

The difference in core loss between uncut and laser cut samples increase with increase in magnetic flux density and it is maximum at 1.5 T. The frequency at which the measurements were taken also affects the core loss increase due to laser cutting. The magnitude of change in core loss due to laser cutting increases with increase in frequency.

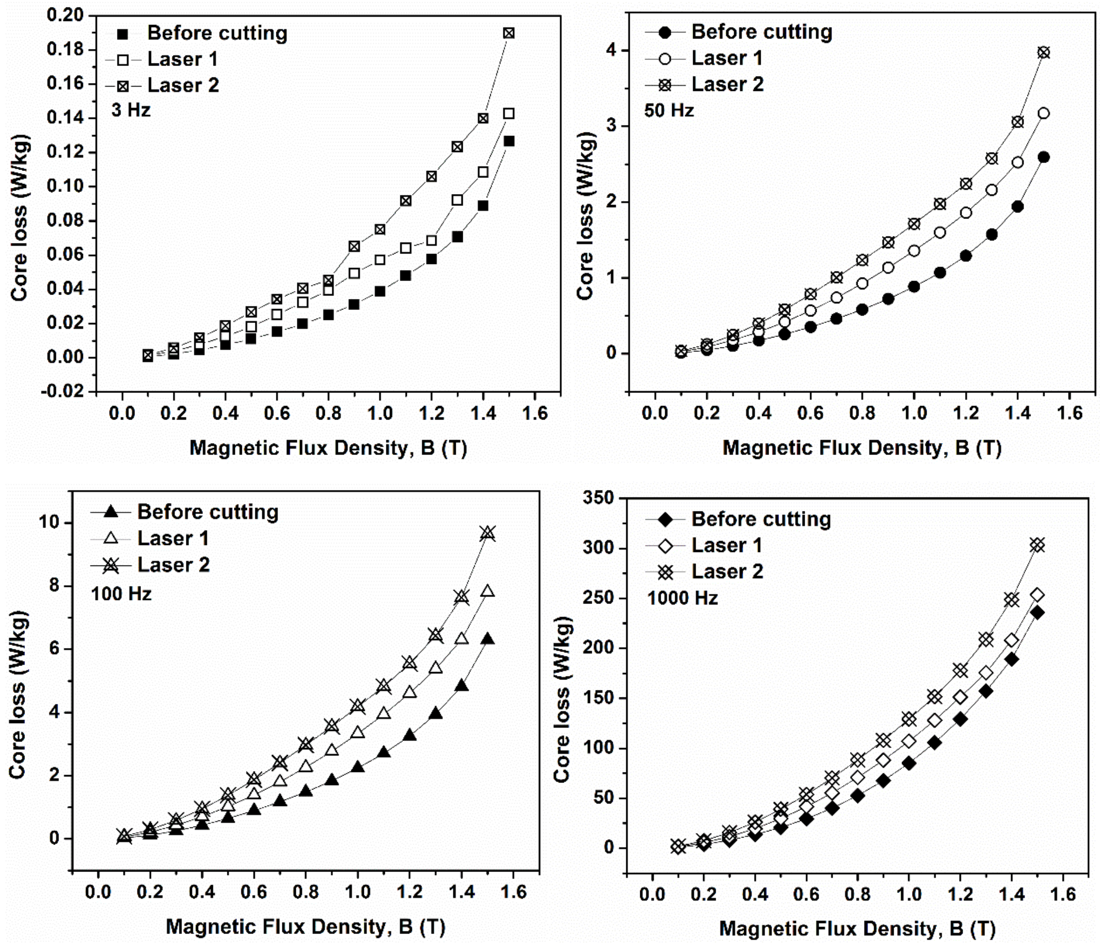

Fig. 7.6 The core loss as a function of maximum magnetic flux density of 35WW300 steel at various frequencies.

7.3.2 Microstructural characterization and Nanoindentation

7.3.2.1 Hardness profiles from nanoindentation

Nanoindentation measurements were performed to determine the point-to-point changes in mechanical properties. The hardness profiles of B35AV1900 and 35WW300 steel samples is shown in Fig. 7.7. The hardness was constant throughout the sample with no change due to laser cutting for both the grades. Therefore, laser cutting exerts no mechainical hardening near the edge of the material and no affected zone can be determined from hardness measurements.

Hofmann et al. [53] also reported that there is no mechanical hardening due to laser cutting from microhardness measurements.

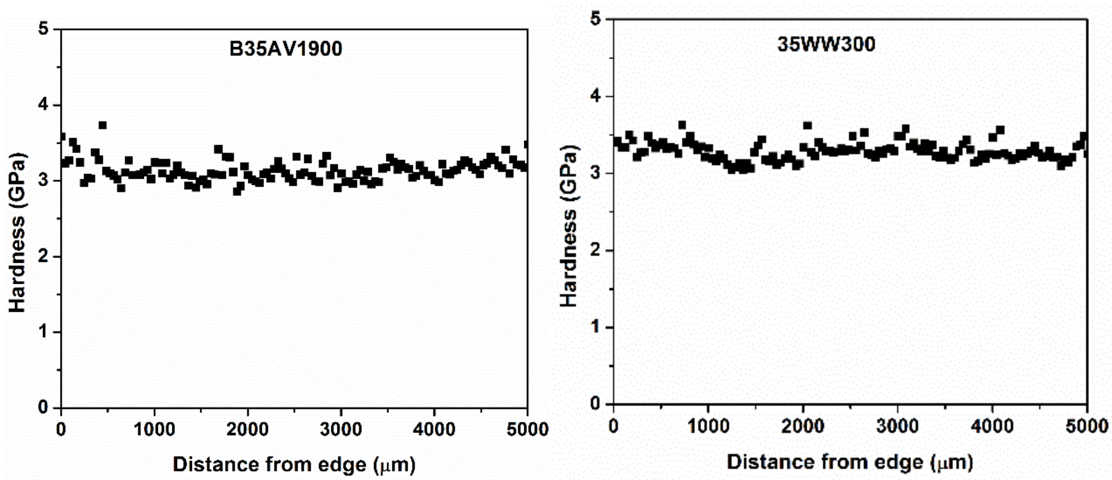

Fig. 7.7 The hardness plotted as a function of distance from the laser cut edge for B35AV1900 and 35WW300 samples.

7.3.2.2 Microstructure

After measurement of mechanical properties near the edge, the next parameter which could possibly explain the magnetic deterioration due to laser cutting was microstructure. The average grain size of B35AV1900 and 35WW300 was found to be 106 ± 13 μm and 130 ± 10 μm, respectively. Back scattered electron (BSE) images were analysed to find out the damage induced by laser cutting. The back scattered electron image of the samples is shown in Fig. 7.8 where no change in microstructure due to cutting is observed. There is no visible heat affected zone in these samples and not any phase transformations were observed near the edge due to heating. The reason for this is the high silicon percentage which stabilizes the ferrite phase and avoids the transformation at high temperature. In low silicon steels (< 0.5 wt. %), the laser cutting process results in the formation of bainitic phase and a clear heat affected zone [63]. Also, there is no change in grain size (Fig. 7.8) near the edge due to laser cutting, which can be explained by the severity of the thermal cycle in which time is too short to allow grain growth. Further, a contrast change is observed at certain points, which are marked by dotted circles near the edge for both the grades, with respect to the normal electron channelling contrast in the region away from the cut edge. These contrast effects are produced by the residual stress induced due to thermal fluctuations during cutting. This means that there is no continuous damaged area near the edge but there are regions with residual stress concentrations near the edge. The area up to which these stress concentration points are observed extends upto few hundred μm from the cut edge for both the grades. These results confirm the presence of residual stresses induced due to cutting and correlate with the magnetic deterioration results explained in the previous sections. However, the material modification and the area of the affected region due to cutting is still not quantified completely. The other reasons, which can cause the deterioration of magnetic properties, can be oxygen contamination and/or long-range residual stresses.

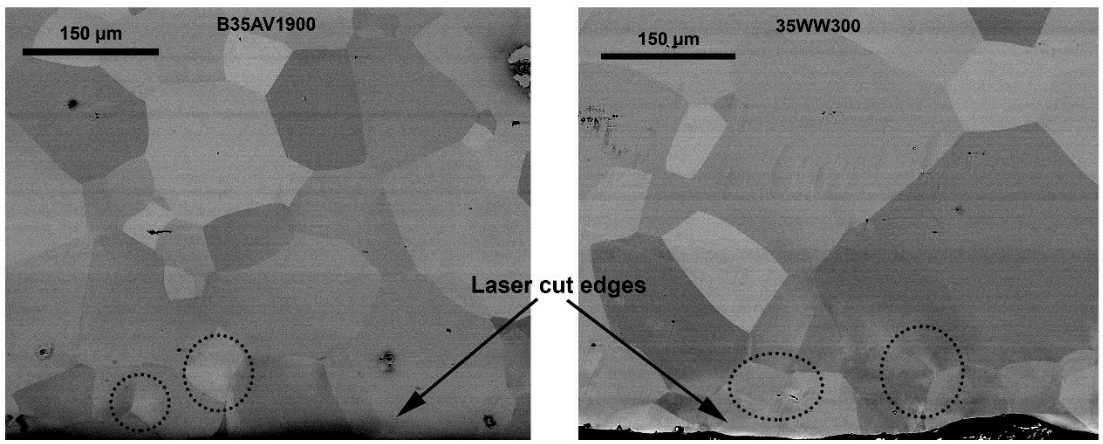

Fig. 7.8 The back scattered electron image of B35AV1900 and 35WW300 laser cut sample.

7.3.2.3 Chemical analysis

The elemental analysis was performed on the laminations to see the effect of laser cutting on the composition near the edge. The electron dispersive spectroscopy (EDS) analysis for B35AV1900 and 35WW300 grades near the cut edge and in the interior of the sample is shown in Fig. 7.9 and Fig. 7.10. There are only two elements detected by EDS which are Fe and Si that corresponds to the actual composition of these non-oriented electrical steel grades. There was no indication of oxide formation or any change in composition due to thermal effects of laser cutting. The elements which were present in the steel were Fe and Si with the weight percent Si equal to 3 %. One more peak was observed near 1.4 kV (Al) which was very small, thus, small amount of this element is also present.

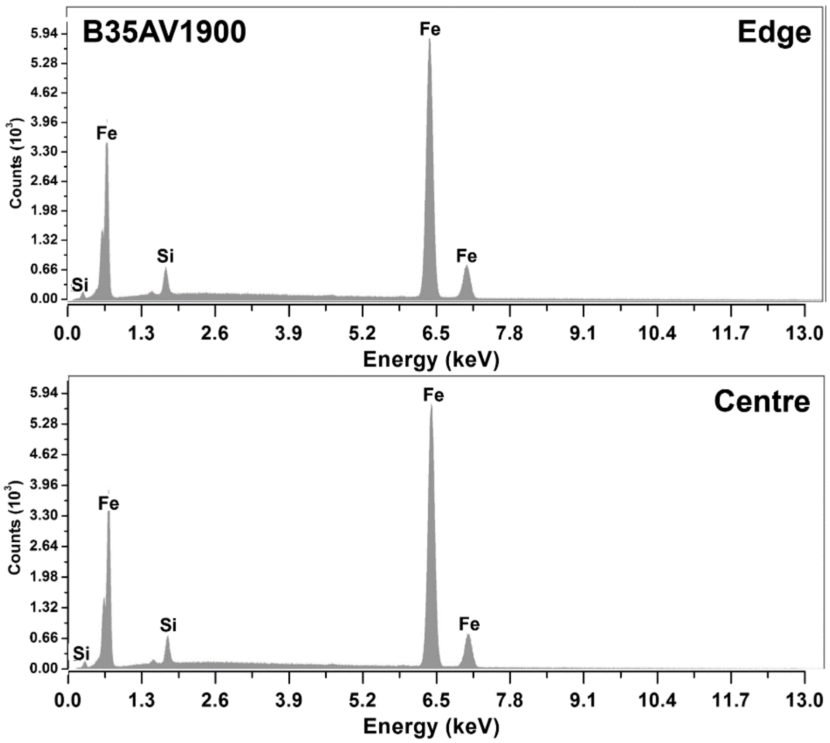

B35AV1900	Edge	Centre
	Wt.%	
Si	2.86	2.84
Fe	97.14	97.16

Fig. 7.9 The EDS analysis of B35AV1900 laser cut laminations near the edge and at the centre.

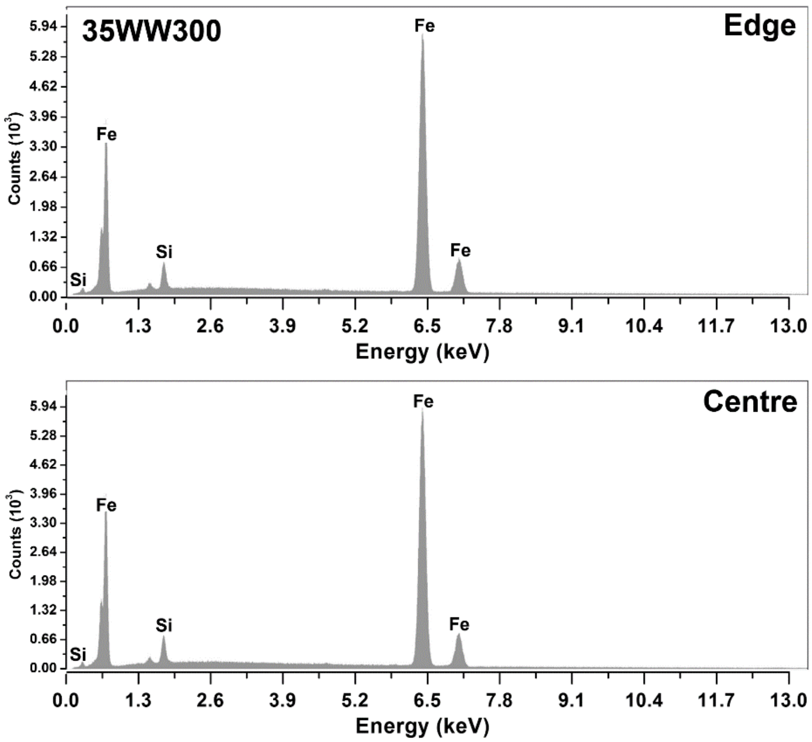

35WW300	Edge	Centre
	Wt.%	
Si	2.83	2.87
Fe	97.17	97.13

Fig. 7.10 The EDS analysis of 35WW300 laser cut laminations near the edge and at the centre.

The results obtained from microstructural analysis, hardness measurement and chemical composition determination indicated that there is no change in grain size, hardness and composition near the edge. However, there are other factors which can be responsible for the changes in magnetic properties such as thermal stresses [6], [63], crystallographic texture [6], [49] and magnetic domain structure [10], [53] near the edge. The magnetic domain analysis was done in one of the steel lamination (35WW300) to estimate the area affected by cutting. Since the domain structure is affected by the residual stress induced by cutting [53], the local magnetic domain analysis provides an idea about the extent of damage due to residual stress induced.

7.3.2.4 Magnetic domain imaging

Magnetic domain imaging was performed and the domain images are shown in Fig. 7.11. From these images, big slab like domains are visible away from the edge in unaffected area whereas the domain structure near the edge is modified due to cutting. Naumoski et al. [10] and

Hofmann et al. [53] reported similar results where the change in magnetic contrast was observed, near the laser cut edge, using Kerr magneto-optical microscope. A region of poor magnetic domain contrast (no contrast) was found near the laser cut edge compared to a good magnetic contrast in unaffected area in the NOES lamination. This area of poor contrast was termed as magnetically hardened zone and appeared possibly due to the residual stresses induced during cutting. The domain patterns in magnetically hardened zone were not visible from Kerr microscope because the resolution of Kerr microscope is low and hence, cannot image fine domains with the complicated structure [35]. In contrast, electron microscope has a high spatial resolution and can image fine domains. A study on magnetic domains was reported by Ding et al. [66] where modified fine domain structure due to coating stresses was observed using electron microscopy.

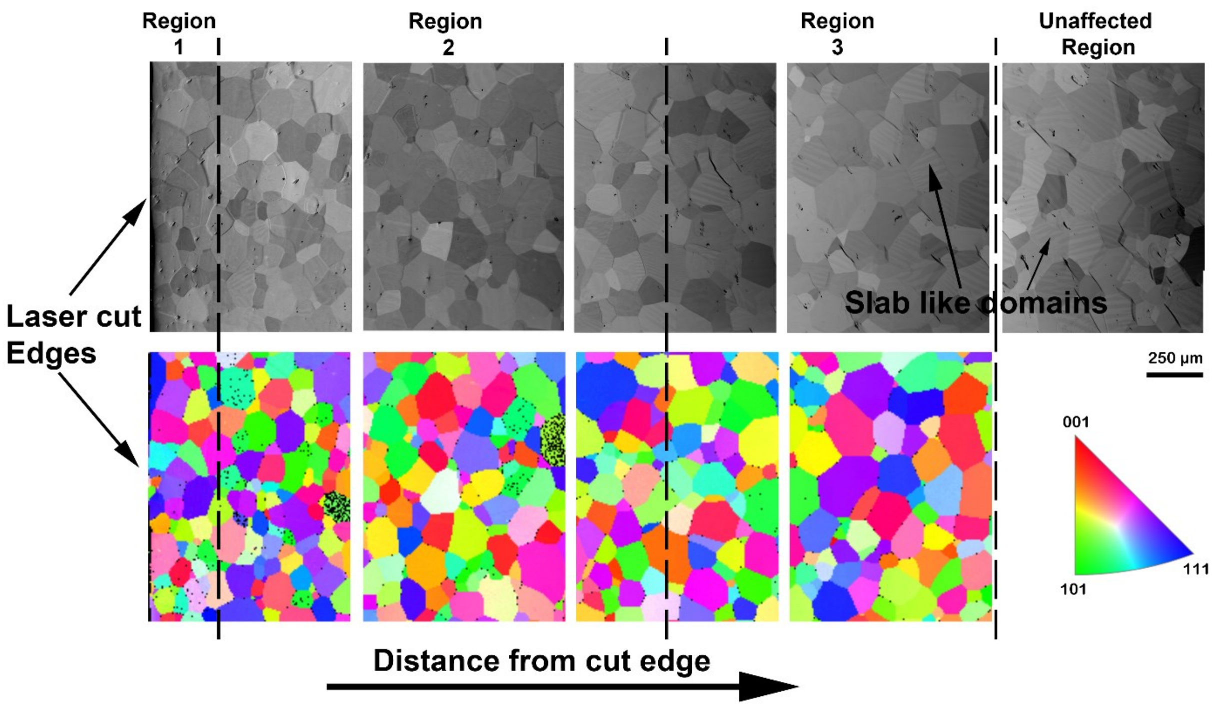

Fig. 7.11 Magnetic domain images and EBSD maps from laser cut edge towards the centre of 35WW300 lamination.

The high magnification images of the modified domain structure near the laser cut edge are shown in Fig. 7.12. A very fine striped domain structure is found in the grains close to the edge, compared to the large slab-like domains in the unaffected area. These striped domains are perpendicular to the cut edge, which indicates the presence of a stress component perpendicular to the cut edge [66]. This results in the magnetic property deterioration due to cutting.

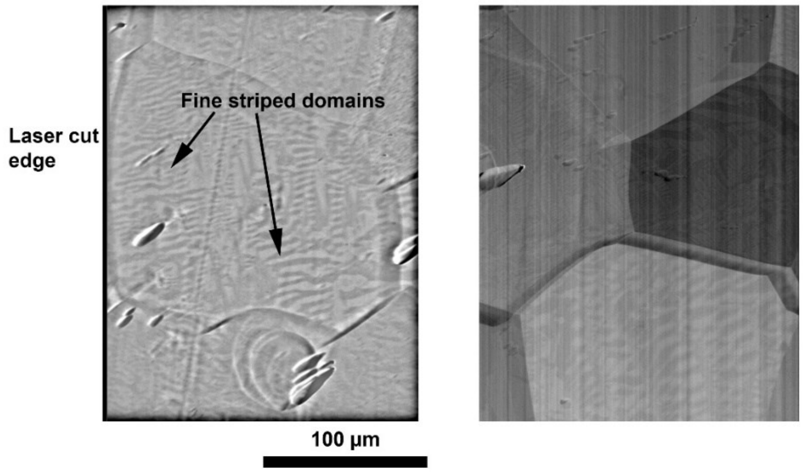

Fig. 7.12 Images of grains with modified domain structure near the edge due to laser cutting in 35WW300 steel. These grains are from region 1 of Fig. 7.11.

From Fig. 7.11 and Fig. 7.12, the striped domain structure was found in most of the grains of different orientations, with no grains having slab-like domain structure, in the region very close to the edge (region 1 of Fig. 7.11). This region also has maximum number of inclusions visible form the micrographs in Fig. 7.11. Beyond this region, the grains with slab-like domains started to appear and their number was increased with increase in the distance from the edge. These results of magnetic contrast imaging close to the edge correlated well with the residual stress observations from BSE image (Fig. 7.8), where a contrast due to residual stress was seen close to the edge. Further, a statistical analysis was done on the number of grains with the slab-like domains from the edge towards the centre of the sample as shown in Fig. 7.13. The affected area due to laser cutting can be divided in to different regions based on the degree of deterioration. The area close to the edge is more deteriorated with no slab-like domains (region 1 of Fig. 7.11 and Fig. 7.13). This region corresponds to the magnetically hardened zone found by Naumoski et al. [10] and Hofmann et al. [53]. After this region, there is low magnetic contrast up to ~3 mm having few grains with slab-like domains (region 2 of Fig. 7.11 and Fig. 7.13). This is followed by a region up to ~5.5 mm (region 3 of Fig. 7.11 and Fig. 7.13) where a mixture of grains with complex domain structure and slab-like domains are observed. Beyond this region, the domain structure seems unaffected. Hence, the affected region due to laser cutting can be divided into three sections: strongly hardened magnetic region (region 1), region with few slab domains (region 2) and a region consisting of a mixture of different domain patterns (region 3). This micromagnetic analysis from domain imaging explains well the results obtained from average magnetic measurements where the quality drop of 20-50 % was found in this grade (35WW300).

Besides the magnetic domain structure, the crystallographic texture is also modified due to laser cutting. The number of grains with near (111) orientation are more in the micrograph near the edge in Fig. 7.11 and it decreases with increasing distance from the edge. The (111) orientation is not a desirable orientation in terms of magnetic performance [14].

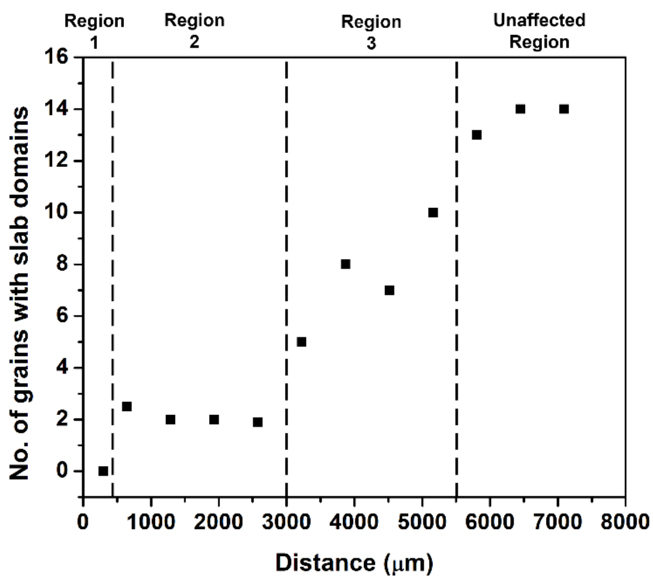

Fig. 7.13 The number of grains with slab domains vs distance from the laser cut edge in 35WW300 steel.

7.4 Discussion

The two grades selected for this study showed different magnetic deterioration after cutting. The increase in losses and reduction of permeability was observed to be higher in B35AV1900 compared to 35WW300 steel. The difference in the extent of deterioration due to cutting can be due to various factors such as initial grain size and composition. The percent increase in losses in B35AV1900 and 35WW300 grades at different frequencies is shown in Fig. 7.14. The percent increase in loss is higher in B35AV1900 steel compared to 35WW300 steel at all the frequencies and decreases with increase in frequency for both the grades.

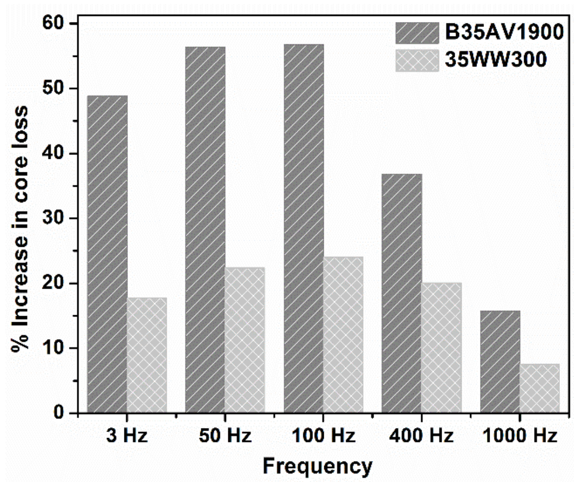

Fig. 7.14 Percent increase in core loss, for laser 1 sample, as a function of frequency, at 1.5 T, for B35AV1900 and 35WW300.

The laser cutting method lead to the degradation of magnetizability, especially at low flux densities, whereas the extent of degradation is reduced at higher flux densities as shown in Fig. 7.3. This means that laser cutting results in a steep increase in the field strength to reach equal flux density compared with the sample before cutting. The value of flux density was reduced by 23.9 %, for laser 1 B35AV1900 grade, at 150 A/m and 8.1 % at 800 A/m. For laser 1 35WW300 steel, the value of flux density was reduced by 20.3 % at 150 A/m and 1.37 % at 800 A/m. This means that the deterioration due to cutting decreases with increasing field strength. Similar results were observed by Naumoski et al. [10] and Hofmann et al. [53], where the magnetically hard zone was reduced with increase in field strength.

The observed changes in the magnetic behaviour can be correlated with its relevant material parameters. The material characteristics that have a strong influence on magnetic properties are grain size, inclusions, crystallographic texture and residual stress. These material characteristics determine the domain wall pinning and hence, affects the coercive field whereas crystallographic texture affects the domain rotation and hence, remanent magnetic flux [11]. The values of remanent magnetic flux and coercive field strengths can also be used to indicate the microscopic and semi macroscopic internal stresses induced due to cutting. These stresses are induced due to thermal gradient generated due to high temperatures employed during laser cutting. The stresses induced by laser cutting depends on the type of steel (particularly Si%) because the temperature gradient is affected by thermal conductivity of the steel [11]. The steel with high thermal conductivity will have higher residual stresses induced due to laser cutting.

7.4.1 Loss separation

The core loss analysis was made for the 35WW300 steel according to the loss separation concept, which considers that the total core loss is a combination of hysteresis loss and eddy current loss [14]. The following equation (Eq. 7.1) was used to calculate the hysteresis loss, where k_h is the hysteresis loss constant, B is the peak magnetic flux density and f is the frequency.

$$W_h = k_h \times B^2 \times f \qquad \dots (7.1)$$

The eddy current loss was calculated by subtracting hysteresis loss from the total core loss as (Eq. 7.2):

$$W_e = W - W_h \qquad \dots (7.2)$$

The effect of laser cutting on individual loss components is shown in Fig. 7.15. The hysteresis loss is affected more by laser cutting compared to eddy current losses. The increase in hysteresis loss due to laser cutting can be correlated with the magnetic domain analysis (Fig. 7.11, Fig. 7.12 and Fig. 7.13) that show modified domain patterns near the edge due to cutting.

The fine and distorted domain structure impedes the wall motion during magnetization resulting in increase of hysteresis loss. The residual stress component perpendicular to the cut edge and the increase in number of inclusions near the edge also increases hysteresis. In this way, the observed changes in hysteresis can be directly attributed to the microstructural changes induced by cutting. Eddy current losses are also increased by laser cutting but to a lesser extent than hysteresis.

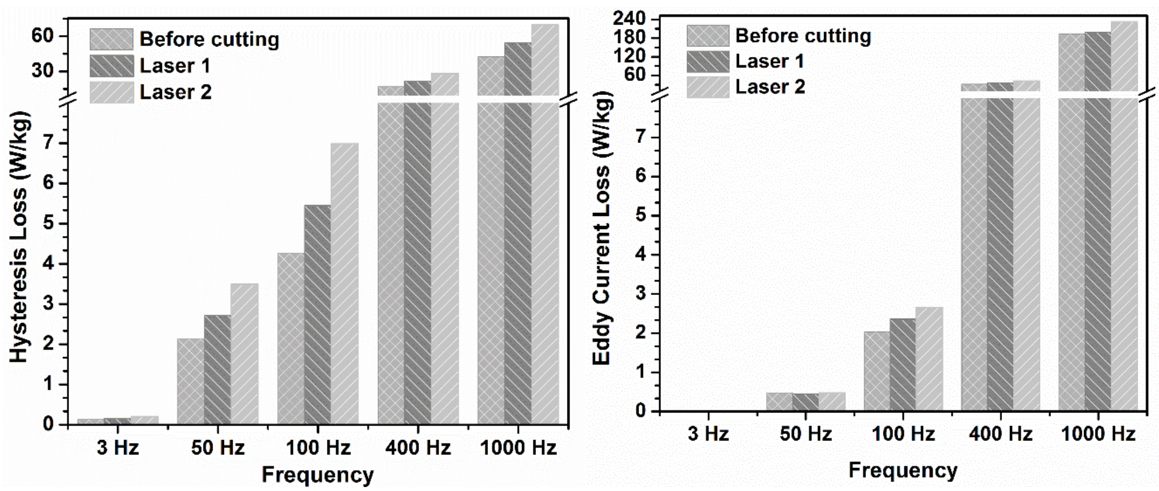

Fig. 7.15 The hysteresis loss and eddy current loss versus frequency before and after laser cutting 35WW300 at 1.5 T.

For better understanding the effect of cutting on the loss components, the percent increase in losses due to cutting are plotted as a function of flux density at 50 Hz as shown in Fig. 7.16. The percent hysteresis and eddy current losses decreases with increasing flux density and are minimum at 1.5 T. This is in good agreement with the results presented in Fig. 7.3, where the percent drop in flux due to cutting decreases with increase in field strength. This can be explained by change in magnetically hardened zone at higher flux densities or field strengths [10]. Also, the volume of cutting affects the losses and the percent increase in loss for laser 2 sample is almost double compared to laser 1 sample.

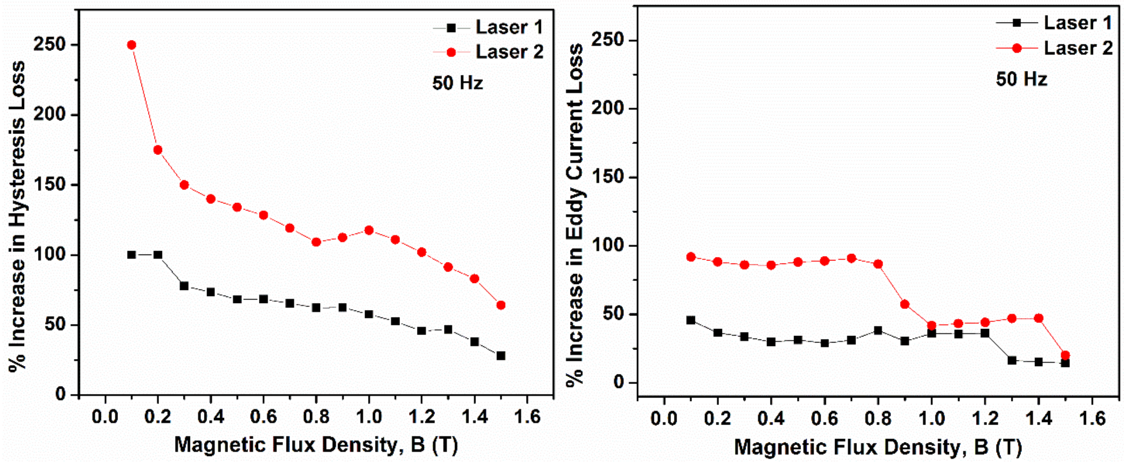

Fig. 7.16 The percent increase in hysteresis loss and eddy current loss as a function of maximum magnetic flux density of B35AV1900 at 50 Hz.

The percent increase in eddy current losses at different frequencies is shown in Fig. 7.17. The percent increase in eddy current loss shows a wider gap between laser 1 and laser 2 sample at lower flux densities but this gap decreases with increase in flux density. Morever, the percent loss decreases with increase in frequency.

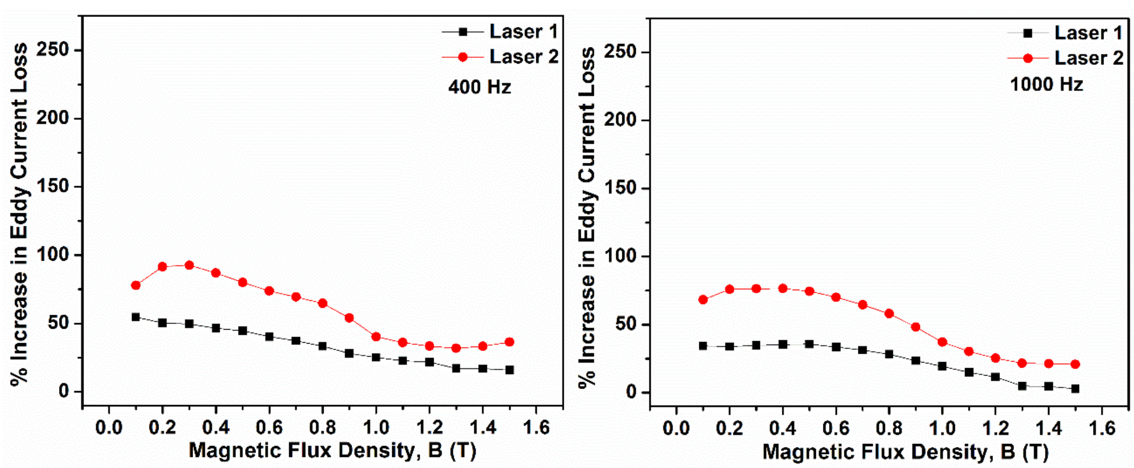

Fig. 7.17 The percent increase in eddy current loss as a function of maximum magnetic flux density of B35AV1900 at 400 Hz and 1000 Hz.

The contribution of hysteresis and eddy current loss components in increasing the total loss is shown in Fig. 7.18. As a result of significant deterioration, the hysteresis component represent important contribution to the total loss compared to eddy current component.

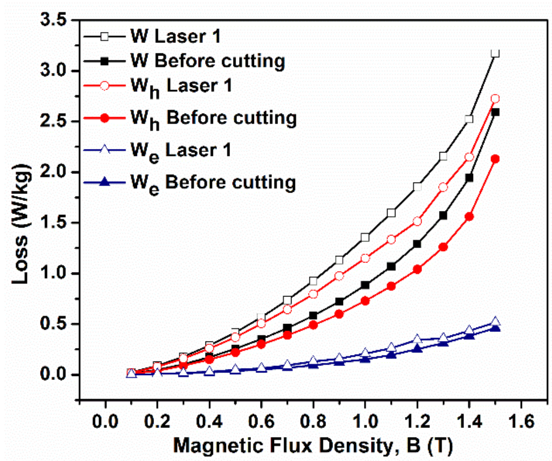

Fig. 7.18 The hysteresis loss, eddy current loss and total loss as a function of maximum magnetic flux density of 35WW300 Laser 1 sample at 50 Hz.

The calculation of core loss is important in the design process of electric machines. Despite the non-homogenous material modification near the laser cut edge, we derived and successfully related the loss components with the material modifications.

7.5 Conclusions

1. The core loss is increased due to laser cutting and also depends on the volume of cutting. This means that the laser 2 sample has higher losses than laser 1 sample.
2. Laser cutting also affects the permeability of the sample with the maximum change in permeability at around 0.6 T – 1.0 T.
3. The magnetic property degradation depends on the type of steel. The magnetic property deterioration is more for B35AV1900 sample compared to 35WW300 sample after laser cutting.

4. Laser cutting causes flattening of the hysteresis loops with increase in coercive field and decrease in remanent flux density.
5. The grain size, hardness and composition of steel sample is not changed by laser cutting. However, residual stress concentration points were observed from the BSE images.
6. There is magnetic domain modification near the cut edge, which is non-homogenous and can be divided into sections: severely deteriorated region (few hundred micrometers), region with poor contrast having very few slab-like domains and the region with mixed grains with fine complex domain structure and slab-like domains
7. Hysteresis loss is affected more by laser cutting than eddy current loss and is in good agreement with the magnetic domain modification near the edge.

8. Global Discussions

Motor laminations are manufactured by various cutting processes such as punching and laser cutting into a particular design followed by clamping the laminations together as a core by interlocking or welding. In Chapter 4, the microstructural changes which occurred during various stages of punching 35WW300 steel and its relationship with mechanical properties, was presented. It can help to better understand the changes in material and mechanical properties due to interlocking laminations, which consequently affects the magnetic performance of the core. It was reported by Nakayama et al. [113] that 3.6 vol% protuberance caused 18 % core loss increase, which can be a serious problem in small motors. During interlocking process, a dowel is formed in the lamination which is a protuberance formed by incomplete punching. This helps in clamping the laminations as a core by jointing the dowels together and therefore, the deterioration of magnetic properties due to interlocking can be caused by punching or stress induced due to jointing [114]. The stress due to incomplete punching a circular shaped protuberance was measured by nanoindentation in the present research. The factors responsible for hardness increase due to punching, such as residual stress and work hardening, were reported as shown in Fig. 4.11. The residual stress has less significant effect on the hardness of the sample whereas work hardening increases the hardness considerably. The Fig. 4.11 can be divided into two regions: elastic deformation region where the load was not high enough to induce plasticity and plastic deformation region where the material deformed plastically. The load which separated the two regions was in between 1100 N and 2000 N which can be referred as transition load. Therefore, while punching the material passes through stages from elastic zone to plastic zone via transition.

There is one more factor to consider while studying the hardness change due to punching which is change in grain size. It was confirmed by electron microscopy (Fig. 4.7, Fig. 4.8, Fig. 4.9 and Fig. 4.10) that no change in grain size occurred at lower loads (550 N and 1100 N) but at higher loads (4000 N), there were very small regions close to the punched edge where the highly-strained area was found (black region near the punched edge in Fig. 4.9). Due to poor EBSD contrast, this area was not clearly observed. The poor EBSD contrast was due to lack of output signal from that region which can be due to severe plastic deformation, which leads to the increase in dislocation density and misorientation angle. Severe plastic deformation can also lead to the formation of shear bands (or ultrafine grains), which can affect the hardness of the material [119]. This means that change in hardness at higher loads can be attributed to residual stress, work hardening and possibly grain refinement. However, from the EBSD image (Fig. 4.9) and BSE micrograph (Fig. 4.10) of the sample punched at 4000 N load, the regions with poor EBSD contrast are very small which makes the contribution of hardness change due to grain refinement negligible.

The changes in the hardness near the punched edge can be correlated with the microstructure of the steel and is strongly affected by work hardening, change in microstructure and residual stress induced. The hardness equation proposed by Frutos et al. [116] was used along with the microstructural analysis to separate the effect of each factor on the hardness change in the punched sample (Chapter 4 and Chapter 5). In the present discussion, the results from both the chapters are analysed together with more detailed Frutos analysis where the hardness change due to work hardening is calculated by the equation proposed by Frutos. The calculated values are then compared with the experimental values from Chapter 4 and Chapter 5.

8.1 Change in hardness due to work hardening in interlocking 35WW300 laminations (incomplete punching)

The total hardness (*H*) in the affected area can be divided into components: average hardness of the sample in unaffected area (H_0), hardness change due to work hardening (*H (W. H)*), hardness change due to grain refinement (*H (G. Ref)*) and hardness change due to residual stress (*H (Res. Stress)*) [116]. The hardness change due to work hardening, *H (W. H)*, was calculated by using the equation proposed by Frutos et al. [116] as shown in Eq. 8.1, where σ_y^* is the effective yield strength, ΔP is the load increase in the punched region, E_r is the reduced elastic modulus and h_{max} is the maximum depth of indentation.

$$\sigma_y^* = \left(\frac{\Delta P}{5.626.\, E_r \,.\, h_{max}^2}\right)^2 .\, E_r \qquad \text{... (8.1)}$$

The effective yield strength was used to calculate *H (W. H)* using Tabor's relation (Eq. 8.2) [132]:

$$H\,(W.H) = 3\,\sigma_y^* \qquad \text{... (8.2)}$$

The value of *H (W. H)* was calculated using 100 nm maximum depth using the hardness profiles of 2200 N, 3300 N and 4000 N sample from Fig. 4.6. The total hardness and the hardness increase due to work hardening vs distance is shown in Fig. 8.1. The hardness increase in the punched region for 2200 N sample was a combination of *H (W. H)* and *H (Res. Stress)* whereas in 3300 N sample, there were regions that were only affected by work hardening and some regions that were affected by both the work hardening and the residual stress. In 4000 N sample, the region which was mainly affected by work hardening was extended to approximately

100 μm. Therefore, the hardness change in affected region due to punching (interlocking samples) is due to a combination of *H (W. H)* and *H (Res. Stress)* (since *H (G. Ref)* is negligible in interlocking samples). The width of affected region due to incomplete punching at different loads in the NOES lamination and the calculated hardness values are given in Table 8.1. These values are in good agreement with the data analysed in Fig. 4.11, except for 4000 N.

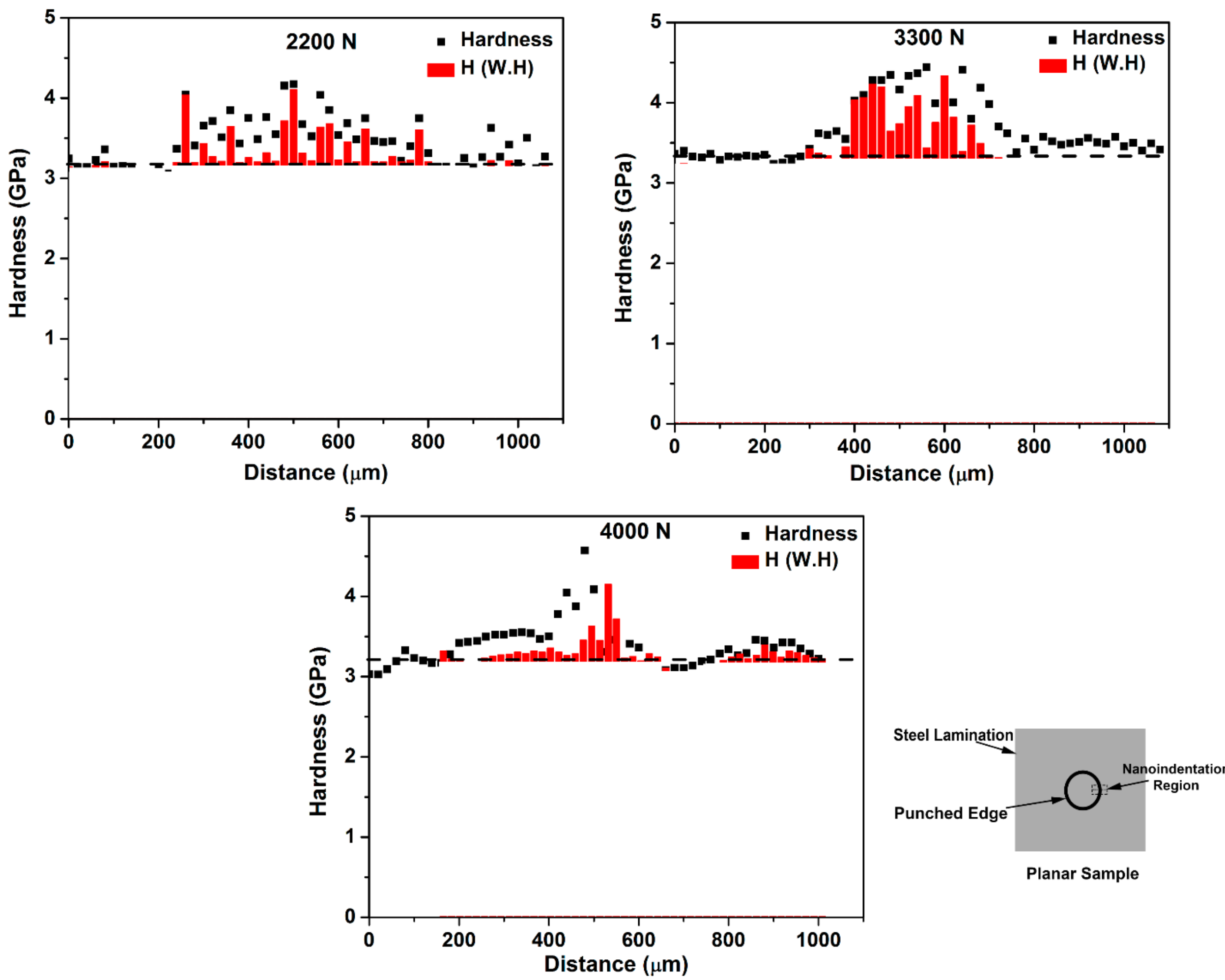

Fig. 8.1 The total hardness and hardness change due to work hardening as a function of distance in samples punched at 2200 N, 3300 N and 4000 N. The black dotted box in the schematic represents the area where measurements were performed.

Table 8.1 The width of affected region and hardness values of interlocking (incomplete punched) 35WW300 lamination.

Sample punched at different loads	Distance of damage (μm) - Nanoindentation	Peak hardness (GPa)	Hardness change in punched region (GPa)	H (W. H) from Frutos calculations	H (Res. Stress) = H – H_0 – H (W. H)
550 N	680	3.5	0.3	0	0.3
1100 N	600	3.45	0.25	0	0.25
1650 N	680	3.42	0.22	0	0.22
2200 N	600	4.15	0.95	0.37	0.58
3300 N	600	4.38	1.18	0.81	0.37
4000 N	600	4.64	1.44	0.3	1.14

8.2 Change in hardness in punched 35WW250 laminations

In Chapter 5, a detailed analysis of change in hardness due to work hardening, microstructural modification and residual stress was done in a punched non-oriented electrical steel lamination. The cross section of the punched lamination was analyzed and the microstructural heterogeneities were observed near the punched edge. The cross section was divided in to four regions namely, roll over, sheared, fracture and burr, based on the difference in the hardness profiles. Pop-in analysis was also performed on the nanoindentation data to determine the regions in the microstructure where the density of dislocations has increased due to punching deformation and ultrafine grains are formed. It was found that the regions of poor EBSD contrast in punched motor core tooth (Fig. 5.5) are higher (than those observed in incomplete punching, in Fig. 4.9, at 4000 N load) and those regions with poor contrast were further analysed and found to be shear bands with ultrafine grains. This confirms the hardness change was attributed to work hardening, residual stress and grain refinement in punched lamination. The hardness change due to work hardening was calculated by using equations 8.1 and 8.2 from hardness profiles in Fig. 5.12, Fig. 5.13, Fig. 5.14 and Fig. 5.15 for different sections of punched lamination. The values of *H (W. H)* for different sections are different and the contribution of hardness increase due to work hardening is maximum for fracture region among all the four regions as shown in Fig. 8.2. The different between the *H (W. H)* and the total hardness change gives an estimate of the hardness increase due to grain refinement and residual stress. The distance of damage estimated from nanoindentation, pop-in analysis and SEM micrographs for the punched sample is given in Table 8.2. Zero pop-in region represents the area with high dislocation density, which is due to the plastic deformation and therefore, hardness increase is mainly due to work hardening and grain refinement. Further, the distance of damage measured from SEM is higher than that observed with nanoindentation. This difference can be due to the presence of residual stress being so small that it cannot be measured by nanoindentation. The change in hardness for such a small value is difficult to interpret from nanoindentation because the variation in hardness up to ~ 0.1 GPa can also be due to grain orientation, grain boundaries, inclusions and other microstructural features, in addition to residual stresses if present. The hardness change due to various factors in punched 35WW250 lamination is given in Table 8.3 which is the modification of Table 5.1 and is in good agreement with those values.

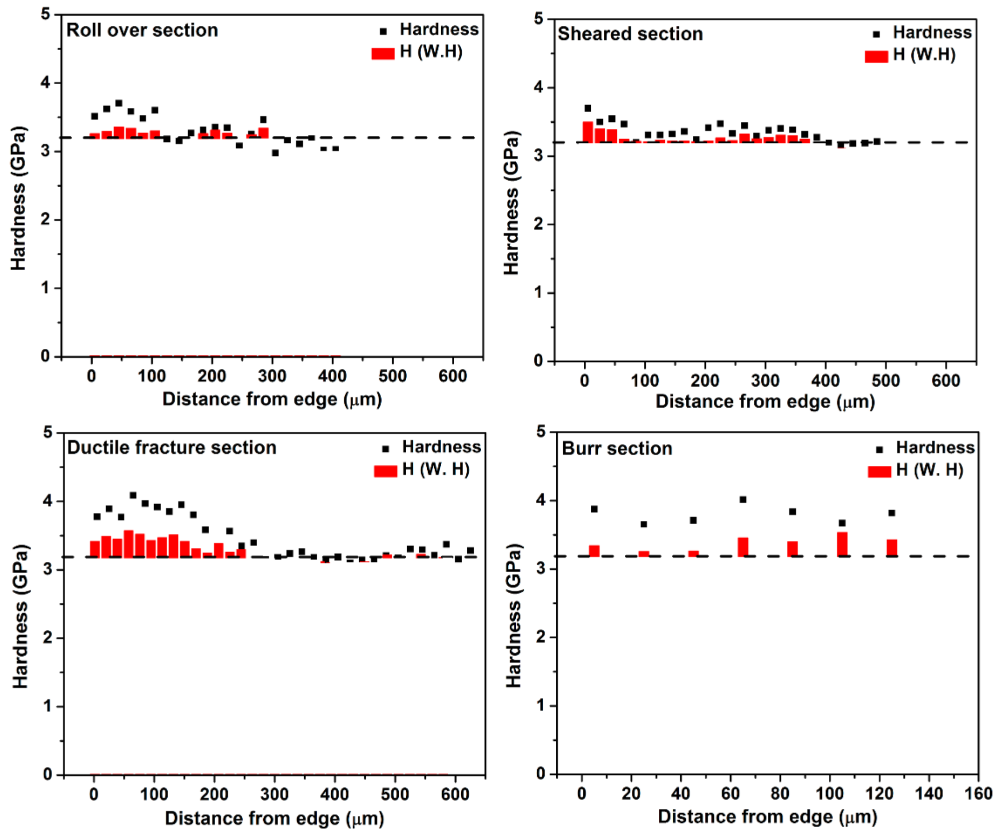

Fig. 8.2 The total hardness and hardness change due to work hardening as a function of distance in different sections of punched 35WW250 lamination.

Table 8.2 The width of affected region for various sections of cross section of punched 35WW250 steel.

	Distance of damage (µm)-Nanoindentation	**Zero pop-in distance (µm)**	**Distance of damage (µm)-SEM**
Roll over	100	50	180
Sheared	100	120	210
Fracture	300	210	280
Burr	Full area	Full area	Full area

Table 8.3 Hardness change in different sections of punched 35WW250 steel.

Section	Microstructural features	Maximum Hardness (GPa)- Nanoindentation	Possible reason for hardness increase (SEM)	H (W. H) – Frutos calculations (GPa)	H (G. Ref) (GPa)	H (Res. Stress) (GPa)
Roll over	Region with no grain size change but zero pop-in	3.68	Work hardening + Residual stress	0.107	0	0.42
	Region with no grain size change and non-zero pop-in	3.46	Residual stress	0.05	0	0.26
Sheared	Region with no change in grain size but zero pop-in value	3.6	Work hardening + Residual stress	0.2	0	0.25
Fracture	Ultrafine grains within the shear bands	4.54	Grain refinement +Work hardening + Residual stress	0.25	1.14	
	Region with no change in grain size and non-zero pop-in value	3.34	Residual stress	0.09	0	0.1
	Region where burr starts to form	4.41	Grain refinement +Work hardening + Residual stress	0.35	0.91	
Burr	Region with elongated grains	4.01	Grain refinement +Work hardening + Residual stress	0.2	0.66	
	Region within undeformed grain	3.69	Work hardening + Residual stress	0.23	0	0.31

The effect of mechanical cutting on the magnetic properties of NOES laminations was studied in Chapter 6. This chapter was focussed to study the effect of mechanical cutting on microstructure and magnetic properties of two non-oriented electrical steel grades – 35WW300 and B35AV1900. The deterioration was higher in B35AV1900 than in 35WW300 (Fig. 6.7), which means the laminations with bigger grains are better in terms of magnetic properties deterioration due to cutting. The shear cutting and punching cause the shearing of the lamination near the edge resulting in the separation of the material and therefore, induces similar microstructural changes. However, the area of damaged region near the edge can differ because shear cutting uses blade for cutting whereas punch is used in case of punching.

8.3 Comparison of microstructure and mechanical properties of shear cut, punched and laser cut samples

The microstructure of 35WW300 steel lamination which was shear cut, punched and laser cut is shown in Fig. 8.3. The microstructure of shear cut and punched samples are almost the same with the clear damaged zone near the edge due to plastic deformation and residual stress. However, the laser cut sample doesn't show a clear damaged region but there are some regions near the edge that show different contrast. This is due to the residual stress induced by laser cutting near the edge.

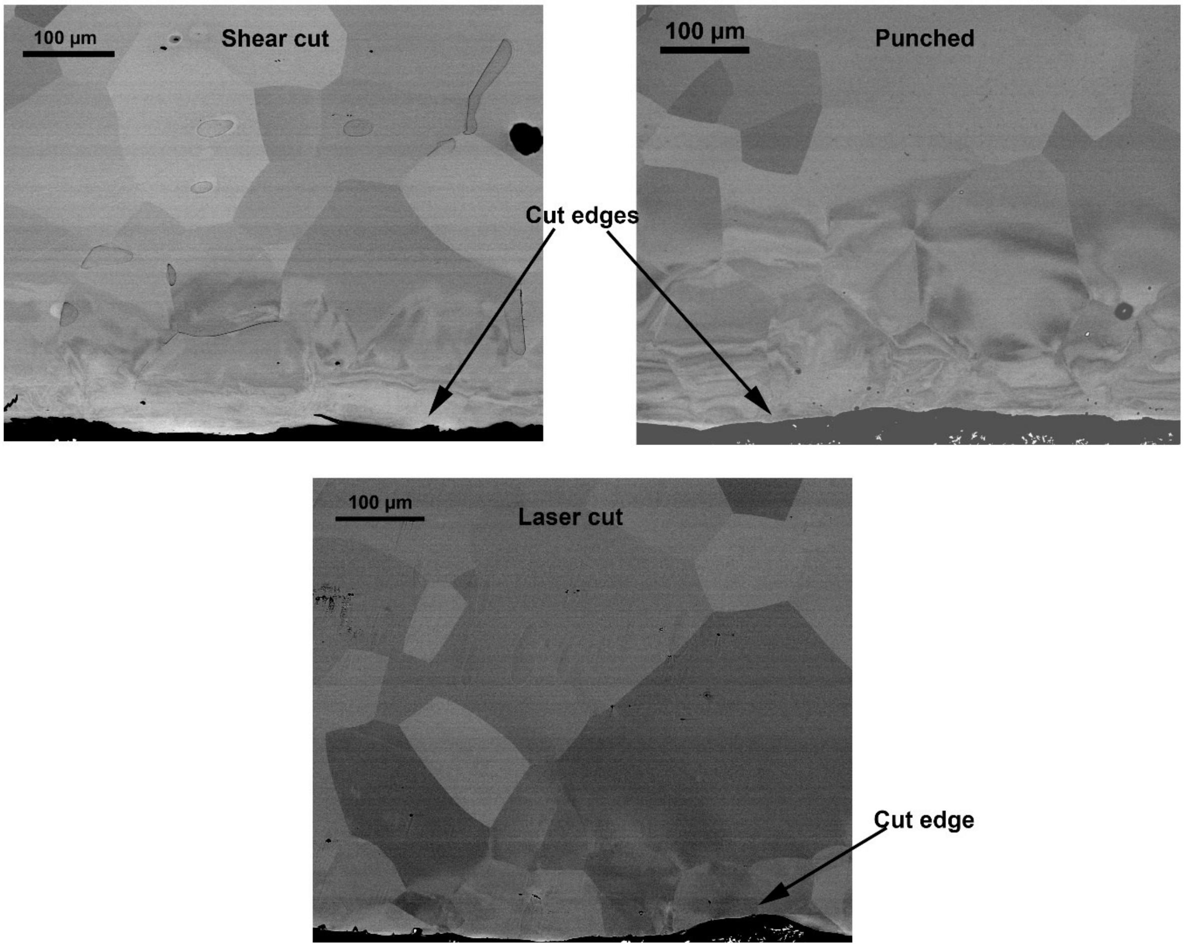

Fig. 8.3 The microstructure of shear cut, punched and laser cut 35WW300 steel lamination

The hardness profiles of shear cut, punched and laser cut samples is shown in Fig. 8.4 (obtained from Fig. 4.6, Fig. 6.4 and Fig. 7.7). The hardness increase near the edge due to punching is higher than that of shear cut sample and laser cutting has no effect on the hardness of the sample. The distance of damage measured from nanoindentation and SEM is given in Table 8.4.

Table 8.4 The width of affected region for shear cut, punched and laser cut 35WW300 steel.

	Distance of damage (μm)- Nanoindentation	**Distance of damage (μm)- SEM (BSE)**
Shear cut	140	170.8
Punched	250	281.7
Laser cut	0	No continuous damaged region

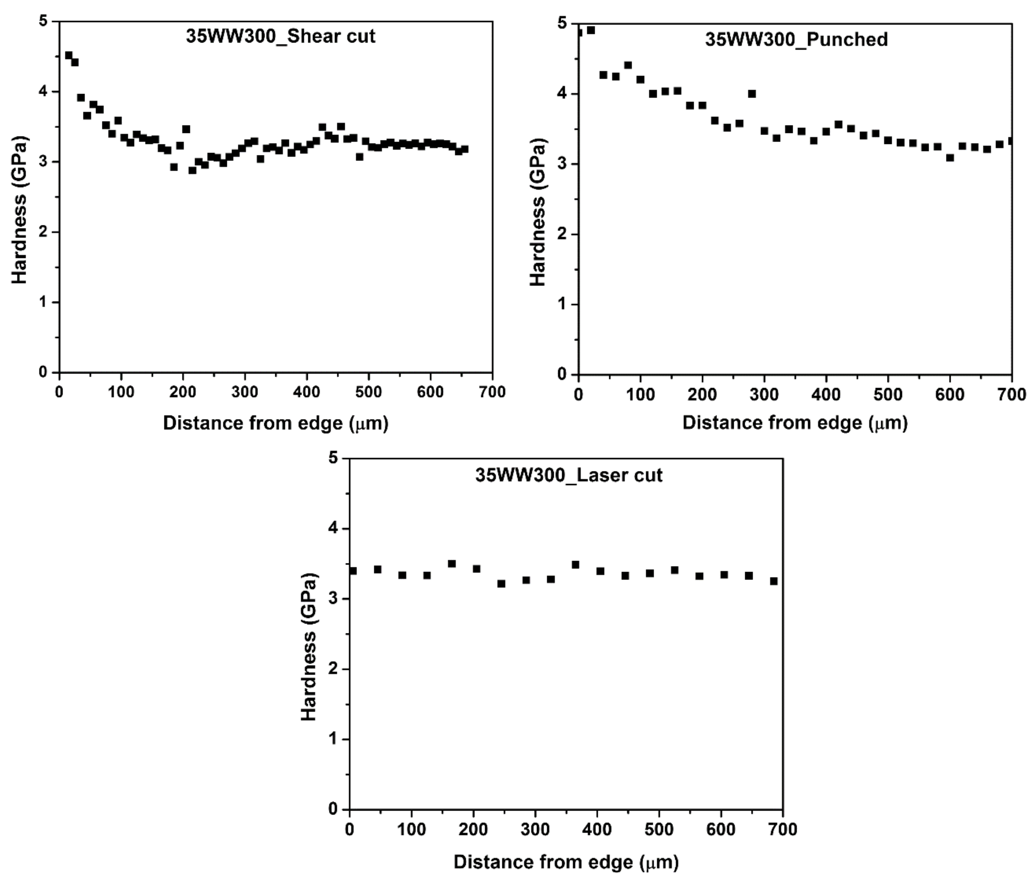

Fig. 8.4 The hardness profile of shear cut, punched and laser cut 35WW300 steel lamination.

The other type of cutting used for small batch production of motor cores is laser cutting which was studied in Chapter 7. In Chapter 7, the NOES lamination, 35WW300 and B35AV1900, were cut by laser cutting and their microstructure, mechanical and magnetic property characterization was done. The laser cutting deterioration is higher in B35AV1900 than in 35WW300 (Fig. 7.3) similar to the case of shear cutting (Fig. 6.5), which means bigger the grains, lesser the deterioration due to cutting. The comparisons between the shear cutting and laser cutting 35WW300 grade are made in the following section.

8.4 Comparison of magnetic properties of laser cut and shear cut samples

The magnetization curves of shear cut and laser cut 35WW300 laminations is shown in Fig. 8.5 (obtained from Fig. 6.5 and Fig. 7.3). The magnetic deterioration is higher for laser cut sample compared to shear cut sample and the extent of deterioration is different at different magnitudes of field strength. At lower field strength, the value of flux density is lowered by 3.6 % for shear 1 sample whereas it is lowered by 20.3 % for laser 1. At 800 A/m, the magnetic flux density is decreased by 1.36 % for shear 1 sample and 2 % for laser 1. Therefore, with increase in field strength, the deterioration due to cutting decreases and this is more significant in laser cut sample. The width of damaged zone in shear cut sample was 140 µm that was caused by plastic deformation, which is not easily recoverable. Hence, the magnetic deterioration due to shear cutting does not change much with field strength. In contrast, the laser cut sample showed modified magnetic domain structure near the edge extending up to 5.5 mm from the edge, which explains 20.3 % drop in flux at lower field strengths (Fig. 7.11). Naumoski et al. [10] reported that the magnetic contrast near the cut edge of non-oriented electrical steel changes with change in the magnitude of the magnetic field. At lower field values, poor magnetic domain contrast was observed near the laser cut edge using Kerr microscope, whereas, at higher field magnitude, the region of poor magnetic contrast was reduced. Thus, a significant change in magnetic deterioration due to laser cutting is observed at different field strengths, as shown in Fig. 8.5. This is further explained in Fig. 8.6, where percent change in losses is observed with change in flux density at 50 Hz. The percent change in loss due to shear cutting is almost independent of flux density, whereas it decreases with increasing flux density for laser cut samples. These results are in good agreement with the microstructural modifications in shear cut and laser cut samples as discussed above.

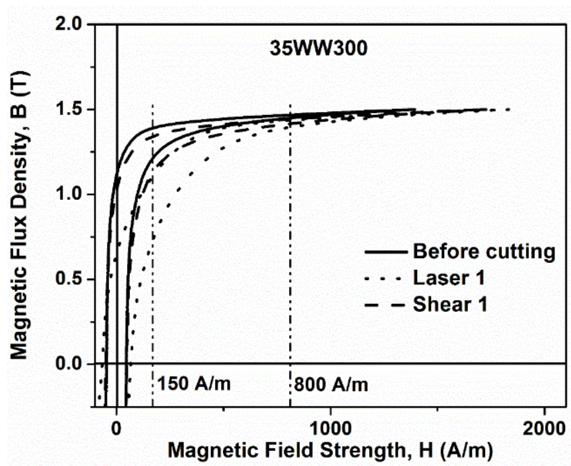

Fig. 8.5 The magnetization curves of shear cut and laser cut 35WW300 lamination.

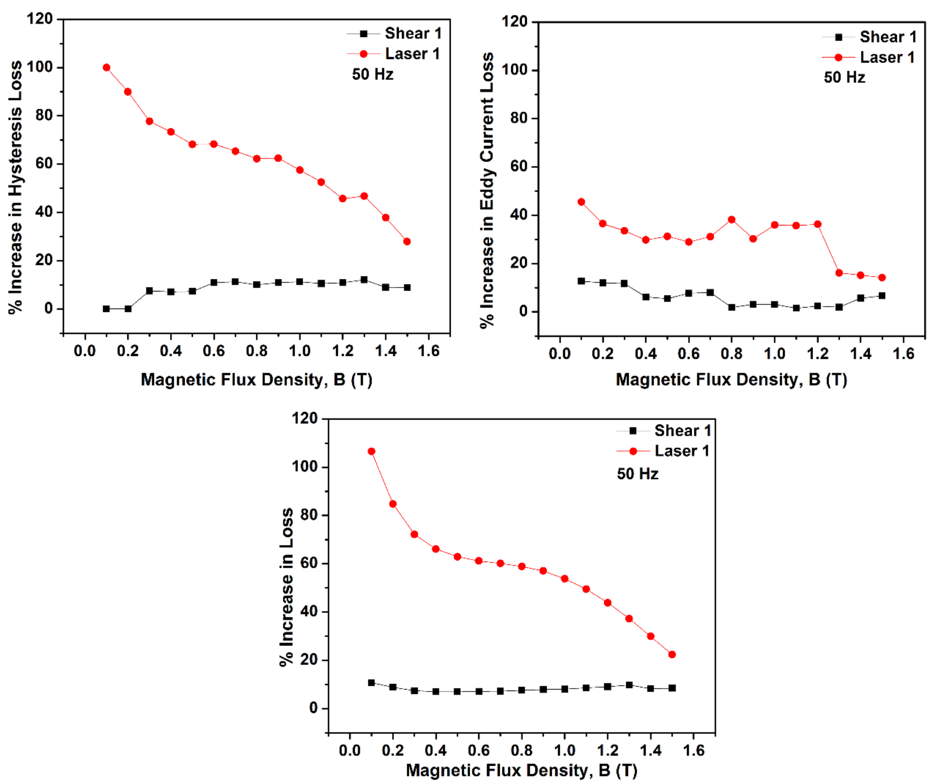

Fig. 8.6 The percent increase in hysteresis loss, eddy current loss and total loss as a function of maximum magnetic flux density of 35WW300 at 50 Hz for shear cut and laser cut samples.

The comparison of losses changed due to shear and laser cutting is shown in Fig. 8.7 and Fig. 8.8 (derived from Fig. 6.6 and Fig. 7.6). The effect of laser cutting on magnetic properties is more than that of shear cutting, as shown in Fig. 8.7. Also, both the cutting methods affect the hysteresis losses more than the eddy current losses at all frequencies upto 1000 Hz. At 3 Hz frequency, the total increase in loss in shear cut as well as laser cut samples is due to hysteresis loss component with no eddy current loss. Thus, cutting modifies the material near the edge which restricts the movement of magnetic domains during magnetization, resulting in increase in hysteresis losses. However, the material modification does not signifcantly affect the eddy current losses. The reason for less change in eddy current losses due to cutting is that the frequency is not high enough for the eddy currents to become dominant and increase the losses. Also, eddy currents depend on various other factors such as resistivity and skin depth, which can be affected by cutting. Hence, it is difficult to separate the effect of individual factors on eddy current loss change due to cutting and therefore, simulations can be done in future to quantify the effect. The change in individual loss components due to cutting at 50 Hz is shown in Fig. 8.8.

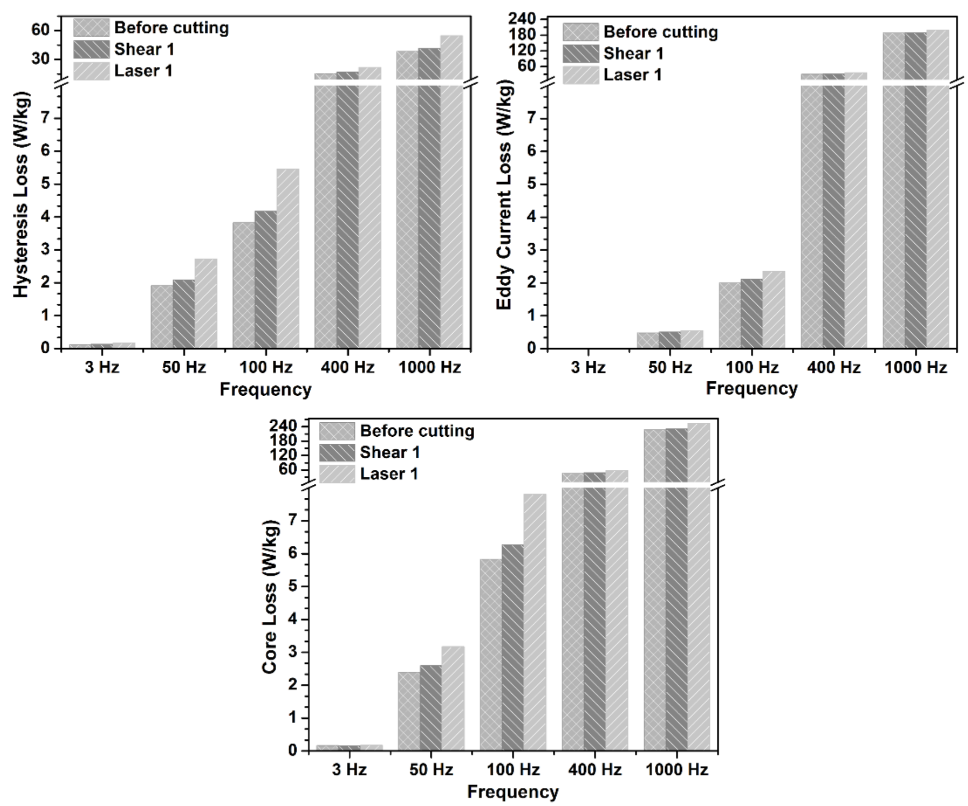

Fig. 8.7 The hysteresis loss, eddy current and total core loss versus frequency of 35WW300 sample before and after shear and laser cutting at 1.5 T.

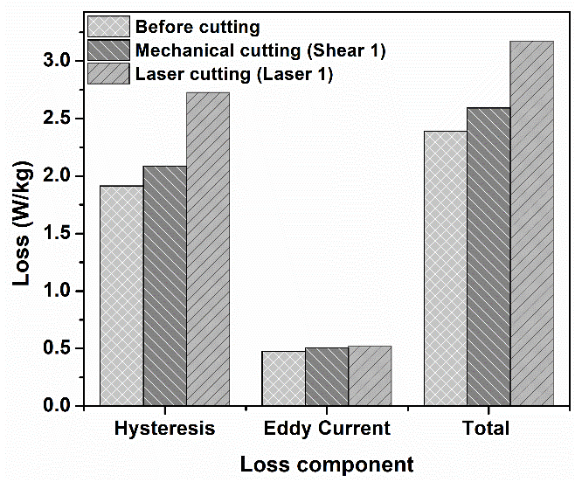

Fig. 8.8 The hysteresis loss, eddy current and total core loss of 35WW300 sample before and after shear and laser cutting at 1.5 T and 50 Hz.

8.5 Summary

The examined manufacturing methods, interlocking, punching, shear cutting and laser cutting, were analysed in greater depth and compared with one another in this chapter. All these methods lead to the modification of microstructure and material properties, which was demonstrated by SEM micrographs and nanoindentation. The mechanical cutting (punching and shear cutting) induces plastic deformation and residual stress near the edge, which consequently increases the hardness near the edge. The hardness change in punched sample was higher than the shear cut sample whereas no mechanically hardened area was found in laser cut sample. Also, the distance of damage for punched sample was 281 μm and 170 μm for shear cut sample, measured from SEM micrographs.

The hardness change near the punched sample was divided into hardness change due to work hardening, grain refinement and residual stress based on Frutos analysis along with the microstructural analysis. The damaged induced by interlocking (incomplete punching) was mainly due to work hardening and residual stress whereas in punched sample, a highly heterogenous microstructure was observed due to the formation of shear bands and elongated grains and the damage is higher.

The magnetic measurement results were analysed by magnetization curves and losses for the shear and laser cut samples. The laser cutting process deteriorates the magnetic properties to a greater extent than shear cutting process. Shear cutting induces plastic deformation, which results in the lattice distortions and increase in the number of defects. These defects act as hindrances to the movement of magnetic domains, therefore, losses are increased. Hence, there is a direct correlation between the magnetic property deterioration and microstructural modification. In laser cut samples, the magnetic deterioration was found to be higher than shear cutting because the deterioration is more global rather than local and was explained by the micromagnetic analysis near the cut edge.

9. Synopsis

9.1 Summary and Conclusions

The deterioration of magnetic properties is measured in terms of increase in losses and decrease in permeability. Less deterioration in magnetic properties of non-oriented electrical steel laminations, due to the manufacturing process, is necessary in order to maintain the performance of electric motor. First, the modification of microstructure and material properties due to manufacturing was investigated and then, it was related to magnetic properties. The interlocking dowel of spherical shape was produced by punching the steel lamination at a load lower than the actual punching load at which the material breaks into two pieces. Different interlocking samples were prepared at different loads starting with a load of 550 N. Formation of dowels induces residual stresses in the laminations at lower loads whereas plastic deformation (work hardening) was induced, in addition to residual stress, at higher loads (≥ 2200 N). The work hardening and the induced residual stress both deteriorates the magnetic properties but the extent of deterioration by work hardening is more than the residual stress. Hence, it is desirable to select a load which results in lesser damage of the material due to the formation of dowels by punching. This will help in reducing the core losses due to manufacturing of the motor core laminations.

The industrial punched sample was examined under electron microscope and the microstructural features which can deteriorate magnetic properties were analysed. The deformation structure formed due to punching was found to be heterogeneous and consisted of shear bands and ribbon grains. The ribbon grains were formed in more stable crystal orientations e.g {110} for Si-steel. Further, the punched edge was divided in to four sections based on the hardness profiles and microstructure. The sections were named as: roll over, sheared, fracture and burr. The increase in hardness for roll over section was small, which was attributed to the plastic strain and tensile residual stress. Sheared section was characterised by plastic strain and residual stress. Ductile fracture section showed an increasing trend of hardness initially reaching a peak and then decreasing. Burr section was characterised by plastic strain which was indicated by zero pop-in displacement in the entire section. The dislocation density increased due to work hardening and shear band formation can be the major cause of deterioration of magnetic properties. This is probably due to the dislocations acting as hindrances to the motion of domains, resulting in the increase of losses. Further, the distance of damage was maximum for the ductile fracture section among the other four sections, which means that magnetic property deterioration varies from one point to another within the damaged region. Hence, it is desirable to include these microstructural modifications in the loss calculations of the core of electric motors.

The mechanical cutting (shear cutting) led to an evident magnetic property deterioration such as increase of iron loss and decrease of permeability and these variations became more obvious with increasing cutting volume from shear 1 to shear 2. The loss increase due to shear cutting was ~20% for B35AV1900 steel and ~9% for 35WW300 steel, at 1.5 T and 50 Hz, which was well correlated with the damaged region for these two grades. The distance of damage for B35AV1900 steel was 170 µm from the edge whereas it was 140 µm for 35WW300 steel. Therefore, the distance up to which the material properties are modified by cutting is important to understand the extent of magnetic property deterioration.

The laser cutting deteriorates the magnetic properties more than mechanical cutting. However, it is difficult to estimate the damaged region from microstructural analysis or hardness measurements. Therefore, micromagnetic analysis was performed near the edge, along with the BSE imaging, to relate the magnetic deterioration due to cutting with microstructural changes. The magnetic domains near the cut edge were modified by residual stress induced by cutting and a non-homogenous damaged zone was observed, which extended up to ~5.5 mm from the edge. This damaged zone is very different from the one formed near the shear cut edge. The damaged region near the shear cut edge is highly deteriorated by plastic deformation and residual stresses and the deterioration of magnetic properties mainly occurs due to that area. In contrast, the damaged region of laser cut samples are divided into 3 sections: one with grains having only modified striped domains aligned perpendicular to the cut edge, extending up to a few hundred micrometers from the edge, second one with very few grains with slab domains and maximum striped domains extending up to 3 mm and the third one with the mixture of grains with slab like domains and striped domains (up to 5.5 mm). This means that the magnetic deterioration due to laser cutting is not only restricted to the area very close to the edge but is extended over a wide area, which explains the drastic increase of losses and reduction of permeability by laser cutting.

Loss separation calculations showed that the cutting affects the hysteresis losses more than the eddy current loss. This is because of pinning of domains by defects created by plastic deformation due to shear cutting and complex domains formed due to laser cutting. The deterioration due to cutting decreases with increase in field strength and this change is significant in laser cutting.

The calculation of core loss is an important task in the design process of the electric motors. Usually, the steel laminations database consists of information obtained by Epstein frame or SST based on the sample geometries without considering the effects of cutting. In case of machine designs that employ small geometries, the properties encountered in real applications are significantly worse than specified in the datasheet, especially when laser cutting is used. Under such conditions, a detailed study of material modifications which affects the magnetic properties and the region up to which it extends is required. The dependence of magnetic properties on the material parameters modified by cutting requires an appropriate database for the better design process.

9.2 Contributions to Original Knowledge

The present research will contribute to the understanding of different manufacturing methods used to design the motor core laminations. This research will help in relating the microstructural changes due to manufacturing with the mechanical and magnetic property modification. This understanding is important in terms of materials selection and optimization of manufacturing parameters to reduce the core losses. The main contributions of the present study are as follows:

- The detailed microstructural analysis, showing the formation of different microstructural features, across the thickness of the punched lamination and its relationship with the mechanical properties was first time done in the present thesis. This study can help to better understand the damage caused by punching and estimate its effect on the magnetic property deterioration.
- Studied the contribution of work hardening, residual stress and grain refinement in increasing the hardness near the edge of mechanically cut sample by relating microstructure and hardness measurements.
- Estimation of damaged region by various methods such as hardness measurements, pop-in analysis and SEM. Combination of these techniques showed a complementarity, which is useful for future studies.
- Measured the affected region in laser cut samples by magnetic domain analysis performed on the cut edge using electron microscopy. The magnetic domain imaging was observed along with the local texture and BSE micrographs to understand the material modification near the edge.
- Successfully related the microstructural and material modifications, due to shear and laser cutting, to the magnetic deterioration. This study is useful for incorporating the material parameters into the design of motor core laminations, to minimize losses.

9.3 Suggestions for future work

This thesis aimed to study the microstructural modifications and mechanical and magnetic property characterization for different manufacturing processes and tried to bridge the gap between the material and magnetic properties. However, there are few things which are yet to be understood and can be done in future are as follows:

- More detailed analysis on the magnetic domain contrast effects due to laser cutting and performing the similar analysis for shear cut samples.

- Study the effect of shape of interlocking dowels on the material and mechanical properties.
- Measurement of magnetic deterioration due to interlocking dowels in a NOES lamination and relating that with microstructure and mechanical properties.
- Repeating the similar study for more grades of steel to understand better the effect of grain size, texture and composition on the cutting deterioration.

Bibliography

[1] V. Petrus, “Switched Reluctance Motors for Electric Vehicle Propulsion: Comparative Numerical and Experimental Study of Control Schemes,” Faculty of Electrical Engineering, Technical University of Cluj-Napoca, 2012.

[2] V. Permiakov, “1D and 2D Magnetization in Electrical Steels under Uniaxial Stress,” PhD Dissertation, Department of Electrical Energy, systems and Automation, Ghent University, Belgium, 2005.

[3] F. Landgraf, “Nonoriented Electrical Steels,” *JOM*, vol. 64, no. 7, pp. 764–771, Jul. 2012.

[4] Y. Kurosaki, H. Mogi, H. Fujii, T. Kubota, and M. Shiozaki, “Importance of punching and workability in non-oriented electrical steel sheets,” *J. Magn. Magn. Mater.*, vol. 320, no. 20, pp. 2474–2480, Oct. 2008.

[5] M. Emura, F. J. G. Landgraf, W. Ross, and J. R. Barreta, “The influence of cutting technique on the magnetic properties of electrical steels,” *J. Magn. Magn. Mater.*, vol. 254–255, pp. 358–360, Jan. 2003.

[6] A. Belhadj, P. Baudouin, F. Breaban, A. Deffontaine, M. Dewulf, and Y. Houbaert, “Effect of laser cutting on microstructure and on magnetic properties of grain non-oriented electrical steels,” *J. Magn. Magn. Mater.*, vol. 256, no. 1–3, pp. 20–31, Jan. 2003.

[7] G.-Y. Zhou, H. Hao, M.-J. Jin, and J.-X. Shen, “Influence of interlocking dowels on motor core loss,” *Compel Bradf.*, vol. 35, no. 2, pp. 808–820, 2016.

[8] K. Senda, A. Fujita, A. Honda, N. Kuroki, and M. Yagi, “Magnetic properties and domain structure of nonoriented electrical steel under stress,” *Electr. Eng. Jpn.*, vol. 182, no. 4, pp. 10–18, Mar. 2013.

[9] H. Toda, Y. Oda, M. Kohno, M. Ishida, and Y. Zaizen, “A New High Flux Density Non-Oriented Electrical Steel Sheet and its Motor Performance,” *IEEE Trans. Magn.*, vol. 48, no. 11, pp. 3060–3063, Nov. 2012.

[10] H. Naumoski, B. Riedmüller, A. Minkow, and U. Herr, “Investigation of the influence of different cutting procedures on the global and local magnetic properties of non-oriented electrical steel,” *J. Magn. Magn. Mater.*, vol. 392, pp. 126–133, Oct. 2015.

[11] R. Siebert, J. Schneider, and E. Beyer, “Laser cutting and mechanical cutting of electrical steels and its effect on the magnetic properties,” *IEEE Trans. Magn.*, vol. 50, no. 4, 2014.

[12] G. Crevecoeur, L. Dupre, L. Vandenbossche, and R. V. de Walle, “Local Identification of Magnetic Hysteresis Properties Near Cutting Edges of Electrical Steel Sheets,” *IEEE Trans. Magn.*, vol. 44, no. 6, pp. 1010–1013, Jun. 2008.

[13] W. D. Callister, *Materials Science and Engineering: An Introduction*, 5th Edition. John Wiley and Sons, Inc.,USA, 1940.

[14] B. D. Cullity and C. D. Graham, *Introduction to Magnetic Materials, Second Edition*. 2008.

[15] G. Bertotti, "Chapter 1 - Magnetic Hysteresis," in *Hysteresis in Magnetism*, San Diego: Academic Press, 1998, pp. 3–30.

[16] N. Chukwuchekwa, "Investigation of Magnetic Properties and Barkhausen Noise of Electrical Steel," PhD thesis, Wolfson Centre of Magnetics, Cardiff University, Wales, United Kingdom, 2011.

[17] J. D. Kraus and K. R. Carver, *Electromagnetics*, Third edition. New york: McGraw-Hill Education, 1984.

[18] J. Barros, J. Schneider, K. Verbeken, and Y. Houbaert, "On the correlation between microstructure and magnetic losses in electrical steel," *J. Magn. Magn. Mater.*, vol. 320, no. 20, pp. 2490–2493, 2008.

[19] J. Shilling and G. Houze, "Magnetic properties and domain structure in grain-oriented 3% Si-Fe," *IEEE Trans. Magn.*, vol. 10, no. 2, pp. 195–223, Jun. 1974.

[20] F. D. Tan, J. L. Vollin, and S. M. Cuk, "A practical approach for magnetic core-loss characterization," *IEEE Trans. Power Electron.*, vol. 10, no. 2, pp. 124–130, Mar. 1995.

[21] G. Bertotti, "Chapter 12 - Eddy Currents," in *Hysteresis in Magnetism*, San Diego: Academic Press, 1998, pp. 391–430.

[22] V. Permiakov, L. Dupré, A. Pulnikov, and J. Melkebeek, "Loss separation and parameters for hysteresis modelling under compressive and tensile stresses," *J. Magn. Magn. Mater.*, vol. 272–276, no. SUPPL. 1, pp. e553–e554, 2004.

[23] M. LoBue, C. Sasso, V. Basso, F. Fiorillo, and G. Bertotti, "Power losses and magnetization process in Fe–Si non-oriented steels under tensile and compressive stress," *J. Magn. Magn. Mater.*, vol. 215–216, pp. 124–126, Jun. 2000.

[24] K. Matsumura and B. Fukuda, "Recent developments of non-oriented electrical steel sheets," *IEEE Trans. Magn.*, vol. 20, no. 5, pp. 1533–1538, Sep. 1984.

[25] D. S. Petrovič, "Non-oriented electrical steel sheets," *Mater. Tehnol.*, vol. 44, no. 6, pp. 317–325, 2010.

[26] P. Beckley, *Electrical Steels for Rotating Machines*. The Institution of Engineering and Technology, Michael Faraday House, Six Hills Way, Stevenage SG1 2AY, UK: IET, 2002.

[27] F. Fiorillo, *Characterization and Measurement of Magnetic Materials*. Academic Press, 2004.

[28] S. K. Ray and O. N. Mohanty, “Magnetic ageing characteristics of low silicon electrical steels,” *J. Magn. Magn. Mater.*, vol. 28, no. 1, pp. 44–50, Jul. 1982.

[29] K.-H. Kung, “A study of hot shortness in steels,” Masters Thesis, Missouri University of Science and Technology, 1965.

[30] P. Brissonneau, “Non-oriented electrical sheets,” *J. Magn. Magn. Mater.*, vol. 41, no. 1–3, pp. 38–46, Feb. 1984.

[31] A. Honda, Y. Obata, and S. Okamura, “History and recent development of non-oriented electrical steel in Kawasaki Steel,” *Kawasaki Steel Tech. Rep.*, no. 39, pp. 13–20, 1998.

[32] A. Honda, B. Fukuda, I. Ohyama, and Y. Mine, “Effects of magnetic properties of nonoriented electrical steel sheets on motor efficiency,” *J. Mater. Eng.*, vol. 12, no. 1, pp. 41–45, 1990.

[33] J. Füzer *et al.*, “Investigation of total losses of non-oriented electrical steels,” *Acta Phys. Pol. A*, vol. 118, no. 5, pp. 1018–1019, 2010.

[34] A. Honda, Y. Obata, and S. Okamura, “History and recent development of non-oriented electrical steel in Kawasaki Steel,” *Kawasaki Steel Tech. Rep.*, no. 39, pp. 13–20, 1998.

[35] M. Gallaugher, N. Brodusch, R. Gauvin, and R. R. Chromik, “Magnetic domain structure and crystallographic orientation of electrical steels revealed by a forescatter detector and electron backscatter diffraction,” *Ultramicroscopy*, vol. 142, pp. 40–49, Jul. 2014.

[36] J.-T. Park and J. A. Szpunar, “Evolution of recrystallization texture in nonoriented electrical steels,” *Acta Mater.*, vol. 51, no. 11, pp. 3037–3051, Jun. 2003.

[37] R. K. Ray, J. J. Jonas, and R. E. Hook, “Cold rolling and annealing textures in low carbon and extra low carbon steels,” *Int. Mater. Rev.*, vol. 39, no. 4, pp. 129–172, Jan. 1994.

[38] E. Cardelli *et al.*, “A challenging hysteresis operator for the simulation of Goss-textured magnetic materials,” *J. Magn. Magn. Mater.*, vol. 432, pp. 14–23, Jun. 2017.

[39] L. Kestens and S. Jacobs, “Texture control during the manufacturing of nonoriented electrical steels,” *Texture Stress Microstruct.*, vol. 2008, 2008.

[40] M. A. da Cunha and S. da C. Paolinelli, “Low core loss non-oriented silicon steels,” *J. Magn. Magn. Mater.*, vol. 320, no. 20, pp. 2485–2489, Oct. 2008.

[41] K. Verbeken, I. Infante-Danzo, J. Barros-Lorenzo, J. Schneider, and Y. Houbaert, “Innovative processing for improved electrical steel properties,” *Rev. Metal. Madr.*, vol. 46, no. 5, pp. 458–468, 2010.

[42] F. Bohn, A. Gündel, F. J. G. Landgraf, A. M. Severino, and R. L. Sommer, “Magnetostriction, Barkhausen noise and magnetization processes in E110 grade non-oriented electrical steels,” *J. Magn. Magn. Mater.*, vol. 317, no. 1–2, pp. 20–28, 2007.

[43] A. Chaudhury *et al.*, “Low silicon non-grain-oriented electrical steel: Linking magnetic properties with metallurgical factors,” *J. Magn. Magn. Mater.*, vol. 313, no. 1, pp. 21–28, Jun. 2007.

[44] M. A. Laughton and D. F. Warne, *Electrical Engineer’s Reference Book*, 16th Edition. Newnes, 2002.

[45] A. Schoppa, J. Schneider, and J.-O. Roth, “Influence of the cutting process on the magnetic properties of non-oriented electrical steels,” *J. Magn. Magn. Mater.*, vol. 215–216, pp. 100–102, Jun. 2000.

[46] A. Schoppa, H. Louis, F. Pude, and C. von Rad, “Influence of abrasive waterjet cutting on the magnetic properties of non-oriented electrical steels,” *J. Magn. Magn. Mater.*, vol. 254–255, pp. 370–372, Jan. 2003.

[47] P. Baudouin, M. De Wulf, L. Kestens, and Y. Houbaert, “The effect of the guillotine clearance on the magnetic properties of electrical steels,” *J. Magn. Magn. Mater.*, vol. 256, no. 1–3, pp. 32–40, Jan. 2003.

[48] H. M. S. Harstick, M. Ritter, A. Plath, and W. Riehemann, “EBSD Investigations on Cutting Edges of Non-Oriented Electrical Steel,” *Metallogr. Microstruct. Anal.*, vol. 3, no. 4, pp. 244–251, Jul. 2014.

[49] W. Shi, J. Liu, and C. Li, “Effect of cutting techniques on the structure and magnetic properties of a high-grade non-oriented electrical steel,” *J. Wuhan Univ. Technol.-Mater Sci Ed*, vol. 29, no. 6, pp. 1246–1251, Dec. 2014.

[50] X. Xiong, S. Hu, K. Hu, and S. Zeng, “Texture and magnetic property evolution of non-oriented Fe–Si steel due to mechanical cutting,” *J. Magn. Magn. Mater.*, vol. 401, pp. 982–990, Mar. 2016.

[51] R. Chandramouli, “Sheet metal operations - Cutting and related processes.” NPTEL - Mechanical Engineering - Forming, Joint Initiative of IITs and IISc - Funded by MHRD.

[52] A. Pulnikov, P. Baudouin, and J. Melkebeek, “Induced stresses due to the mechanical cutting of non-oriented electrical steels,” *J. Magn. Magn. Mater.*, vol. 254–255, pp. 355–357, Jan. 2003.

[53] M. Hofmann, H. Naumoski, U. Herr, and H.-G. Herzog, “Magnetic Properties of Electrical Steel Sheets in Respect of Cutting: Micromagnetic Analysis and Macromagnetic Modeling,” *IEEE Trans. Magn.*, vol. 52, no. 2, 2016.

[54] F. Ossart, E. Hug, O. Hubert, C. Buvat, and R. Billardon, “Effect of punching on electrical steels: Experimental and numerical coupled analysis,” *IEEE Trans. Magn.*, vol. 36, no. 5 I, pp. 3137–3140, 2000.

[55] G. Loisos and A. J. Moses, “Effect of mechanical and Nd:YAG laser cutting on magnetic flux distribution near the cut edge of non-oriented steels,” *J. Mater. Process. Technol.*, vol. 161, no. 1–2, pp. 151–155, Apr. 2005.

[56] T. Omura, Y. Zaizen, M. Fukumura, K. Senda, and H. Toda, “Effect of Hardness and Thickness of Nonoriented Electrical Steel Sheets on Iron Loss Deterioration by Shearing Process,” *IEEE Trans. Magn.*, vol. 51, no. 11, 2015.

[57] H. A. Weiss *et al.*, “Influence of shear cutting parameters on the electromagnetic properties of non-oriented electrical steel sheets,” *J. Magn. Magn. Mater.*, vol. 421, pp. 250–259, Jan. 2017.

[58] V. Manescu, G. Paltanea, H. Gavrila, and I. Peter, “The influence of punching and laser cutting technologies on the magnetic properties of non-oriented silicon iron steels,” in *2014 International Symposium on Fundamentals of Electrical Engineering (ISFEE)*, 2014, pp. 1–4.

[59] C. C. Chiang, M. F. Hsieh, Y. H. Li, and M. C. Tsai, “Impact of Electrical Steel Punching Process on the Performance of Switched Reluctance Motors,” *IEEE Trans. Magn.*, vol. 51, no. 11, pp. 1–4, Nov. 2015.

[60] Y. Kashiwara, H. Fujimura, K. Okamura, K. Imanishi, and H. Yashiki, “Estimation model for magnetic properties of stamped electrical steel sheet,” *Electr. Eng. Jpn.*, vol. 183, no. 2, pp. 1–11, Apr. 2013.

[61] L. Dupré, R. Van Keer, and J. Melkebeek, “A study of the influence of laser cutting and punching on the electromagnetic behaviour of electrical steel sheets using a combined finite element - dynamic Preisach model,” *Proc. 4th Intern Workshop Electr. Magn. Fields Assoc Ingé N Montefiore Marseille 1998*, pp. 195–200, 1998.

[62] R. Siebert, R. Baumann, E. Beyer, P. Herwig, and A. Wetzig, “Laser manufacturing of electrical machines,” in *Electric Drives Production Conference (EDPC), 2014 4th International*, 2014, pp. 1–5.

[63] A. Belhadj, P. Baudouin, and Y. Houbaert, “Simulation of the HAZ and magnetic properties of laser cut non-oriented electrical steels,” *J. Magn. Magn. Mater.*, vol. 248, no. 1, pp. 34–44, Jul. 2002.

[64] S. K. Chang, “Texture effects on magnetic properties in high-alloyed non-oriented electrical steels,” *Met. Sci. Heat Treat.*, vol. 49, no. 11–12, pp. 569–573, Nov. 2007.

[65] Y. Kai, Y. Tsuchida, T. Todaka, and M. Enokizono, “Effect of local residual stress in rotating machine core on vector magnetic property,” in *2010 XIX International Conference on Electrical Machines (ICEM)*, 2010, pp. 1–6.

[66] Y. Ding, M. Gallaugher, N. Brodusch, R. Gauvin, and R. R. Chromik, “Effect of a Coating Induced Residual Stress on Magnetic Domain Structure in Non-Oriented Electrical Steels,” *Microsc. Microanal.*, vol. 20, no. S3, pp. 894–895, Aug. 2014.

[67] P. Vourna, A. Ktena, and E. Hristoforou, “Residual stress analysis in nonoriented electrical steel sheets by barkhausen noise measurements,” *IEEE Trans. Magn.*, vol. 50, no. 4, 2014.

[68] K. Fujisaki *et al.*, “Motor core iron loss analysis evaluating shrink fitting and stamping by finite-element method,” *IEEE Trans. Magn.*, vol. 43, no. 5, pp. 1950–1954, 2007.

[69] “IEC 60404-2:1996, Magnetic materials - Part 2: Methods of measurement of the magnetic properties of electrical steel sheet and strip by means of an Epstein frame,” 1996.

[70] A. Pulnikov, “Modification of magnetic properties of non oriented electrical steels by the production of electromagnetic devices,” 2004. .

[71] J. Gyselinck, “Twee-Dimesionale Dynamische Eindige- Elementenmodellering van Statische en Roterende Elektromagnetische Energieomzetters,” PhD Dissertation, School of Electrical Engineering, Electrical Machines and Power Electronics, Ghent Univesrity, Belgium, 2000.

[72] D. L. Rodrigues-Jr *et al.*, “Effect of Plastic Deformation on the Excess Loss of Electrical Steel,” *IEEE Trans. Magn.*, vol. 48, no. 4, pp. 1425–1428, Apr. 2012.

[73] F. J. G. Landgraf and M. Emura, “Losses and permeability improvement by stress relieving fully processed electrical steels with previous small deformations,” *J. Magn. Magn. Mater.*, vol. 242–245, Part 1, pp. 152–156, Apr. 2002.

[74] E. De *et al.*, “Comparison of iron losses evaluations by different testing procedures,” presented at the 19th International Conference on Electrical Machines, ICEM 2010, 2010.

[75] “IEC 60404-3:1992, Magnetic materials – Part 3: Methods of measurement of the magnetic properties of electrical steel sheet and strip by means of a single sheet tester,” 1992.

[76] L. Rahf, J. D. Sievert, and Q.-C. Qu, “Single strip tester for the determination of magnetic losses and hysteresis parameters,” *J. Magn. Magn. Mater.*, vol. 24, no. 2, pp. 218–220, Sep. 1981.

[77] H. Ahlers, J. D. Sievert, and Q. -ch. QU, “Comparison of a single strip tester and Epstein frame measurements,” *J. Magn. Magn. Mater.*, vol. 26, no. 1, pp. 176–178, Mar. 1982.

[78] M. De Wulf, D. Makaveev, Y. Houbaert, and J. Melkebeek, “Design and calibration aspects of small size single sheet testers,” *J. Magn. Magn. Mater.*, vol. 254–255, pp. 70–72, Jan. 2003.

[79] A. J. Moses and D. Davies, “Influence of Compressive Stress on Magnetic Properties of Commercial (110) [001] Oriented Silicon-Iron,” *IEEE Trans. Magn.*, vol. 16, no. 2, pp. 454–460, 1980.

[80] A. Moses, “Effects of applied stress on the magnetic properties of high permeability silicon-iron,” *IEEE Trans. Magn.*, vol. 15, no. 6, pp. 1575–1579, Nov. 1979.

[81] A. Moses, “Effects of stress on the magnetic properties of grain-oriented silicon-iron magnetized in various directions,” *IEEE Trans. Magn.*, vol. 17, no. 6, pp. 2872–2874, Nov. 1981.

[82] V. E. Iordache, F. Ossart, and E. Hug, “Magnetic characterisation of elastically and plastically tensile strained non-oriented Fe-3.2%Si steel,” *J. Magn. Magn. Mater.*, vol. 254–255, pp. 57–59, 2003.

[83] V. E. Iordache, E. Hug, and N. Buiron, “Magnetic behaviour versus tensile deformation mechanisms in a non-oriented Fe–(3 wt.%)Si steel,” *Mater. Sci. Eng. A*, vol. 359, no. 1–2, pp. 62–74, Oct. 2003.

[84] V. E. Iordache and E. Hug, “Effect of mechanical strains on the magnetic properties of electrical steels,” *J. Optoelectron. Adv. Mater.*, vol. 6, no. 4, pp. 1297–1303, 2004.

[85] A. Pulnikov, V. Permiakov, W. De, and J. Melkebeek, “Measuring setup for the investigation of the influence of mechanical stresses on magnetic properties of electrical steel,” *J. Magn. Magn. Mater.*, vol. 254–255, pp. 47–49, 2003.

[86] D. Miyagi, Y. Aoki, M. Nakano, and N. Takahashi, “Effect of Compressive Stress in Thickness Direction on Iron Losses of Nonoriented Electrical Steel Sheet,” *IEEE Trans. Magn.*, vol. 46, no. 6, pp. 2040–2043, Jun. 2010.

[87] N. Takahashi and D. Miyagi, “Effect of stress on iron loss of motor core,” in *Electric Machines Drives Conference (IEMDC), 2011 IEEE International*, 2011, pp. 469–474.

[88] N. Takahashi, M. Morishita, D. Miyagi, and M. Nakano, “Examination of Magnetic Properties of Magnetic Materials at High Temperature Using a Ring Specimen,” *IEEE Trans. Magn.*, vol. 46, no. 2, pp. 548–551, 2010.

[89] T. Kanada, Y. Kido, A. Kutsukake, T. Ikeda, and M. Enokizono, “Magnetic properties of soft magnetic materials under tensile and compressive stress,” *Przeglad Elektrotechniczny*, vol. 87, no. 9 B, pp. 93–96, 2011.

[90] T. Nakata, N. Takahashi, K. Fujiwara, and M. Nakano, “Measurement of magnetic characteristics along arbitrary directions of grain-oriented silicon steel up to high flux densities,” *IEEE Trans. Magn.*, vol. 29, no. 6, pp. 3544–3546, 1993.

[91] N. Nencib, A. Kedous-Lebouc, and B. Cornut, “Performance evaluation of a large rotational single sheet tester,” *J. Magn. Magn. Mater.*, vol. 160, pp. 174–176, Jul. 1996.

[92] M. Nakano, H. Nishimoto, K. Fujiwara, and N. Takahashi, “Improvements of single sheet testers for measurement of 2-d magnetic properties up to high flux density,” *IEEE Trans. Magn.*, vol. 35, no. 5 PART 2, pp. 3965–3967, 1999.

[93] D. Makaveev, R. Von, W. De, and J. Melkebeek, “Accurate field strength measurement in rotational single sheet testers,” *J. Magn. Magn. Mater.*, vol. 215, pp. 673–676, 2000.

[94] Y. Kai, Y. Tsuchida, T. Todaka, and M. Enokizono, “Influence of Stress on Vector Magnetic Property Under Alternating Magnetic Flux Conditions,” *IEEE Trans. Magn.*, vol. 47, no. 10, pp. 4344–4347, Oct. 2011.

[95] Y. Kai, Y. Tsuchida, T. Todaka, and M. Enokizono, “Influence of Stress on Vector Magnetic Property Under Rotating Magnetic Flux Conditions,” *IEEE Trans. Magn.*, vol. 48, no. 4, pp. 1421–1424, Apr. 2012.

[96] Y. Kai and M. Enokizono, “Measurement of two-dimensional magnetostriction of a non-oriented electrical steel sheet under shear stress,” *Int. J. Appl. Electromagn. Mech.*, vol. 48, no. 2–3, pp. 233–238, 2015.

[97] Y. Kai, Y. Tsuchida, T. Todaka, and M. Enokizono, “Measurement Method of Vector Magnetic Properties of a Non-oriented Electrical Steel Sheet under Stress Conditions,” *IEEJ Trans. Fundam. Mater.*, vol. 132, no. 10, pp. 930–935, 2012.

[98] Y. Kai, M. Enokizono, and Y. Kido, “Measurement of vector magnetic properties of a nonoriented electrical steel sheet under shear stress,” *Electr. Eng. Jpn. Engl. Transl. Denki Gakkai Ronbunshi*, vol. 191, no. 4, pp. 1–7, 2015.

[99] A. J. Schwartz, M. Kumar, B. L. Adams, and D. P. Field, Eds., *Electron Backscatter Diffraction in Materials Science*. Boston, MA: Springer US, 2009.

[100] D. E. Newbury, D. C. Joy, P. Echlin, C. E. Fiori, and J. I. Goldstein, *Advanced Scanning Electron Microscopy and X-Ray Microanalysis*. Boston, MA: Springer US, 1986.

[101] D. C. Joy, D. E. Newbury, and D. L. Davidson, “Electron channeling patterns in the scanning electron microscope,” *J. Appl. Phys.*, vol. 53, no. 8, pp. R81–R122, Aug. 1982.

[102] J. Goldstein, *Scanning Electron Microscopy and X-ray Microanalysis: Third Edition*. Plenum, 2003.

[103] H. C. Rogers, “Adiabatic Plastic Deformation,” *Annu. Rev. Mater. Sci.*, vol. 9, no. 1, pp. 283–311, 1979.

[104] S. da C. Paolinelli, M. A. da Cunha, and A. B. Cota, “The influence of shear bands on final structure and magnetic properties of 3% Si non-oriented silicon steel,” *J. Magn. Magn. Mater.*, vol. 320, no. 20, pp. e641–e644, Oct. 2008.

[105] S. Chikazumi, *Physics of Ferromagnetism*, Second Edition. Oxford University Press, 1996.

[106] “ASTM-E112 Standard Test Methods for Determining Average Grain Size.” 2013.

[107] W. C. Oliver and G. M. Pharr, “An improved technique for determining hardness and elastic modulus using load and displacement sensing indentation experiments,” *J. Mater. Res.*, vol. 7, no. 6, pp. 1564–1583, Jun. 1992.

[108] S. Suresh and A. E. Giannakopoulos, “A new method for estimating residual stresses by instrumented sharp indentation,” *Acta Mater.*, vol. 46, no. 16, pp. 5755–5767, Oct. 1998.

[109] A. C. Fischer-Cripps, *Nanoindentation*. New York, NY: Springer New York, 2004.

[110] “Hysitron Triboindenter User Manual.” Hysitron, Inc. Minneapolis USA.

[111] A. Montagne, V. Audurier, and C. Tromas, “Influence of pre-existing dislocations on the pop-in phenomenon during nanoindentation in MgO,” *Acta Mater.*, vol. 61, no. 13, pp. 4778–4786, Aug. 2013.

[112] “Measuring Technology for defining parameters of soft magnetic materials.” Brockhaus Measurements, Germany.

[113] T. Nakayama and H. Kojima, “Interlocking Performances on Non-Oriented Electrical Steels,” *J. Mater. Eng. Perform.*, vol. 16, no. 1, pp. 7–11, Feb. 2007.

[114] K. Senda, H. Toda, and M. Kawano, “Influence of Interlocking on Core Magnetic Properties,” *IEEJ J. Ind. Appl.*, vol. 4, no. 4, pp. 496–502, 2015.

[115] M. P. Groover, *Fundamentals of Modern Manufacturing: Materials, Processes, and Systems*, 5th Edition. 2012.

[116] E. Frutos, M. Multigner, and J. L. González-Carrasco, “Novel approaches to determining residual stresses by ultramicroindentation techniques: Application to sandblasted austenitic stainless steel,” *Acta Mater.*, vol. 58, no. 12, pp. 4191–4198, Jul. 2010.

[117] M. Göken and M. Kempf, “Pop-ins in Nanoindentations - the Initial Yield Point,” *Z. Fuer Met.*, vol. 92, no. 9, pp. 1061–1067, 2001.

[118] M. Lindenmo, A. Coombs, and D. Snell, “Advantages, properties and types of coatings on non-oriented electrical steels,” *J. Magn. Magn. Mater.*, vol. 215–216, pp. 79–82, Jun. 2000.

[119] J. R. Bowen, P. B. Prangnell, and F. J. Humphreys, “Microstructural evolution during formation of ultrafine grain structures by severe deformation,” *Mater. Sci. Technol.*, vol. 16, no. 11–12, pp. 1246–1250, Nov. 2000.

[120] C. Kaido, H. Mogi, M. Fujikura, and J. Yamasaki, “Punching Deterioration Mechanism of Magnetic Properties of Cores,” *IEEJ Trans. Fundam. Mater.*, vol. 128, no. 8, pp. 545–550, 2008.

[121] Y. Ding, M. Gallaugher, N. Brodusch, R. Gauvin, and R. R. Chromik, “Coating induced residual stress in nonoriented electrical steel laminations,” *J. Mater. Res.*, vol. 29, no. 16, pp. 1737–1746, 2014.

[122] A. Barnoush, “Correlation between dislocation density and nanomechanical response during nanoindentation,” *Acta Mater.*, vol. 60, no. 3, pp. 1268–1277, Feb. 2012.

[123] D. Dorner, S. Zaefferer, and D. Raabe, "Retention of the Goss orientation between microbands during cold rolling of an Fe3%Si single crystal," *Acta Mater.*, vol. 55, no. 7, pp. 2519–2530, Apr. 2007.

[124] B. Hutchinson, "Deformation microstructures and textures in steels," *Philos. Trans. R. Soc. Lond. Math. Phys. Eng. Sci.*, vol. 357, no. 1756, pp. 1471–1485, Jun. 1999.

[125] T. Ohmura, K. Tsuzaki, and F. Yin, "Nanoindentation-Induced Deformation Behavior in the Vicinity of Single Grain Boundary of Interstitial-Free Steel," *Mater. Trans.*, vol. 46, no. 9, pp. 2026–2029, 2005.

[126] D. F. Bahr, D. E. Kramer, and W. W. Gerberich, "Non-linear deformation mechanisms during nanoindentation," *Acta Mater.*, vol. 46, no. 10, pp. 3605–3617, Jun. 1998.

[127] T. Sakai, A. Belyakov, and H. Miura, "Ultrafine Grain Formation in Ferritic Stainless Steel during Severe Plastic Deformation," *Metall. Mater. Trans. A*, vol. 39, no. 9, p. 2206, May 2008.

[128] L. Zhang, T. Ohmura, and K. Tsuzaki, "Application of Nanoindentation Technique in Martensitic Structures," in *Nanoindentation in Materials Science*, J. Nemecek, Ed. InTech, 2012.

[129] T. H. Ahn, C. Shin, N. H. Han, and J. Kwon, "Evaluation of bulk properties of structural materials from small-scale mechanical tests," *ASEM13*, Sep. 2013.

[130] W. D. Nix and H. Gao, "Indentation size effects in crystalline materials: A law for strain gradient plasticity," *J. Mech. Phys. Solids*, vol. 46, no. 3, pp. 411–425, Mar. 1998.

[131] R. Rodríguez and I. Gutierrez, "Correlation between nanoindentation and tensile properties influence of the indentation size effect," *Mater. Sci. Eng. A*, vol. 361, no. 1–2, pp. 377–384, 2003.

[132] D. Tabor, *The Hardness of Metals*. New York: Oxford University Press, 2000.

[133] E. Schafler, M. Zehetbauer, A. Borbely, and T. Ungar, "Dislocation densities and internal stresses in large strain cold worked pure iron," *Mater. Sci. Eng. A*, vol. 234, pp. 445–448, Aug. 1997.

[134] A. Peksoz, S. Erdem, and N. Derebasi, "Mathematical model for cutting effect on magnetic flux distribution near the cut edge of non-oriented electrical steels," *Comput. Mater. Sci.*, vol. 43, no. 4, pp. 1066–1068, Oct. 2008.

[135] K. H. Schmidt, "Der einfluss des stanzens auf die magnetischen eigenschaften von elektroblech mit 1% silizium," *J. Magn. Magn. Mater.*, vol. 2, no. 1, pp. 136–150, Dec. 1975.

[136] M. Popescu, T. J. E. Miller, M. McGilp, D. M. Ionel, S. J. Dellinger, and R. J. Heidemann, "On the physical basis of power losses in laminated steel and minimum-effort

modeling in an industrial design environment," presented at the Conference Record - IAS Annual Meeting (IEEE Industry Applications Society), 2007, pp. 60–66.

[137] W. M. Arshad *et al.*, "Incorporating Lamination Processing and Component Manufacturing in Electrical Machine Design Tools," in *Conference Record of the 2007 IEEE Industry Applications Conference, 2007. 42nd IAS Annual Meeting*, 2007, pp. 94–102.

[138] P. Baudouin, A. Belhadj, F. Breaban, A. Deffontaine, and Y. Houbaert, "Effects of laser and mechanical cutting modes on the magnetic properties of low and medium Si content nonoriented electrical steels," *IEEE Trans. Magn.*, vol. 38, no. 5, pp. 3213–3215, Sep. 2002.